MICROFLUIDIC PLATFORMS FOR THE INVESTIGATION OF FUEL CELL CATALYSTS AND ELECTRODES

BY

FIKILE R. BRUSHETT

DISSERTATION

Submitted in partial fulfillment of the requirements
for the degree of Doctor of Philosophy in Chemical Engineering
in the Graduate College of the
University of Illinois at Urbana-Champaign, 2010

Urbana, Illinois

Doctoral Committee:

Professor Paul J.A. Kenis, Chair
Professor Rich I. Masel
Professor Andrzej Wieckowski
Professor Edmund G. Seebauer

Abstract

A clear need exists for novel approaches to producing and utilizing energy in more efficient ways, in light of society's ever increasing demand as well as growing concerns with respect to climate change related to CO_2 emissions. The development of low temperature fuel cell technologies will continue to play an important role in many alternative energy conversion strategies, especially for portable electronics and automotive applications. However, widespread commercialization of fuel cell technologies has yet to be achieved due to a combination of high costs, poor durability and, system performance limitations **(Chapter 1)**. Developing a better understanding of the complex interplay of electrochemical, transport, and degradation processes that govern the performance and durability of novel fuel cell components, particularly catalysts and electrodes, *within operating fuel cells* is critical to designing robust, inexpensive configurations that are required for commercial introduction. Such detailed *in-situ* investigations of individual electrode processes are complicated by other factors such as water management, uneven performance across electrodes, and temperature gradients. Indeed, too many processes are interdependent on the same few variable parameters, necessitating the development of novel analytical platforms with more degrees of freedom.

Previously, membraneless microfluidic fuel cells have been developed to address some of the aforementioned fuel cell challenges **(Chapter 2)**. At the microscale, the laminar nature of fluid flow eliminates the need for a physical barrier, such as a stationary membrane, while still allowing ionic transport between electrodes. This enables the development of many unique and innovative fuel cell designs. In addition to addressing water management and fuel crossover issues, these laminar flow-based systems allow for the independent specification of individual stream compositions (*e.g.*, pH). Furthermore, the use of a liquid electrolyte enables the simple *in-situ* analysis of individual electrode performance using an off-the-shelf reference electrode. *These advantages can be leveraged to develop microfluidic fuel cells as versatile electro-analytical platforms for the characterization and optimization*

of catalysts and electrodes for both membrane- and membraneless fuel cells applications. To this end, a microfluidic hydrogen-oxygen (H_2/O_2) fuel cell has been developed which utilizes a flowing liquid electrolyte instead of a stationary polymeric membrane. For analytical investigations, the flowing stream (*i*) enables autonomous control over electrolyte parameters (*i.e.,* pH, composition) and consequently the local electrode environments, as well as (*ii*) allows for the independent *in-situ* analyses of catalyst and/or electrode performance and degradation characteristics via an external reference electrode (*e.g.,* Ag/AgCl). Thus, this microfluidic analytical platform enables a high number of experimental degrees of freedom, previously limited to a three-electrode electrochemical cell, to be employed in the construct of working fuel cell.

Using this microfluidic H_2/O_2 fuel cell as a versatile analytical platform, the focus of this work is to provide critical insight into the following research areas:

- Identify the key processes that govern the electrode performance and durability in alkaline fuel cells as a function of preparation methods and operating parameters **(Chapter 3)**.
- Determine the suitability of a novel Pt-free oxygen reduction reaction catalyst embedded in gas diffusion electrodes for acidic and alkaline fuel cell applications **(Chapter 4)**.
- Establish electrode structure-activity relationships by aligning *in-situ* electrochemical analyses with *ex-situ* microtomographic (MicroCT) structural analyses **(Chapter 5)**.
- Investigate the feasibility and utility of a microfluidic-based vapor feed direct methanol fuel cell (VF-DMFC) configuration as a power source for portable applications **(Chapter 6)**.

In all these areas, the information garnered from these *in-situ* analytical platforms will advance the development of more robust and cost-effective electrode configurations and thus more durable and commercially-viable fuel cell systems (*both membrane-based and membraneless*).

Acknowledgements

I would like to express my gratitude to several people without whom this work would not have been possible. First and foremost, I am profoundly grateful to my advisor, Professor Paul J.A. Kenis, for his patience, guidance, and support. I am also deeply indebted to Dr. Jayashree Ranga, Dr. Wei-Ping Zhou, and Dr. Michael Mitchell for their invaluable mentorship in fuel cell and electrochemical analyses. Also, I am thankful to my thesis committee, Professors Rich Masel, Andrzej Wieckowski, and Edmund Seebauer, for their support during the faculty and postdoctoral job searches.

In addition to my mentors, I would like to thank my co-workers in the Kenis group. Many thanks go to Matt Naughton and Molly Jhong with whom I worked most closely. Indeed, much of this work would not be possible without their excellent contributions. In addition, thanks go to the talented undergraduate students, namely Desmond Ng, Alix Schmidt, Raymond Grieshaber, and Nicolas Lioutas, whom I have had the pleasure of mentoring. I am also grateful to my colleagues in the electrochemistry section of the Kenis group, namely Adam Hollinger, Pedro Lopez-Montesinos, Michael Thorson, and Devin Whipple, for their scientific insight. Finally, I am grateful to the other Kenis group members, particularly Joshua Tice, Benjamin Schudel, Jerrod Henderson, Sudipto Guha and Sarah Perry, for their scientific insight, editorial assistance, and much needed camaraderie during the completion of this work.

Beyond the Kenis group, I would like to thank my collaborators. I am grateful to Professor Andrew Gewirth and members of his research group, namely Matt Thorum and Claire Tornow, in the Chemistry Department for their help in synthesizing and characterizing the novel catalyst described in Chapter 4. I am also grateful to Leilei Yin, Darren Stevenson, Scott Robinson, and Cate Wallace in the Imaging Technology Group at the Beckman Institute for their assistance in materials imaging and analysis.

Finally, I am appreciative of the generous financial support provided by the Graduate Engineering for Minorities (GEM), the Support for Under-Represented Groups in Engineering (SURGE), and the Harry G. Drickamer fellowship programs.

To my immediate and extended family who taught me there is no substitute for hard work

Table of Contents

Chapter 1

Introduction*

1.1 Addressing Global Energy Challenges

Global industrial development is approaching the point where new strategies must be implemented to manage energy supply and demand. Rising population and industrial growth in the developing world, particularly in China and India, have led to increasing global energy consumption (Figure 1.1) [1]. Simultaneously, a concerted effort is needed to confront the fast-disappearing reserves of conventional fossil fuels (*i.e.*, crude oil). These fuels are often mined in regions of the world that may be considered unfriendly to North America, Europe and Australia, which are still the main energy consumers. Furthermore, the inefficiency and significant greenhouse gas emissions make the direct combustion of more locally abundant fossil fuels, *i.e.* coal and natural gas, increasingly undesirable [1]. Therefore, a need exists for: (*i*) discovery and large-scale production of alternative fuels; and (*ii*) high efficiency utilization of these fuels via novel energy conversion systems such as fuel cells.

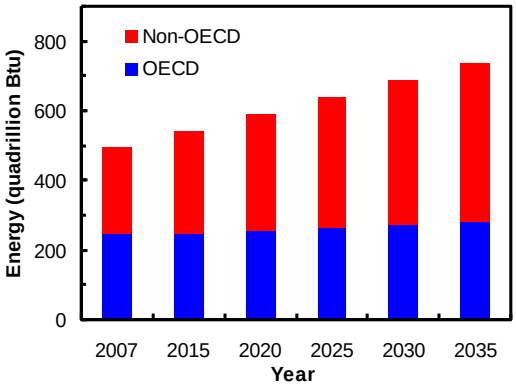

Figure 1.1. Projected world market energy consumption, 2007 - 2035. OECD is the Organization of Economic Cooperation and Development. Both China and India are Non-OECD countries. Data was obtained at the following source [1].

Fuel cells enable efficient conversion of chemical energy to electrical energy without the *Carnot* cycle limitations. Moreover, alternative fuels such as hydrogen, formic acid, bio-alcohols (generated from green processes using renewable energy sources, such as biomass, wind,

* Part of this work has been published: F.R. Brushett, P.J.A Kenis, A. Wieckowski, "New Concepts in the Chemistry and Engineering of Low Temperature Fuel Cells", *Fuel Cell Science: Theory, Fundamentals, and Biocatalysis*, A. Wieckowski & J.K. Norskov, editors, (John Wiley & Sons, Inc.), pg. 565-610.

and solar) can be utilized by fuel cells. Thus, the continued development of fuel cell technologies is of vital importance to strategies aimed at addressing the world's current energy challenges. While a number of fuel cell technologies exist, this thesis focuses on low-temperature fuel cells ($T \leq 120$ °C). Compared to higher temperature systems (T = 200 - 800 °C), these cells have shorter start-up and transient-response times, higher power densities (or specific power), and lower costs [2]. Thus, low-temperature fuel cells have been the subject of intensive industrial and academic research efforts for a range of energy conversion applications (*i.e.*, portable electronics, automotive transport) [2-6]. The proceeding sections will briefly review the current status in the development of low temperature acidic and alkaline fuel cells.

1.2 Overview of Current Acidic Fuel Cell Technology

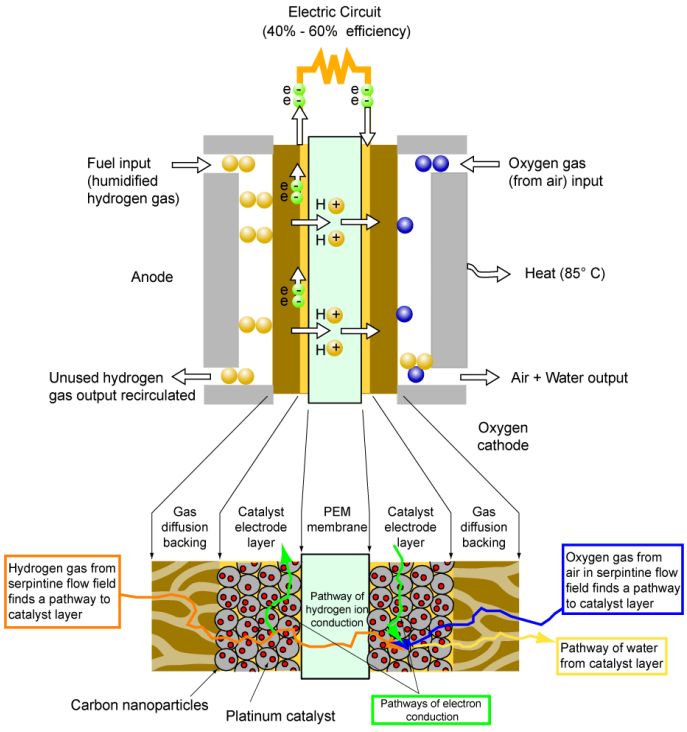

Figure 1.2. Schematic of a zero-emission hydrogen-fueled polymer electrolyte membrane fuel cell (PEMFC). Hydrogen electro-oxidizes on the anode, splitting into protons and electrons. These electrons travel around an external circuit powering a load whereas the protons travel through a conductive membrane (*e.g.*, Nafion) which separates the electrodes. On the cathode, oxygen (from air) combines with the protons and electrons and electro-reduces to produce water. The generated water is then removed from the fuel cell by the now oxygen-depleted air stream. Image courtesy of the Neutron Imaging Facility of the National Institute of Standards and Technology (NIST).

In acidic fuel cells, a fuel is electro-oxidized on the anode to produce protons, electrons, and reaction by-products. These electrons travel around an external circuit powering a load whereas the protons travel through a conductive electrolyte which spatially separates the two electrodes. On the cathode, oxygen combines with the protons and electrons and electro-reduces to produce water. Any by-products generated at either electrode are removed from the fuel cell by the depleted reactant streams. At present, acidic polymer electrolyte membrane (PEM)-based fuel cells are generally considered the "configuration-of-choice" for most low-temperature applications (Figure 1.2) [2-6]. When hydrated, the acidity of these sub-millimeter solid PEMs enables the dissociation of protons from the polymeric backbone. Thus, these membranes spatially separate the two electrode reactions, selectively conduct protons, and block the passage of unreacted fuels and reaction by-products. Nafion, a persulfonated polytetrafluoroethylene ionomer (synthetic polymer with ionic properties) developed by DuPont, is the most widely used PEM material although other polyaromatic-sulfonate ionomers are also employed [7].

PEM-based fuel cells can be broadly divided into two categories: hydrogen-fueled PEM-based fuel cells (PEMFCs) and direct liquid fuel cells (DLFCs) using small alcohols (*i.e.*, methanol, ethanol), formic acid or simple ethers as fuels [2-6,8-10]. PEMFCs are considered eco-friendly, zero-emission power sources, as the only generated by-product is water (Figure 1.2). However, hydrogen fuel must be generated, ideally from water or biomass using the aforementioned renewable solar, nuclear or wind energies. Among the most-developed fuel cell technologies, PEMFCs have been successfully demonstrated in stationary, extraterrestrial, and, most recently, automotive applications [2,5]. For portable applications, safety concerns and practical issues associated with the on-board storage of hydrogen at high volumetric energy density have spurred the development of DLFCs, which benefit from the high energy density and

easier storage of organic fuels (Figure 1.3) [11]. Unlike PEMFCs, DLFCs produce the greenhouse gas carbon dioxide (CO_2), via the electro-oxidation of organic fuels, but the emission rate per energy unit is significantly lower than the CO_2 production rate of conventional energy conversion systems (*i.e.*, internal combustion engines) because of the greater efficiencies of fuel cell-based systems. Both direct methanol fuel cells (DMFCs) and direct formic acid fuel cells (DFAFCs) have experienced moderate commercial success in niche applications, namely, military and telecommunications [12].

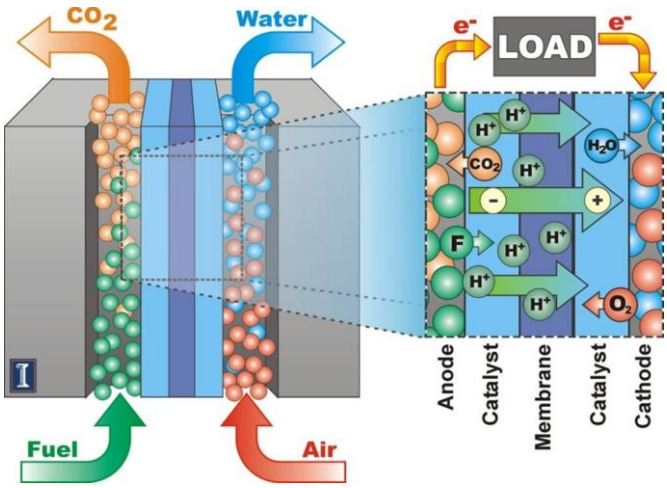

Figure 1.3. Schematic of an acidic direct liquid fuel cell (DLFC) utilizing a small organic fuel (*e.g.*, methanol, ethanol, formic acid). This image is reprinted with the permission of Joshua Ackerman.

Despite some success, widespread market penetration of acidic fuel cell technologies has yet to be realized due to (*i*) high costs, (*ii*) insufficient durability, and (*iii*) system performance limitations. *First*, the limited availability and high cost of platinum (Pt) is a significant concern, as it is typically the main component of both anode and cathode fuel cell catalysts. The natural abundance of Pt is low. The metal is only mass-produced in two world regions, South Africa and Russia. Smaller deposits also exist in North America and Zimbabwe. Furthermore, with future large-scale production of fuel cells, Pt prices would likely increase causing significant perturbations in the market. Thus, minimizing or eliminating the Pt content of fuel cell catalysts while maintaining acceptable power output and electrode durability remains a major challenge. In addition, despite continued advances in the synthesis and theory of conducting polymers, PEM materials remain prohibitively expensive.

Second, the insufficient long-term stability of the present PEM-based fuel cell technologies, coupled with the already-mentioned high costs has, thus far, prevented widespread commercialization. For example, according to the US Department of Energy (DOE) guidelines, fuel cell systems for automotive applications must provide power for 5,000 hours and 150,000 miles to be comparable with modern internal combustion engines [2,5]. Presently, most PEM-based fuel cell systems operate efficiently for only a fraction of that required lifetime before suffering a decrease in power output. An improved understanding of the fundamental degradative processes that govern component durability *within an operating fuel cell* is key to designing more robust configurations. However, in conventional fuel cell systems, the individual component performance characteristics are difficult to deconvolute from other contributing factors as multiple processes are interdependent on the same few variable parameters. Probing these *in-situ* mechanisms remains a significant challenge.

Third, the performance of acidic PEM-based fuel cells is primarily limited by cathode performance and membrane-related issues. The cathodic oxygen reduction reaction (ORR) remains a key challenge, particularly for acidic PEMFCs. The present "state-of-art" Pt-only nanoparticles catalysts is not be sufficient for meeting required performance and durability benchmarks for large-scale commercialization [13-15]. Sluggish kinetics and high overpotentials associated with the ORR necessitate substantial loadings of Pt-based metal catalysts to achieve adequate performance [16]. However, as mentioned previously, the high cost and limited availability of Pt necessitates the development of novel electrocatalysts which reduce or eliminate precious metal content. A wide range of alternative oxygen reduction catalysts have been explored including Pt-transition metal alloys (*e.g.*, iron, cobalt, nickel, copper) [13,17,18], ruthenium-based chalcogenides [19], metal oxides [20], transition carbides

[21], cobalt–polypyrole–carbon composites [22,23], enzymes [24,25], and pyrolized Fe(Co)/C/N systems [26], but none yet have shown the necessary combination of electrocatalytic activity, stability, and cost-effectiveness, to replace Pt-only catalysts in acidic fuel cell systems [14]. For DLFCs, the alcohol oxidation reactions on the anode are hampered by similar issues, specifically sluggish kinetics and high costs. However, these issues are less of a concern as DLFC-based power sources typically target the portable electronics market which is less cost-sensitive than the automotive market [27].

In addition to these electrocatalytic challenges, acidic PEM-based fuel cells are hampered by membrane-related challenges, notably water management and fuel crossover. In acidic fuel cells, anode dry-out occurs during operation at high current densities because of the osmotic drag of water molecules along with protons transported across the membrane, from the anode to the cathode. The osmotic drag, in combination with water formation, causes flooding of the cathode, which hampers oxygen transport to electrocatalytic sites. Also, operating fuel cells at elevated temperatures ($\geq 80\ ^{o}C$) further complicates water management, as the PEM must stay fully hydrated to maintain sufficient conductivity and performance. Several active (*i.e.,* electro-osmotic pumps) [28,29] and passive (*i.e.,* component modification) [30] water management strategies have been proposed to overcome this limitation. Unfortunately, such strategies often require ancillary components that complicate fuel cell design and reduce overall system energy density. Fuel crossover occurs when unreacted fuel migrates (via electro-osmosis and/or diffusion) through the PEM and reacts on the cathode causing mixed potentials, thereby reducing performance [31]. The crossover may be mitigated by diluting fuel streams, but this, in turn, reduces system energy density. Overcoming these performance-limiting issues requires the rational design of novel electrocatalysts and high-performance components.

1.3 Overview of Current Alkaline Fuel Cell Technology

As alkaline fuel cells (AFCs) operated at high pH regimes, hydroxyl anions are the mobile ions. A fuel combines with hydroxyl ions and electro-oxidized to generate electrons and reaction by-products. These electrons travel around an external circuit powering a load. On the cathode, oxygen combines with electrons and water, and electro-reduces to produce hydroxyl ions. To complete the circuit, the hydroxyl ions travel back through a conductive electrolyte to the anode. Any by-products generated at either electrode are removed from the fuel cell by the depleted reactant streams. Unlike acidic PEM-based fuel cells, AFCs typically employ concentrated liquid electrolytes (*e.g.*, potassium hydroxide) as hydroxyl carriers (Figure 1.4) [4].

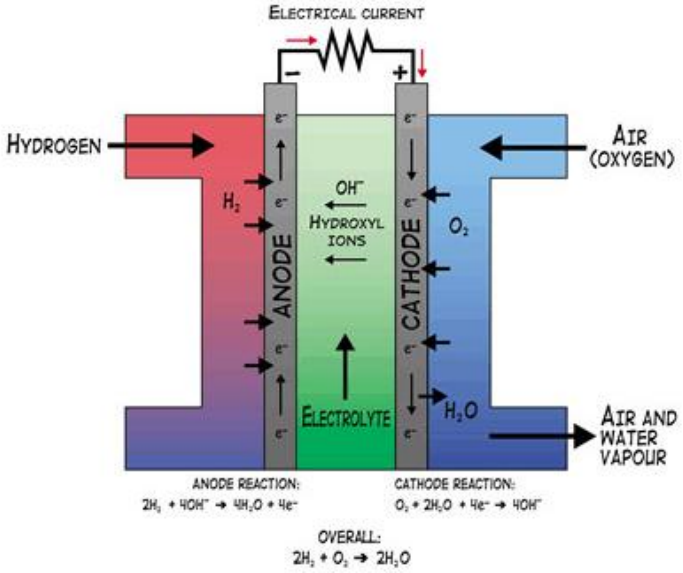

Figure 1.4. Schematic of a zero-emission hydrogen-fueled alkaline fuel cell (AFC). Hydrogen electro-oxidizes on the anode by combining with hydroxyl ions to produce electrons and water. These electrons travel around an external circuit powering a load. Oxygen (from air) combines with the electrons and water and electro-reduces to generate hydroxyl ions. The hydroxyl ions travel through a conductive liquid electrolyte (*e.g.*, KOH) which separates the electrodes and can be stagnant or flowing. Image obtained at AFC Energy PLC website [39].

AFCs overcome a number of the challenges that hamper the commercialization of acidic PEM-based fuel cells. Under alkaline conditions, alcohol oxidation and oxygen reduction kinetics are enhanced leading to improved fuel cell energetic efficiency and reduced need for

high loadings of Pt-based precious metal catalysts [32]. Furthermore, a wider range of materials are stable under alkaline conditions, compared under acidic conditions, facilitating the implementation of cheap non-noble metal catalysts (*i.e.*, silver (Ag) cathodes, nickel (Ni) anodes) as well as other inexpensive component materials (*e.g.*, Ni current collectors) which can significantly lower fuel cell costs [32,33]. Note that specific components do degrade under alkaline conditions (*e.g.*, teflonized electrodes) [34]. In addition, fuel crossover is reduced under alkaline conditions, as the hydroxyl gradient (from cathode to anode) opposes the diffusion of unreacted fuel (from anode to cathode). Consequently, AFCs have significant potential as an alternative to acidic PEM-based fuel cells for low-temperature applications [35-37].

Traditional AFCs used for vehicular studies in the 1950s and the National Aeronautics and Space Administration (NASA) Apollo space program in the 1960s were among the first successful applications of fuel cell technologies [3]. These AFC configurations utilized a stationary liquid electrolyte, typically concentrated potassium hydroxide (30-45 wt% KOH) [4]. The major technical concerns for these traditional AFCs are (*i*) electrode durability in highly caustic environments (*i.e.*, polytetrafluoroethylene degradation), (*ii*) carbonate formation when oxidizing organic fuels directly and, to a lesser extent, (*iii*) water management at the electrodes (anode flooding / cathode dry-out) [34]. Of particular importance is carbonate formation (CO_3^{2-} / HCO_3^-), which occurs when the hydroxyl ions (OH^-) present in the electrolyte react with carbon dioxide (CO_2) mainly from either organic fuel oxidation, or the environment in which the system operates (*e.g.*, tailpipe emissions from automobiles). In the presence of mobile cations, the carbonates can precipitate within the electrodes, where they damage the microporous architecture, block electrocatalytic sites, and eventually reduce performance. Furthermore, carbonate formation reduces the OH^- concentration in the liquid electrolyte, thus lowering electrolyte

conductivity and electrode kinetics. Consequently, these traditional AFCs were mainly limited to applications where cost was not a concern, which allowed for the use of high purity hydrogen (H_2) and oxygen (O_2) gas streams, thus avoiding carbonate formation related issues.

To alleviate carbonate and water management related issues, modern liquid electrolyte-based AFCs typically incorporate circulating electrolyte streams which lead improved performance and lifetime compared to AFCs with stationary electrolytes (Figure 1.4) [33,34,37-41]. The flowing electrolyte improves heat and water management and facilitates carbonate removal, which results in higher CO_2-tolerance (~100 ppm) [34]. While such flowing configurations prolong AFC lifetimes, the electrolyte solution must still be periodically replenished or replaced to maintain conductivity and prevent carbonate precipitation due to saturation over long operational lifetimes. To further extended lifetimes, liquid electrolyte-based AFC may also incorporate CO_2 scrubbers (*i.e.*, soda lime) at the oxidant inlet. However, both the scrubber and the circulating electrolyte system are ancillaries which increase parasitic losses and device complexity. Note that electrode durability in the caustic environment remains a challenge [34]. Leaking of concentrated electrolyte can also be a consumer safety concern [33].

The recent emergence of promising alkaline anion-exchange membranes (AAEMs), coupled with the aforementioned challenges associated with acidic PEM-based fuel cells, has spurred renewed interest in development of AFC systems (Figure 1.5). As an alternative to liquid electrolyte-based AFCs, novel alkaline anion exchange membrane (AAEM)-based fuel cells reduce system complexity and increase device robustness but still maintain the electrocatalytic advantages of operating under alkaline conditions [42-45]. Furthermore, AAEMs are less susceptible to carbonate precipitation because no mobile cations exist *within the membrane*, enabling less stringent operating conditions, *e.g.* air-breathing cathodes. Still, the presence of

carbonate ions in the AAEM can adversely impact cell performance (*e.g.,* unfavorable pH gradients, reduced conductivity) particularly in the case of direct liquid AAEM-based fuel cells [46]. Note, also, that carbonate precipitation on the electrodes is still possible in the presence of metal cations generated elsewhere in the fuel cell system [2]. Over the past decade AAEM technologies have made dramatic improvement in stability and conductivity; however, several key challenges remain such as high materials costs and insufficient performance and durability under fuel cell operating conditions, especially at elevated temperatures (T = 60-80 °C) [43,47]. For example, AAEM-based fuel cells, like acidic PEM-based fuel cells, are hampered by membrane limitations, notably membrane conductivity and water management at the electrodes (anode flooding / cathode dry-out) [48,49].

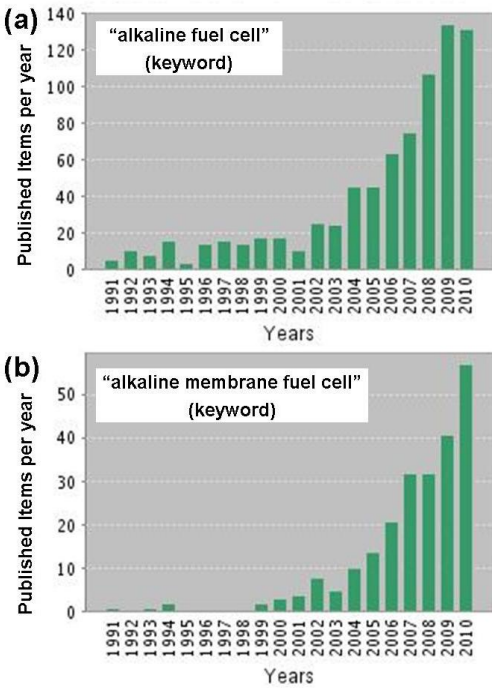

Figure 1.5. Bibliographic analysis of publication using keyword searches for **(a)** "alkaline fuel cell" and **(b)** "alkaline membrane fuel cell" in the online version of the Science Citation Index (SCI), Web of Science. SCI is a multidisciplinary database of the Institute for Scientific Information (ISI), Philadelphia, USA.

1.4 Key Remaining Challenges in the Development of Low-Temp Fuel Cells

A clear need exists for novel approaches to producing and utilizing energy in more efficient ways, in light of society's ever increasing demand as well as growing concerns with respect to climate change related to CO_2 emissions [50]. The development of low temperature fuel cell technologies will continue to play an important role in many alternative energy conversion strategies, especially for portable electronics and automotive applications. Compared to secondary batteries, fuel cells offer higher energy densities and near-instantaneous

rechargeability. With regards to internal combustion engines, fuel cell offer higher efficiencies and reduced emissions. However, widespread commercialization of acidic and alkaline fuel cell technologies has yet to be achieved mainly due to a combination of high costs (particularly of the precious metal catalysts), poor durability and, system performance limitations. To overcome the limitations of present technologies, innovative fuel cell configurations which exploit novel physicochemical concepts to simultaneously reduce costs and improve performance. Moreover, developing a better understanding of the complex electrochemical, transport and degradation processes that govern the performance and durability of novel fuel cell components, particularly catalysts and electrodes, *within operating alkaline or acidic fuel cells* is critical to designing robust, inexpensive configurations that are required for commercial introduction. The development of novel analytical platforms and techniques to probe these critical underlying processes is the focus of this thesis.

1.5 References

1. *US Energy Information Administration International Energy Outlook 2010*. Annual International Energy Outlook 2010 July 27 2010 [cited 2010 September 29]; Available from: http://www.eia.doe.gov/oiaf/ieo/index.html.
2. Borup, R., J. Meyers, B. Pivovar, Y.S. Kim, R. Mukundan, N. Garland, D. Myers, M. Wilson, F. Garzon, D. Wood, P. Zelenay, K. More, K. Stroh, T. Zawodzinski, J. Boncella, J.E. McGrath, M. Inaba, K. Miyatake, M. Hori, K. Ota, Z. Ogumi, S. Miyata, A. Nishikata, Z. Siroma, Y. Uchimoto, K. Yasuda, K.I. Kimijima, and N. Iwashita, *Scientific aspects of polymer electrolyte fuel cell durability and degradation*. Chemical Reviews, 2007. 107(10): p. 3904-3951.
3. Perry, M.L. and T.F. Fuller, *A historical perspective of fuel cell technology in the 20th century.* Journal of the Electrochemical Society, 2002. 149(7): p. S59-S67.
4. Carrette, L., K.A. Friedrich, and U. Stimming, *Fuel cells: Principles, types, fuels, and applications.* Chemphyschem, 2000. 1(4): p. 162-193.
5. Jacoby, M., *Analytics for Fuel Cells.* Chemical & Engineering News, 2009. 87(13): p. 39-41.
6. Gottesfeld, S., *Polymer Electrolyte and Direct Methanol Fuel Cells*, in *Electrochemical Engineering*, D.D. Macdonald and P. Schmuki, Editors. 2007, Viley-VCH Verlag GmbH & Co. KGaA: Weinheim. p. 544 - 661.
7. Zawodzinski, T.A. and D. Schiraldi, *The Future of Polymers for Fuel Cell Membranes.* Polymer Reviews, 2006. 46(3): p. 215 - 217.
8. Ren, X.M., P. Zelenay, S. Thomas, J. Davey, and S. Gottesfield, *Recent Advances in Direct Methanol Fuel Cells at Los Alamos National Laboratory.* Journal of Power Sources, 2000. 86: p. 111-116.
9. Rice, C., R.I. Ha, R.I. Masel, P. Waszczuk, A. Wieckowski, and T. Barnard, *Direct Formic Acid Fuel Cells.* Journal of Power Sources, 2002. 111(1): p. 83-89.

10. Thomas, S.C., X.M. Ren, S. Gottesfeld, and P. Zelenay, *Direct Methanol Fuel Cells: Progress in Cell Performance and Cathode Research.* Electrochimica Acta, 2002. 47: p. 3741-3748.
11. Demirci, U.B., *Direct liquid-feed fuel cells: Thermodynamic and environmental concerns.* Journal of Power Sources, 2007. 169(2): p. 239-246.
12. *Tekion*. 2010 [cited 2010 September 30]; Available from: http://www.tekion.com/main.htm.
13. Gasteiger, H.A., S.S. Kocha, B. Sompalli, and F.T. Wagner, *Activity benchmarks and requirements for Pt, Pt-alloy, and non-Pt oxygen reduction catalysts for PEMFCs.* Applied Catalysis B - Environmental, 2005. 56(1-2): p. 9-35.
14. Gewirth, A.A. and M.S. Thorum, *Electroreduction of Dioxygen for Fuel-Cell Applications: Materials and Challenges.* Inorganic Chemistry, 2010. 49(8): p. 3557-3566.
15. Shao-Horn, Y., W.C. Sheng, S. Chen, P.J. Ferreira, E.F. Holby, and D. Morgan, *Instability of supported platinum nanoparticles in low-temperature fuel cells.* Topics in Catalysis, 2007. 46(3-4): p. 285-305.
16. Norskov, J.K., J. Rossmeisl, A. Logadottir, L. Lindqvist, J.R. Kitchin, T. Bligaard, and H. Jonsson, *Origin of the overpotential for oxygen reduction at a fuel-cell cathode.* Journal of Physical Chemistry B, 2004. 108(46): p. 17886-17892.
17. Stamenkovic, V.R., B. Fowler, B.S. Mun, G.F. Wang, P.N. Ross, C.A. Lucas, and N.M. Markovic, *Improved oxygen reduction activity on Pt3Ni(111) via increased surface site availability.* Science, 2007. 315(5811): p. 493-497.
18. Stamenkovic, V.R., B.S. Mun, M. Arenz, K.J.J. Mayrhofer, C.A. Lucas, G.F. Wang, P.N. Ross, and N.M. Markovic, *Trends in electrocatalysis on extended and nanoscale Pt-bimetallic alloy surfaces.* Nature Materials, 2007. 6(3): p. 241-247.
19. Guinel, M.J.F., A. Bonakdarpour, B.A. Wang, P.K. Babu, F. Ernst, N. Ramaswamy, S. Mukerjee, and A. Wieckowski, *Carbon-Supported, Selenium-Modified Ruthenium-Molybdenum Catalysts for Oxygen Reduction in Acidic Media.* Chemsuschem, 2009. 2(7): p. 658-664.
20. Jorissen, L., *Bifunctional oxygen/air electrodes.* Journal of Power Sources, 2006(155): p. 23-32.
21. Meng, H. and P.K. Shen, *Novel Pt-free catalyst for oxygen electroreduction.* Electrochemistry Communications, 2006. 8(4): p. 588-594.
22. Bashyam, R. and P. Zelenay, *A class of non-precious metal composite catalysts for fuel cells.* Nature, 2006. 443(7107): p. 63-66.
23. Kothandaraman, R., V. Nallathambi, K. Artyushkova, and S.C. Barton, *Non-precious oxygen reduction catalysts prepared by high-pressure pyrolysis for low-temperature fuel cells.* Applied Catalysis B-Environmental, 2009. 92(1-2): p. 209-216.
24. Mano, N., V. Soukharev, and A. Heller, *A laccase-wiring redox hydrogel for efficient catalysis of O-2 electroreduction.* Journal of Physical Chemistry B, 2006. 110(23): p. 11180-11187.
25. Solomon, E.I., U.M. Sundaram, and T.E. Machonkin, *Multicopper oxidases and oxygenases.* Chemical Reviews, 1996. 96(7): p. 2563-2605.
26. Lefevre, M., E. Proietti, F. Jaouen, and J.P. Dodelet, *Iron-Based Catalysts with Improved Oxygen Reduction Activity in Polymer Electrolyte Fuel Cells.* Science, 2009. 324(5923): p. 71-74.
27. Dyer, C.K., *Fuel cells for portable applications.* Journal of Power Sources, 2002. 106(1-2): p. 31-34.
28. Buie, C.R., J.D. Posner, T. Fabian, C.A. Suk-Won, D. Kim, F.B. Prinz, J.K. Eaton, and J.G. Santiago, *Water management in proton exchange membrane fuel cells using integrated electroosmotic pumping.* Journal of Power Sources, 2006. 161(1): p. 191-202.
29. Yi, J.S., J.D.L. Yang, and C. King, *Water management along the flow channels of PEM fuel cells.* AIChE Journal, 2004. 50(10): p. 2594-2603.
30. Ge, S.H., X.G. Li, and I.M. Hsing, *Internally humidified polymer electrolyte fuel cells using water absorbing sponge.* Electrochimica Acta, 2005. 50(9): p. 1909-1916.
31. Kuver, A. and W. Vielstich, *Investigation of methanol crossover and single electrode performance during PEMDMFC operation - A study using a solid polymer electrolyte membrane fuel cell system.* Journal of Power Sources, 1998. 74(2): p. 211-218.

32. Spendelow, J.S. and A. Wieckowski, *Electrocatalysis of oxygen reduction and small alcohol oxidation in alkaline media.* Physical Chemistry Chemical Physics, 2007. 9(21): p. 2654-2675.
33. Gouerec, P., L. Poletto, J. Denizot, E. Sanchez-Cortezon, and J.H. Miners, *The evolution of the performance of alkaline fuel cells with circulating electrolyte.* Journal of Power Sources, 2004. 129(2): p. 193-204.
34. Cifrain, M. and K.V. Kordesch, *Advances, aging mechanism and lifetime in AFCs with circulating electrolytes.* Journal of Power Sources, 2004: p. 234-242.
35. Kordesch, K., J. Gsellmann, M. Cifrain, S. Voss, V. Hacker, R.R. Aronson, C. Fabjan, T. Hejze, and J. Daniel-Ivad, *Intermittent use of a low-cost alkaline fuel cell-hybrid system for electric vehicles.* Journal of Power Sources, 1999. 80(1-2): p. 190-197.
36. Gülzow, E., *Alkaline Fuel Cells.* Fuel Cells, 2004. 4(4): p. 251-255.
37. McLean, G.F., T. Niet, S. Prince-Richard, and N. Djilali, *An assessment of alkaline fuel cell technology.* International Journal of Hydrogen Energy, 2002. 27(5): p. 507-526.
38. *Energy Conversion Devices, Ovonic Fuel Cells*. 2010 [cited 2010 September 30]; Available from: http://www.energyconversiondevices.com/fuel.php.
39. *AFC Energy PLC.* 2010 [cited 2010 September 30]; Available from: http://www.afcenergy.com/.
40. Burchardt, T., P. Gouerec, E. Sanchez-Cortezon, Z. Karichev, and J.H. Miners, *Alkaline fuel cells: contemporary advancement and limitations.* Fuel, 2002. 81: p. 2151-2155.
41. Lin, B.Y.S., D.W. Kirk, and S.J. Thorpe, *Performance of alkaline fuel cells: A possible future energy system?* Journal of Power Sources, 2006. 161(1): p. 474-483.
42. Adams, L.A., S.D. Poynton, C. Tamain, R.C.T. Slade, and J.R. Varcoe, *A carbon dioxide tolerant aqueous-electrolyte-free anion-exchange membrane alkaline fuel cell.* Chemsuschem, 2008. 1(1-2): p. 79-81.
43. Varcoe, J.R. and R.C.T. Slade, *Prospects for alkaline anion-exchange membranes in low temperature fuel cells.* Fuel Cells, 2005. 5(2): p. 187-200.
44. Yanagi, H. and K. Fukuta, *Anion Exchange Membrane and Ionomer for Alkaline Membrane Fuel Cells (AMFCs).* ECS Transactions, 2008. 16(2): p. 257-262.
45. Lu, S.F., J. Pan, A.B. Huang, L. Zhuang, and J.T. Lu, *Alkaline polymer electrolyte fuel cells completely free from noble metal catalysts.* Proceedings of the National Academy of Sciences of the United States of America, 2008. 105(52): p. 20611-20614.
46. Wang, Y., L. Li, L. Hu, L. Zhuang, J.T. Lu, and B.Q. Xu, *A feasibility analysis for alkaline membrane direct methanol fuel cell: thermodynamic disadvantages versus kinetic advantages.* Electrochemistry Communications, 2003. 5(8): p. 662-666.
47. Varcoe, J.R., R.C.T. Slade, and E. Lam How Yee, *An alkaline polymer electrochemical interface: a breakthrough in application of alkaline anion-exchange membranes in fuel cells.* Chemical Communications, 2006(13): p. 1428-1429.
48. Varcoe, J.R., R.C.T. Slade, G.L. Wright, and Y.L. Chen, *Steady-state dc and impedance investigations of H_2/O_2 alkaline membrane fuel cells with commercial Pt/C, Ag/C, and Au/C cathodes.* Journal of Physical Chemistry B, 2006. 110(42): p. 21041-21049.
49. Zeng, R., S.D. Poynton, J.P. Kizewski, R.C.T. Slade, and J.R. Varcoe, *A novel reference electrode for application in alkaline polymer electrolyte membrane fuel cells.* Electrochemistry Communications, 2010. 12(6): p. 823-825.
50. Whitesides, G.M. and G.W. Crabtree, *Perspective: Don't Forget Long-Term Fundamental Research in Energy.* Science 2007. 315: p. 796-798.

Chapter 2

Membraneless Microfluidic Fuel Cells: Literature Overview and Remaining Opportunities*

2.1 Introduction

Fuel cell-based systems hold promise as alternative power sources for a range of applications due to their high efficiency, high energy density, and low emissions [1-3]. Acidic polymer electrolyte membrane (PEM)-based fuel cells, which utilize hydrogen or small organics as fuel, are considered most promising configurations for low temperature applications (*i.e.*, portable electronics, automotive transport) [4,5]. While such configurations have enjoyed moderate success in niche applications (*i.e.*, military, telecommunication, stationary) [6,7]; to date, large-scale commercialization efforts have been frustrated by a combination of high system costs (platinum (Pt) catalysts, Nafion membranes), insufficient durability, and system performance limitations as detailed in Chapter 1 [4]. To overcome the limitations of present technologies, innovative fuel cell configurations which exploit novel physicochemical concepts to simultaneously reduce costs and improve performance are needed [8]. Membraneless fuel cells which utilize microscale transport phenomena (laminar flow regime) are a promising alternative to PEM-based fuel cells for low-temperature applications [9]. Here, two different membraneless microfluidic fuel cell designs are presented (*i*) laminar flow-based fuel cells (LFFCs) as power sources and (*ii*) microfluidic hydrogen-oxygen (H_2/O_2) fuel cells as electro-analytical platforms for catalyst and electrode development.

* Part of this work has been published: F.R. Brushett, P.J.A Kenis, A. Wieckowski, "New Concepts in the Chemistry and Engineering of Low Temperature Fuel Cells", *Fuel Cell Science: Theory, Fundamentals, and Biocatalysis*, A. Wieckowski & J.K. Norskov, editors, (John Wiley & Sons, Inc.), pg. 565-610.

2.2 Multi-stream Laminar Flow Concept

Microfluidics can be defined as the science and engineering of fluidic and transport phenomena within structures with at least one characteristic dimension in the range of tens to hundreds of micrometers [10,11]. At the microscale, fluid flow is typically laminar and characterized by low Reynolds numbers (Re < ~2100) such that viscous effects dominate over inertial effects and surface forces are more relevant than body forces. Consequently, multiple streams may merge side by side in a single microchannel with only diffusive mixing occurring in between adjacent streams [12]. This precise control over transport properties enables a wide range of applications, including, but not limited to, cell studies, separations, and nanoparticle syntheses [10]. The Kenis group [13-16] and others [9] have exploited these microfluidic phenomena to develop a class of *membraneless* fuel cells that are also referred to as laminar flow-based fuel cells (LFFCs, Figure 2.1). In these applications, the laminar nature of flow eliminates the need for a physical barrier, such as an expensive PEM, while still allowing for ionic transport between the anode and cathode.

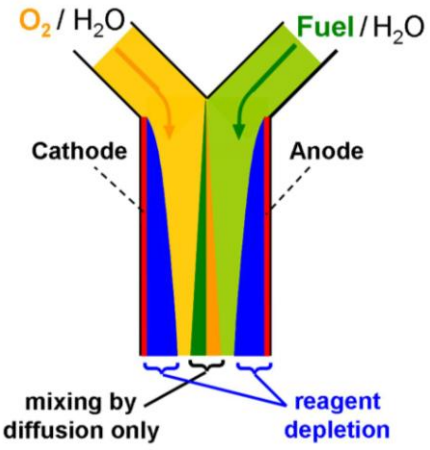

Figure 2.1. Schematic of a Y-shaped laminar flow-based fuel cell (LFFC). The electrodes are the catalyst-coated microchannel sidewalls (red lines). The cell operates by flowing an anodic fuel stream (green) and a cathodic oxygen-saturated stream (yellow) in parallel. Though not shown, both streams generally include a supporting electrolyte to enhance conductivity and maintain pH. The reaction depletion zones at the electrodes and diffusional mixing zones at the liquid-liquid interface are both highlighted (not drawn to scale). Image reprinted with the permission of Professor Paul J.A. Kenis.

2.3 Key Benefits of Membraneless Microfluidic Fuel Cell Design

As power sources, membraneless fuel cells overcome a number of challenges that hinder the performance of membrane-based fuel cells, (see sections 1.2 and 1.3), including fuel crossover, water management, by-product removal and electrode reaction kinetics.

- **Fuel crossover can be minimized by adjusting cell dimensions and stream flow rates [13,14,17].** For example, with operation of a membraneless fuel cell at a high Péclet number (*i.e.*, Pe >3000) the stream-wise convective velocity dominates the transverse diffusive velocity, thus restricting diffusive mixing to a narrow interfacial width at the center of the channel that broadens as a function of downstream position and mean velocity [13]. In addition, Jayashree *et al.* demonstrated that fuel crossover may be further reduced in membraneless fuel cells by hydrodynamically focusing the fuel into a thin stream on the anode by varying the stream flow rate ratios; thus widening the envelope of operating conditions [17]. Thus, compared to conventional membrane-based direct methanol fuel cells (DMFCs), membraneless DMFCs based laminar flow phenomena, exhibit higher open circuit potentials and consequently improved fuel cell efficiencies [18]. Moreover, unlike mixed reactant DMFCs, which are based on single mixed stream of fuel and oxidant, membraneless DMFCs do not require selective, but less active, methanol-tolerant cathode catalysts (*e.g.*, ruthenium-based chalcogenides) [19].
- **Water management issues are absent in all-aqueous membraneless fuel cells.** Thus challenges such as electrode dryout / flooding and stream humidification, which hamper both acidic and alkaline membrane-based fuel cells, can be avoided.
- **The flowing streams also remove by-products of electrode reactions.** This enables operation of membraneless alkaline direct liquid fuel cells (DLFCs) such as membraneless

alkaline DMFCs. The constantly refreshing electrolyte removes by-products such as any formed carbonates from the electrode surface, and hinders the development of adverse pH gradients (detailed in section 1.3) [18,20,21].

- **The composition of the fuel, electrolyte and oxidant streams can be specified independently**. This not only allows for operation of membraneless fuel cells with different fuels and different media (*i.e.*, acidic, alkaline, mixed), but also enables optimization of reaction kinetics at the individual electrodes [15,20,22,23]. By placing an external reference electrode (*e.g.*, off-the-shelf Ag/AgCl in saturated NaCl, BASi) at the fuel cell outlet, anode and cathode performance characteristics can easily be independently monitored in an operating fuel cell [15]. Recently, Brushett *et al.* demonstrated the benefits of stream flexibility by investigating LFFC performance with five different fuels (formic acid, methanol, ethanol, hydrazine and sodium borohydride) in either acidic or alkaline media [20]. Operating under alkaline conditions significantly improves methanol and ethanol oxidation kinetics and stabilizes sodium borohydride. Independent specification and autonomous control of stream properties (*i.e.*, pH) enables the operation of unusual fuel cell configurations such as mixed-media fuel cells [15,23] and biological fuel cells [24,25].

In addition to these operational advantages, the membraneless fuel cells benefit from high surface area to volume ratios and cheap component fabrication techniques, both of which facilitate the development of inexpensive high energy density microscale fuel cell systems [9].

2.4 Overview of Current Membraneless Microfluidic Fuel Cell Technology

Since the inception of microfluidic-based fuel cells in 2002, a wide array of membraneless architectures have been developed, including a commercial venture, INI Power Systems (Morrisville NC), based on technology developed in the Kenis group at the University of Illinois

at Urbana-Champaign [26]. In a seminal publication, Choban *et al.* demonstrated one of the earliest microfluidic fuel cells employing a Y-shaped microchannel design with aqueous anode and cathode streams of formic acid and dissolved oxygen in sulfuric acid (H_2SO_4) solution, respectively (Figure 2.2a) [13]. The fuel cell consisted of two precision-machined graphite plates horizontally aligned to form a Y-channel and sealed on the top and bottom by a polydimethylsiloxane (PDMS) and polycarbonate layers, respectively. Anode (Pd black) and cathode (Pt black) nanoparticle catalysts were electrodeposited onto the opposing channel side-walls. The multilayer structure was held together using binder clips enabling rapid assembly and disassembly. This initial design demonstrated peak current and power densities of ~ 14 mA/cm^2 and 5 mW/cm^2 due to mass transport limitations at the cathode [13]. Furthermore, fuel utilization per pass was only 0.04 % primarily due to the limiting cathode performance characteristics [16]. The cause of these cathode restrictions are two-fold: (*i*) the low diffusivity

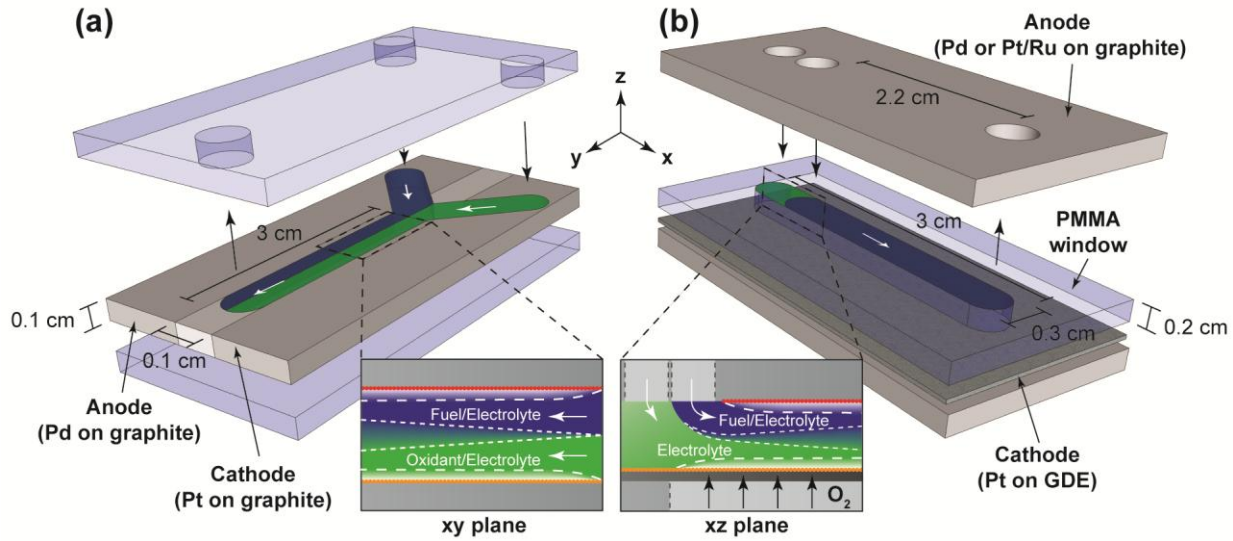

Figure 2.2. Schematic designs of: **(a)** first generation LFFC operated by flowing a fuel stream (blue) and an oxygen-saturated electrolyte stream (green) in parallel; **(b)** second generation LFFC operated by flowing a fuel stream (blue) and an electrolyte stream (green) in parallel with the oxygen entering through a porous gas diffusion electrode (GDE) which serves as the cathode. The inserts schematically show reaction depletion and diffusional mixing zones at the electrodes and at the liquid–liquid interface, respectively. Reprinted from Journal of Power Sources, 195, R.S. Jayashree, S.K. Yoon, F.R. Brushett, P.O. Lopez-Montesinos, D. Natarajan, L.J. Markoski, P.J.A. Kenis, On the performance of membraneless laminar flow-based fuel cells, 3569-3578, 2010 with permission from Elsevier.

of oxygen in solution (~ $2x10^{-5}$ cm^2/s) and (*ii*) the low dissolved oxygen saturation concentrations (1 - 4 mM), both of which cannot sufficiently replenish the depletion boundary layer that forms on the cathode.

The cathode limitations of early fuel cell designs can also be overcome by the introduction of an air-breathing cathode into the membraneless architecture [16-20]. This passive configuration benefits from the relatively high concentrations (~ 10 mM) and high diffusivity of oxygen (~ $2x10^{-1}$ cm^2/s) in the ambient environment. Jayashree *et al.* demonstrated a first membraneless fuel cell with an integrated air-breathing cathode (Figure 2.2b) [16]. The fuel cell consisted of a polymethylmethacrylate (PMMA) window which forms the microfluidic channel, a graphite plate coated with Pd nanoparticles as an anode, and a Toray carbon paper gas diffusion electrode covered with Pt nanoparticles as a cathode. The anode and cathode streams enter the cell through inlets bored into the graphite plate and travel through the microchannel in a vertically-oriented laminar fashion. An aqueous mixture of formic acid and sulfuric acid is used for the anode stream. As oxygen is now supplied to the cathode directly from ambient environment, the cathode stream is only a conductive electrolyte (*i.e.*, H_2SO_4) that serves as a barrier to fuel crossover. Implementation of the air-breathing cathode resulted in a 5-fold increase in the peak power density and a 10-fold increase in the maximum current density under near-identical operating conditions [16,17], compared to the performance of the first LFFC as reported by Choban *et al.* [13].

Another possible strategy to reduce these cathode limitations is the use of oxidants that are soluble at higher concentrations than those of dissolved oxygen, such as hydrogen peroxide, potassium permanganate and hypochlorite bleach [21,27-29]. Use of high energy density liquid oxidants is challenging. For example, hydrogen peroxide reduction is often coupled with

decomposition that leads to vigorous gaseous oxygen evolution, which perturbs the laminar regime and often leads to two-phase behavior [27]. These adverse effects can be mitigated by: (*i*) operating at low concentrations [30], (*ii*) introducing a third stream to reduce interfacial interactions [31], (*iii*) utilizing alternative catalysts (*e.g.*, gold) to minimize undesired oxidant decomposition [29], and/or (*iv*) optimizing the electrode architecture (*e.g.*, porous gas diffusion electrodes, grooved microstructure) to quickly utilize the gaseous oxygen [27,32]. Recently, Kjeang *et al.* presented an alkaline microfluidic fuel cell operating with formate and hypochlorite bleach which produced no gaseous products [21]. Note that microfluidic-based fuel cell systems that utilize liquid oxidants must store and pump these additional fluids, which lead to increases in parasitic losses and device complexity.

For all membraneless fuel cell designs, a trade-off exists between maximizing power density and fuel utilization. For example, the *power density* of a membraneless fuel cell can be improved by reducing the electrode-to-electrode distance, increasing the stream flow rates and/or increasing the fuel concentrations. Unfortunately, all of these improvements hamper both *fuel utilization* and system efficiency. By decreasing the electrode-to-electrode gap, the cell resistances are minimized and power density increases. However, an inter-electrode gap that is too small will enhance fuel crossover, thus negatively affecting the *maximum* power density and also reducing fuel utilization. Moreover, in terms of from the balance of plant (BOP), parasitic losses will increase as a result of an increase in pressure drop in narrower channels. Increasing the stream flow rates can improve cell performance by minimizing both fuel crossover, as a result of shorter residence times, and the boundary layer thickness, as a result of enhanced mass transport through a thinner depletion boundary layer. However, increasing the stream flow rates directly increases parasitic losses associated with pumping. Furthermore, the shortened

residence time decreases fuel utilization as the fuel has less time to diffuse to and react at the anode. Increasing the fuel concentration improves cell performance by enhancing mass transport to the anode through the depletion boundary layer, due to the increased concentration gradients. But increasing fuel concentration increases the extent of fuel crossover, thus reversing the desired increase in power density. In addition, fuel utilization again decreases because of the fuel crossover, and because a significant fuel fraction must remain unreacted to maintain the high concentration gradients. On the other hand, fuel utilization may be increased by reducing fuel concentration and stream flow rates, both of which significantly lower cell power density.

Enhancing both fuel utilization and overall power density is a challenging task that requires different strategies, including novel operating methods and innovative cell designs. For example, Jayashree *et al.* optimized power density and fuel utilization of an air-breathing membraneless fuel cell by varying operational parameters such as stream flow rates and stream ratios, and structural parameters such as channel length, and electrode-to-electrode distance [17]. By hydrodynamic focusing the fuel to a thin stream on the anode, the authors were able to increase the fuel utilization up to 38% without reducing stream flow rates or increasing fuel crossover. Using such a focusing technique, both fuel utilization and power density may be increased as it enables the use of higher concentrations of fuel and oxidant. Altering structural parameters of the microchannel in which the reactants flow can further improve performance and fuel utilization [33-37]. For example, Ahmed *et al.* developed a "trident-shaped" design that used electrolyte stream in the channel center to focus both the fuel and oxidant streams onto their respective electrodes [34]. In another interesting example, Yoon *et al.* investigated different active and passive methods of minimizing the depletion boundary layer which limits cell performance: (*i*) using multiple outlets to remove the depleted regions; (*ii*) using multiple inlets

to replenish the depleted regions; and (*iii*) using a herringbone structure to generate secondary transverse flow enabling chaotic mixing within a single laminar stream, to replace the depleted layer with fluid of higher fuel concentration [33]. In all three examples, the performance improvements obtained from the design modifications must be balanced with either the increased system complexity and parasitic pumping losses associated with additional fluidic streams, or the possibility of increased fuel crossover associated with the chaotic advection. Another strategy to improve both cell performance and fuel utilization is to increase the electrode surface area to further exploit the high surface area to volume ratio in the microscale fuel cells. By introducing porous high surface area electrode structures, instead of directly depositing catalysts on channel sidewalls, Kjeang and co-workers have developed several promising microfluidic-based fuel cell

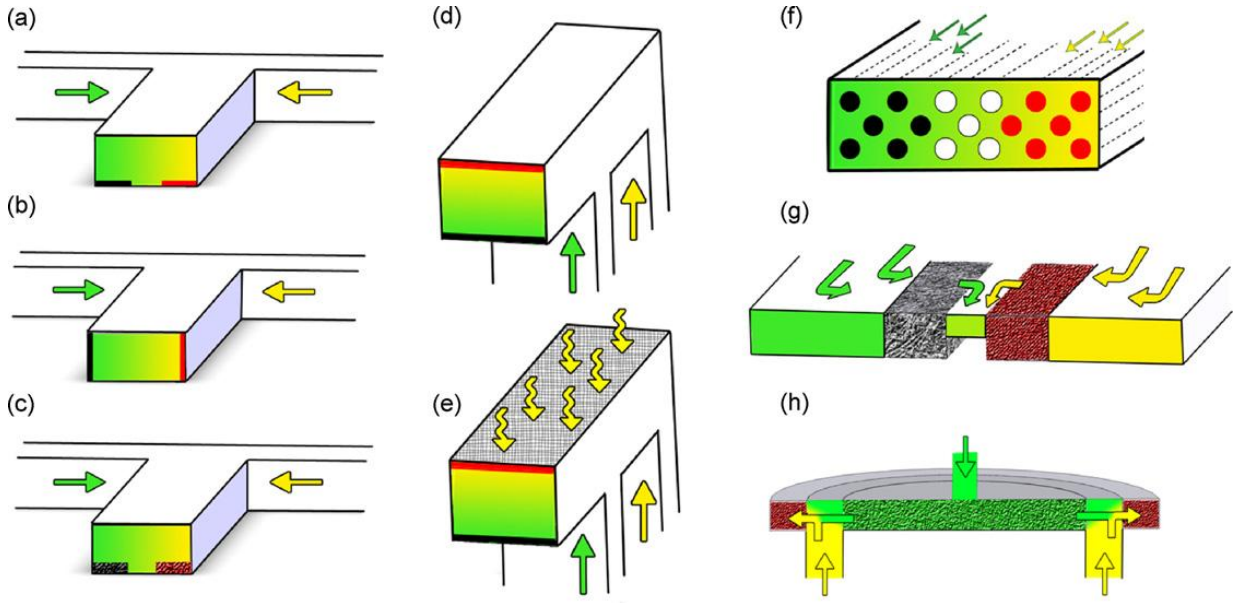

Figure 2.3. Schematic of variety of laminar flow-based microfluidic fuel cell architectures. Laminar streaming, characteristic of microfluidic liquid flows, facilitates the separation of fuel and oxidant in the absence of a membrane. Each architecture is shown with fuel in green, oxidant in yellow, cathodes in red, anodes in black, and porous electrodes textured. Two streams are combined horizontally in a T- or Y-channel with **(a)** electrodes on bottom, **(b)** electrodes on sides, and **(c)** porous electrodes on bottom. **(d)** An F-channel configuration, and **(e)** with the addition of a porous electrode to facilitate air-breathing. **(f)** An electrode array microfluidic fuel cell. **(g)** A flow through porous electrode microfluidic fuel cell. **(h)** A radial porous electrode fuel cell architecture. Reprinted from Journal of Power Sources, 186, E. Kjeang, N. Djilali, D. Sinton, Microfluidic fuel cells: A review, 353-369, 2009 with permission from Elsevier.

configurations that utilize so-called flow-through electrode architectures to improve both fuel utilization and power density [21,27,38-40]. Note that these flow-through configurations would suffer from significant parasitic pumping losses. For further reading, a recent comprehensive review by Kjeang *et al.* provides an excellent summary of the present microfluidic-based fuel cell technologies. In this review, the authors highlight a range of fascinating novel configuration and compare the performance of each (Figure 2.3) [9].

Transitioning from these laboratory-scale "proof-of-concept" configurations to commercially-viable microfluidic fuel cell-based power sources is a present challenge. In addition to general engineering challenges associated with designing conventional fuel cell system, several unique design constraints exist for membraneless fuel cells. As the membraneless fuel cell technologies are based on microscale phenomena, large-scale fuel cell systems must *scale-out* rather than scale-up to maintain the laminar flow regime. Indeed, while a variety of structural and operating parameters can be adjusted to improve the performance of microfluidic fuel cells, the system design is dependent on the explicit intended application with specific power and operational lifetime requirements as well as weight and volume restrictions. First, to obtain a certain absolute power level, a certain number of individual membraneless fuel cells will need to be arranged in an array. Second, to avoid having to integrate the capability to circulate the fluids within the BOP, a larger number of membraneless fuel cells can be run at lower power density but optimized fuel utilization in a single pass. Alternatively, one can run fewer cells at higher power density but low fuel utilization per pass (say 25 %) in a fuel and electrolyte recirculation scenario. The latter case would make more sense for a larger system that is desired to run for an extended period of time. On the basis of this scaling-out concept, INI

Power Systems have successfully developed a 900-channel 100-W prototype direct methanol LFFC-based system [26,41].

While microfluidic-based fuel cells have several key advantages over membrane-based fuel cells, specifically system cost and flexibility, both configurations are hampered by similar long-term durability issues. Thus, for the successful commercialization membraneless technologies, the performance and durability of individual components, particularly catalysts and electrodes, must be fully characterized and optimized under realistic operating conditions. A detailed knowledge of the fundamental processes that govern the working lifetime of these novel systems is required for rational design and development of robust and cost-effective devices.

2.5 Microfluidic Hydrogen-Oxygen Fuel Cells as Electro-Analytical Platforms

Membraneless microfluidic fuel cells operate based on a fine balance between transport phenomena and electrode kinetics. In addition to addressing water management and fuel crossover issues, these laminar flow-based systems allow for the independent specification of individual stream compositions (*e.g.*, pH). Furthermore, the use of a liquid electrolyte, rather than a stationary polymeric membrane, enables the simple *in-situ* analysis of individual electrode performance using an off-the-shelf reference electrode. *These advantages can be leveraged to develop microfluidic fuel cells as versatile electro-analytical platforms for the characterization and optimization of catalysts and electrodes for both membrane- and membraneless fuel cells applications.*

As highlighted in Chapter 1, developing a better understanding of the complex interplay of electrochemical, transport, and degradation processes that govern the performance of novel catalysts and electrodes *within an operating fuel cell* is key to designing robust fuel cells for commercialization [4,42-45]. However, detailed analysis of novel catalyst embedded in gas

diffusion layer within the membrane-electrode assembly (MEAs) of actual working fuel cell is challenging as other factors such as water management, uneven performance across the electrodes, and temperature gradients complicate elucidation of the individual processes taking place at the electrodes. Too many processes are interdependent on the same few variable parameters, necessitating the development of analytical platforms with high degrees of freedom.

To this end, a pH-flexible microfluidic hydrogen-oxygen (H_2/O_2) fuel cell as an analytical platform has been developed that enables the study of electrochemical, transport, and degradation processes at the two electrodes *independently*, without factors such as water management complicating the experiment and data analysis (Figure 2.4) [46-49]. Though

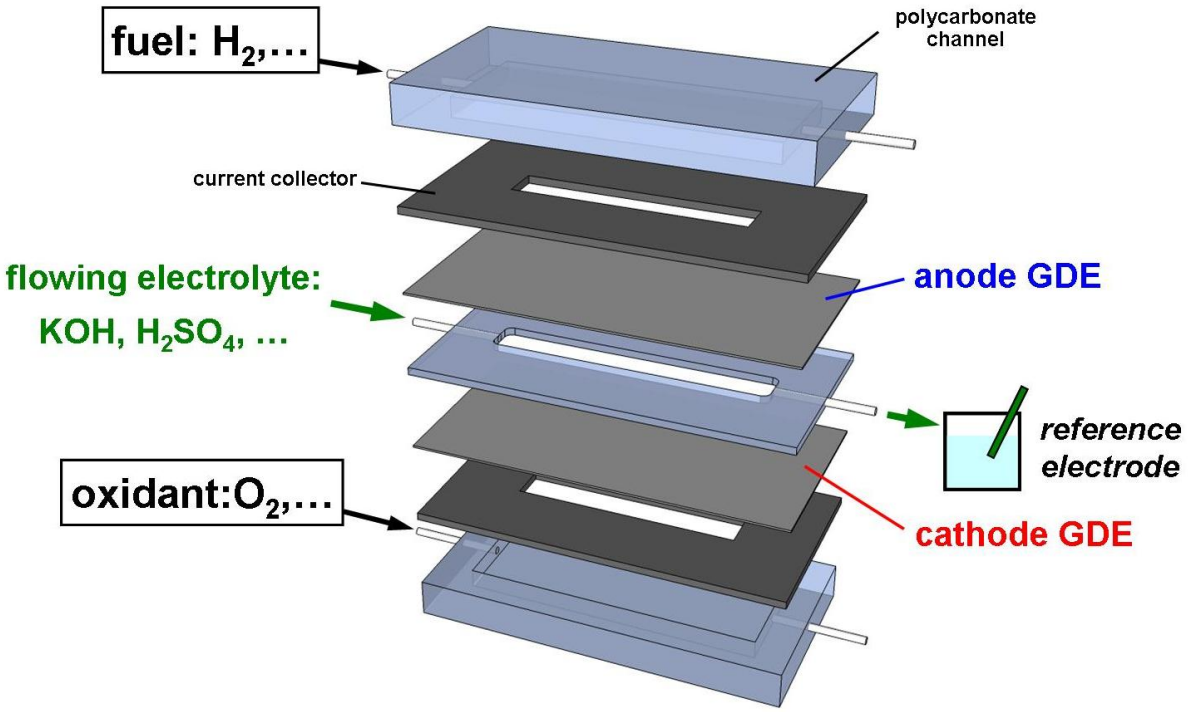

Figure 2.4. A modular schematic of a pH-flexible microfluidic H_2/O_2 fuel cell that serves as a catalyst / electrode characterization platform. A flowing electrolyte stream is separated from gaseous reactant streams by two gas diffusion electrodes (GDEs) with a catalyst-coated side interfacing with the electrolyte. Two graphite windows function as current collectors on either side of the GDEs and polycarbonate flow chambers for reactant delivery. An external reference electrode is placed in an electrolyte collection beaker for monitoring individual electrode performance characteristics. Both the reactant and electrolyte streams can be independently-modulated to create the "operating condition of choice" for analytical investigations.

originally-developed as a microscale power source [46], this configuration helps to bridge the tremendous gap between the traditional characterization of catalyst structure and activity within a three-electrode electrochemical cell and analyses of catalyst/electrode performance and durability within actual fuel cell systems. For analytical investigations, the flowing stream (*i*) enables autonomous control over electrolyte parameters (*i.e.*, pH, composition) and consequently the local electrode environments, as well as (*ii*) allows for the independent *in-situ* analyses of catalyst and/or electrode performance and degradation characteristics via an external reference electrode (*i.e.*, Ag/AgCl in saturated NaCl). Thus, this microfluidic analytical platform enables a high number of experimental degrees of freedom, previously limited to a three-electrode electrochemical cell, to be employed in the construct of working fuel cell.

In prior work, Brushett *et al.* have demonstrated the utility of pH-flexible microfluidic platform as a catalyst / electrode characterization tool by analyzing the performance of Pt/C and Ag/C cathode catalysts in an operating fuel cell under varying alkaline conditions [47]. Furthermore, the performance and long-term stability of Pt and Pt-M alloys cathode catalysts have been investigated as a function of acidic conditions [48]. These preliminary investigations show the utility of the microfluidic analytical platform as a bridge between the capabilities and limitations of traditional electrochemical cells and the actual operational environment of fuel

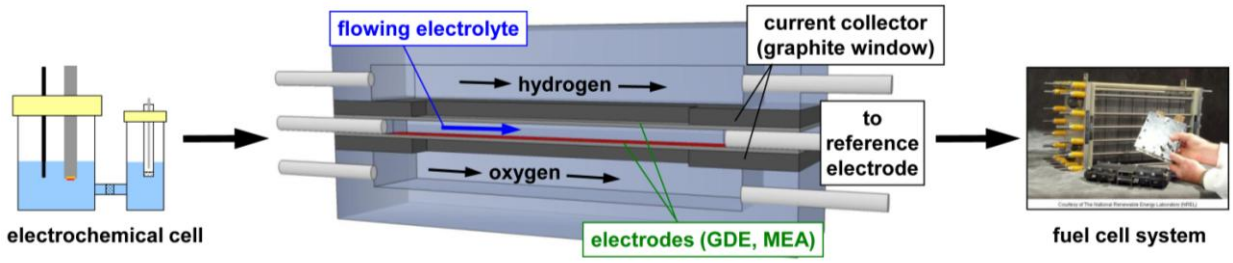

Figure 2.5. Bridging the gap between traditional three-electrode electrochemical cells and actual working fuel cell systems by employing a microfluidic H_2/O_2 fuel cell, as a versatile electro-analytical platform, for *in-situ* catalyst / electrode investigations.

cells (Figure 2.5). For these studies, the key is the flowing electrolyte stream, which enables precise control and analysis of the local electrode environments and facilitates the study of interfacial phenomena and the optimization of electrode / MEA design.

2.6 Topics Studied in this Thesis

Building on this preliminary work, the focus of this thesis is to provide critical insight into the following research areas:

- Identify the key processes that govern the electrode performance and durability in alkaline fuel cells as a function of preparation methods and operating parameters **(Chapter 3)**.
- Determine the suitability of a novel Pt-free oxygen reduction reaction catalyst embedded in gas diffusion electrodes for acidic and alkaline fuel cell applications **(Chapter 4)**.
- Establish electrode structure-activity relationships by aligning *in-situ* electrochemical analyses with *ex-situ* microtomographic (MicroCT) structural analyses **(Chapter 5)**.
- Investigate the feasibility and utility of a microfluidic-based vapor feed direct methanol fuel cell (VF-DMFC) configuration as a power source for portable applications **(Chapter 6)**.

In all these areas, the information garnered from these *in-situ* analytical platforms will advance the development of more robust and cost-effective electrode configurations and thus more durable and commercially-viable fuel cell systems (*both membrane-based and membraneless*).

2.7 References

1. Carrette, L., K.A. Friedrich, and U. Stimming, *Fuel cells: Principles, types, fuels, and applications.* Chemphyschem, 2000. **1**(4): p. 162-193.
2. Perry, M.L. and T.F. Fuller, *A historical perspective of fuel cell technology in the 20th century.* Journal of the Electrochemical Society, 2002. **149**(7): p. S59-S67.
3. Jacoby, M., *Analytics for Fuel Cells.* Chemical & Engineering News, 2009. **87**(13): p. 39-41.
4. Borup, R., J. Meyers, B. Pivovar, Y.S. Kim, R. Mukundan, N. Garland, D. Myers, M. Wilson, F. Garzon, D. Wood, P. Zelenay, K. More, K. Stroh, T. Zawodzinski, J. Boncella, J.E. McGrath, M. Inaba, K. Miyatake, M. Hori, K. Ota, Z. Ogumi, S. Miyata, A. Nishikata, Z. Siroma, Y. Uchimoto, K. Yasuda, K.I. Kimijima, and N.

Iwashita, *Scientific aspects of polymer electrolyte fuel cell durability and degradation.* Chemical Reviews, 2007. **107**(10): p. 3904-3951.

5. Gasteiger, H.A., S.S. Kocha, B. Sompalli, and F.T. Wagner, *Activity benchmarks and requirements for Pt, Pt-alloy, and non-Pt oxygen reduction catalysts for PEMFCs.* Applied Catalysis B - Environmental, 2005. **56**(1-2): p. 9-35.
6. *Tekion*. 2010 [cited 2010 September 30]; Available from: http://www.tekion.com/main.htm.
7. *Ballard Power Systems*. 2010 [cited 2010 October 1]; Available from: http://www.ballard.com/.
8. Brushett, F.R., P.J.A. Kenis, and A. Wieckowski, *New Concepts in the Chemistry & Engineering of Low Temperature Fuel Cells*, in *Fuel Cell Science: Theory, Fundamentals, and Bio-Catalysis*, A. Wieckowski and J.K. Norskov, Editors. 2010, John Wiley & Sons, Inc.: Hoboken. p. 565-610.
9. Kjeang, E., N. Djilali, and D. Sinton, *Microfluidic fuel cells: A review.* Journal of Power Sources, 2009. **186**(2): p. 353-369.
10. Whitesides, G.M., *The origins and the future of microfluidics.* Nature, 2006. **442**(7101): p. 368-373.
11. Squires, T.M. and S.R. Quake, *Microfluidics: Fluid physics at the nanoliter scale.* Reviews of Modern Physics, 2005. **77**(3): p. 977-1026.
12. Kenis, P.J.A., R.F. Ismagilov, and G.M. Whitesides, *Microfabrication inside capillaries using multiphase laminar flow patterning.* Science, 1999. **285**(5424): p. 83-85.
13. Choban, E.R., L.J. Markoski, A. Wieckowski, and P.J.A. Kenis, *Microfluidic fuel cell based on laminar flow.* Journal of Power Sources, 2004: p. 54-60.
14. Markoski, L.J., P.J.A. Kenis, and E.R. Choban, *Fuel cells comprising laminar flow induced dynamic conducting interfaces, electronic devices comprising such cells and method employing same*, US Patent 7,252,898, 7 August 2007.
15. Choban, E.R., J.S. Spendelow, L. Gancs, A. Wieckowski, and P.J.A. Kenis, *Membraneless laminar flow-based micro fuel cells operating in alkaline, acidic, and acidic/alkaline media.* Electrochimica Acta, 2005. **50**(27): p. 5390-5398.
16. Jayashree, R.S., L. Gancs, E.R. Choban, A. Primak, D. Natarajan, L.J. Markoski, and P.J.A. Kenis, *Air-breathing laminar flow-based microfluidic fuel cell.* Journal of the American Chemical Society, 2005. **127**(48): p. 16758-16759.
17. Jayashree, R.S., S.K. Yoon, F.R. Brushett, P.O. Lopez-Montesinos, D. Natarajan, L.J. Markoski, and P.J.A. Kenis, *On the Performance of Membraneless Laminar Flow-Based Microfluidic Fuel Cells.* Journal of Power Sources, 2010. **195**: p. 3569-3578.
18. Jayashree, R.S., D. Egas, J.S. Spendelow, D. Natarajan, L.J. Markoski, and P.J.A. Kenis, *Air-breathing laminar flow-based direct methanol fuel cell with alkaline electrolyte.* Electrochemical and Solid State Letters, 2006. **9**(5): p. A252-A256.
19. Whipple, D.T., R.S. Jayashree, D. Egas, N. Alonso-Vante, and P.J.A. Kenis, *Ruthenium cluster-like chalcogenide as a methanol tolerant cathode catalyst in air-breathing laminar flow fuel cells.* Electrochimica Acta, 2009. **54**(18): p. 4384-4388.
20. Brushett, F.R., R.S. Jayashree, W.P. Zhou, and P.J.A. Kenis, *Investigation of Fuel and Media Flexible Laminar Flow-Based Fuel Cells.* Electrochemica Acta, 2009. **54**.
21. Kjeang, E., R. Michel, D.A. Harrington, D. Sinton, and N. Djilali, *An alkaline microfluidic fuel cell based on formate and hypochlorite bleach.* Electrochimica Acta, 2008. **54**(2): p. 698-705.
22. Choban, E.R., P. Waszczuk, and P.J.A. Kenis, *Characterization of limiting factors in laminar flow-based membraneless microfuel cells.* Electrochemical and Solid State Letters, 2005. **8**(7): p. A348-A352.
23. Cohen, J.L., D.J. Volpe, D.A. Westly, A. Pechenik, and H.D. Abruna, *A dual electrolyte H_2/O_2 planar membraneless microchannel fuel cell system with open circuit potentials in excess of 1.4 V.* Langmuir, 2005. **21**(8): p. 3544-3550.
24. Moore, C.M., S.D. Minteer, and R.S. Martin, *Microchip-based ethanol/oxygen biofuel cell.* Lab on a Chip, 2005. **5**(2): p. 218-225.
25. Topcagic, S. and S.D. Minteer, *Development of a membraneless ethanol/oxygen biofuel cell.* Electrochemica Acta, 2006. **51**(11): p. 2168-2172.

26. *INI Power Systems, www.inipower.com.* 2008 2008 [cited 2009 July 31st].
27. Kjeang, E., A.G. Brolo, D.A. Harrington, N. Djilali, and D. Sinton, *Hydrogen peroxide as an oxidant for microfluidic fuel cells.* Journal of the Electrochemical Society, 2007. **154**(12): p. B1220-B1226.
28. Lopez-Montesinos, P.O., N. Yossakda, A. Schmidt, F.R. Brushett, W.C. Pelton, and P.J.A. Kenis, *Fabrication and characterization of a planar, silicon-based, monolithically integrated micro laminar flow fuel cell (μLFFC) with a bridge-shaped microchannel cross-section.* submitted, 2010.
29. Gu, L.F., N. Luo, and G.H. Miley, *Cathode electrocatalyst selection and deposition for a direct borohydride/hydrogen peroxide fuel cell.* Journal of Power Sources, 2007. **173**(1): p. 77-85.
30. Li, A., S.H. Chan, and N.T. Nguyen, *A laser-micromachined polymeric membraneless fuel cell.* Journal of Micromechanics and Microengineering, 2007. **17**(6): p. 1107-1113.
31. Sun, M.H., G.V. Casquillas, S.S. Guo, J. Shi, H. Ji, Q. Ouyang, and Y. Chen, *Characterization of microfluidic fuel cell based on multiple laminar flow.* Microelectronic Engineering, 2007: p. 1182-1185.
32. Stroock, A.D., S.K.W. Dertinger, A. Ajdari, I. Mezic, H.A. Stone, and G.M. Whitesides, *Chaotic mixer for microchannels.* Science, 2002. **295**(5555): p. 647-651.
33. Yoon, S.K., G.W. Fichtl, and P.J.A. Kenis, *Active control of the depletion boundary layers in microfluidic electrochemical reactors.* Lab on a Chip, 2006. **6**(12): p. 1516-1524.
34. Ahmed, D.H., H.B. Park, and H.J. Sung, *Optimum geometrical design for improved fuel utilization in membraneless micro fuel cell.* Journal of Power Sources, 2008. **185**(1): p. 143-152.
35. Park, H.B., D.H. Ahmed, K.H. Lee, and H.J. Sung, *An H-shaped design for membraneless micro fuel cells.* Electrochimica Acta, 2009. **54**(18): p. 4416-4425.
36. Salloum, K.S., J.R. Hayes, C.A. Friesen, and J.D. Posner, *Sequential flow membraneless microfluidic fuel cell with porous electrodes.* Journal of Power Sources, 2008. **180**(1): p. 243-252.
37. Phirani, J. and S. Basu, *Analyses of fuel utilization in microfluidic fuel cell.* Journal of Power Sources, 2008. **175**(1): p. 261-265.
38. Kjeang, E., J. McKechnie, D. Sinton, and N. Djilali, *Planar and three-dimensional microfluidic fuel cell architectures based on graphite rod electrodes.* Journal of Power Sources, 2007. **168**(2): p. 379-390.
39. Kjeang, E., R. Michel, D.A. Harrington, N. Djilali, and D. Sinton, *A microfluidic fuel cell with flow-through porous electrodes.* Journal of the American Chemical Society, 2008. **130**(12): p. 4000-4006.
40. Kjeang, E., B.T. Proctor, A.G. Brolo, D.A. Harrington, N. Djilali, and D. Sinton, *High-performance microfluidic vanadium redox fuel cell.* Electrochimica Acta, 2007. **52**(15): p. 4942-4946.
41. Hollinger, A.S., R.J. Maloney, R.S. Jayashree, D. Natarajan, L.J. Markoski, and P.J.A. Kenis, *Nanoporous separator and low fuel concentration to minimize crossover in direct methanol laminar flow fuel cells.* Journal of Power Sources, 2010. **195**(11): p. 3523-3528.
42. Kucernak, A.R. and E. Toyoda, *Studying the oxygen reduction and hydrogen oxidation reactions under realistic fuel cell conditions.* Electrochemistry Communications, 2008. **10**(11): p. 1728-1731.
43. Hizir, F.E., S.O. Ural, E.C. Kumbur, and M.M. Mench, *Characterization of interfacial morphology in polymer electrolyte fuel cells: Micro-porous layer and catalyst layer surfaces.* Journal of Power Sources, 2010. **195**(11): p. 3463-3471.
44. Kim, S., M. Khandelwal, C. Chacko, and M.M. Mench, *Investigation of the Impact of Interfacial Delamination on Polymer Electrolyte Fuel Cell Performance.* Journal of the Electrochemical Society, 2009. **156**(1): p. B99-B108.
45. Ramasamy, R.P., E.C. Kumbur, M.M. Mench, W. Liu, D. Moore, and M. Murthy, *Investigation of macro- and micro-porous layer interaction in polymer electrolyte fuel cells.* International Journal of Hydrogen Energy, 2008. **33**(13): p. 3351-3367.
46. Jayashree, R.S., M. Mitchell, D. Natarajan, L.J. Markoski, and P.J.A. Kenis, *Microfluidic Hydrogen Fuel Cell with a Liquid Electrolyte.* Langmuir, 2007. **23**: p. 6871-6874.
47. Brushett, F.R., W.P. Zhou, R.S. Jayashree, and P.J.A. Kenis, *Alkaline Microfluidic Hydrogen-Oxygen Fuel Cell as a Cathode Characterization Platform.* Journal of the Electrochemical Society, 2009. **156**(5): p. B565-B571.

48. Brushett, F.R., H.T. Duong, J.W.D. Ng, A. Wieckowski, and P.J.A. Kenis, *Investigation of Pt, Pt_3Co and Pt_3Co/Mo cathodes for the Oxygen Reduction Reaction in an Acidic Microfluidic H_2/O_2 Fuel Cell.* Journal of the Electrochemical Society, 2010. **157**(6): p. B837-B845.
49. Brushett, F.R., M.S. Thorum, N.S. Lioutas, M.S. Naughton, C. Tornow, H.R. Jhong, A.A. Gewirth, and P.J.A. Kenis, *A Carbon-Supported Copper Complex of 3,5-Diamino-1,2,4-triazole as a Cathode Catalyst for Alkaline Fuel Cell Applications.* Journal of the American Chemical Society, 2010. **132**(35): p. 12185-12187.

Chapter 3

Analysis of Pt/C-based Electrode Performance in an Alkaline Fuel Cell

3.1 Introduction

Despite some niche successes, the widespread commercialization of present acidic polymer electrolyte membrane (PEM)-based fuel cell technologies has yet to be realized due to high system costs (*i.e.*, catalysts, membranes), insufficient durability and, to a lesser extent, system performance limitations (*i.e.*, water management) [1-3]. Operating fuel cells under alkaline conditions, compared to acidic conditions, is advantageous as enhanced organic fuel oxidation and oxygen reduction kinetics improve fuel cell energetic efficiency [4] and enable the use of cheaper non-precious metal catalysts (*i.e,* silver (Ag) cathode, nickel (Ni) anodes) that can dramatically reduce overall fuel cell system costs [5]. Due to perceived carbonate formation issues, research into alkaline fuel cells (AFCs) has been limited as compared to acidic PEM-based fuel cells [6]. However, with the advent of novel anion-exchange membrane technologies, AFCs are a renewed avenue of exploration [7-10]. Consequently, AFCs have significant potential as an alternative to acidic PEM-based fuel cells for low-temperature applications [11-13]. A more detailed description of the present status of AFC technologies may be found in section 1.3.

Developing a better understanding of the complex electrochemical, transport, and degradation processes that govern the performance and durability of electrodes within operating fuel cells is critical to designing robust, inexpensive configurations that are required for commercial introduction [14-17]. However, detailed *in-situ* investigations of individual electrode processes are complicated by other factors such as water management, uneven

performance across electrodes, and temperature gradients. Indeed, too many processes are interdependent on the same few variable parameters, necessitating analytical platforms with many degrees of freedom. To address these challenges, a pH-flexible microfluidic H_2/O_2 fuel cell has been developed for catalyst and electrode characterization (Figure 3.1) [18-20]. For analytical investigation, the flowing electrolyte (*i*) minimizes adverse fuel cell system limitations (*i.e.,* water management) (*ii*) enables independent control of electrolyte parameters (*i.e.*, pH, composition) and consequently local electrode environments, and (*iii*) allows for *in-situ* studies of single electrode performance via an external reference electrode [18-21].

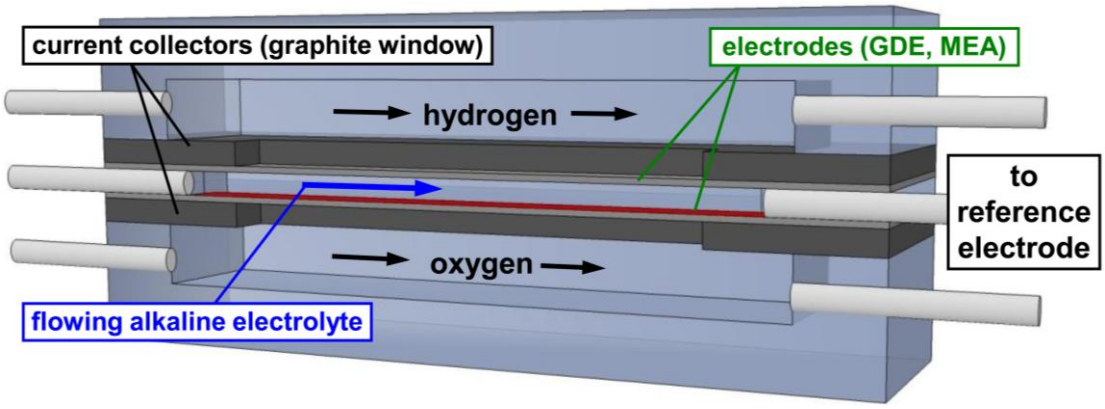

Figure 3.1. Microfluidic H_2/O_2 fuel cell with an independently-controlled flowing alkaline electrolyte stream separated from gaseous reactant streams by two gas diffusion electrodes (GDEs), with the catalyst-coated side interfacing with the electrolyte. Two graphite windows function as current collectors on either side of the GDEs and polycarbonate flow chambers for reactant delivery. An external reference electrode is placed in an electrolyte collection beaker for monitoring individual electrode performance characteristics.

Here, the utility of this versatile analytical platform is demonstrated with a focus on the development of AFC technologies due to aforementioned promise and relative lack of study of these systems compared to their acidic counterparts. The performance and durability of Pt/C-based electrodes in an operating AFC are investigated as a function of electrode preparation protocols (*i.e.,* hot-pressing, acclimation) and cell operating parameters (*i.e.,* electrolyte composition). Furthermore, the impact of carbonates on individual electrode and overall fuel

cell performance is simulated by introducing the contaminants via the flowing electrolyte stream. Developing a detailed understanding of the key factors that govern the performance of electrodes within operating AFCs will be critical to furthering the development of robust and cost-effective liquid- and alkaline anion exchange membrane (AAEM)-based systems.

3.2 Experimental

3.2.1 Gas Diffusion Electrode Preparation

For each electrode, a catalyst ink was prepared by mixing 8 mg of commercial Pt/C (50% mass on Vulcan carbon, E-Tek), 5.33 mg polytetrafluoroethylene (PTFE, Aldrich) powder as the hydrophobic catalyst binder, 200 µL Millipore water (18.2 MΩ) and 200 µL isopropyl alcohol. Previously, the optimal weight percentage of PTFE to the total weight of the PTFE / catalyst mixture within the catalyst ink was determined to be 40 wt% [18]. This catalyst ink was sonicated (Branson 3510) for 1 hr to obtain a uniform mixture, which was then painted onto the hydrophobized carbon side of a Toray carbon paper gas diffusion layer (EFCG "S" type electrode, E-Tek) to create a gas diffusion electrode (GDE). The GDE was sintered under a nitrogen (N_2) atmosphere at 330 °C for 20 min in a preheated tube furnace (Lindberg/Blue) [22]. Then, certain fabricated GDEs were hot pressed (Carver 3851-0) at a pressure of approximately 340 psi (~2344 kPa) and a temperature of ~125 ± 10 °C for 5 min. The geometric GDE surface area was 4 cm^2 (4 (L) x 1 (W) cm^2). For all the electrodes studied, the total catalyst loading was 2 mg Pt/C /cm^2 with a metal loading of 1 mg Pt/cm^2.

3.2.2 Fuel cell Assembly and Testing

Two GDEs, anode and cathode, were placed on opposite sides of a 0.15-cm thick polymethylmethacrylate (PMMA) sheet, such that the catalyst-covered sides interfaced with the

3-cm long and 0.33-cm wide precision-machined window in the PMMA. The window has an inlet and an outlet on either side such that the aqueous electrolyte flows between the electrodes. Two 0.1-cm thick graphite plates with access windows (3.8 (L) x 0.7 (W) cm^2) are placed on the outside of the GDEs and served as current collectors. The reactant gas flow chambers (5 (L) x 1 (W) x 0.5 (H) cm^3) were precision-machined into polycarbonate sheets. The multilayer assembly was held together using binder clips. Prior to experimentation, the fuel cell assembly was leak tested by flowing deionized water through the fluidic chamber for several minutes. In the few cases leaking was observed, typically due to misalignment of the layers, the cell was disassembled and realigned. No leaking was observed during subsequent operation.

Fuel cell experiments were conducted using General Purpose Electrochemical Software (GPES, EcoChemie) controlled by a potentiostat (Autolab PGSTAT-30, EcoChemie). H_2 and O_2 gas (laboratory grade, S.J. Smith) are each fed at a flow rate of 50 sccm [19]. Potassium hydroxide (KOH, Mallinckrodt, 88%, balance of H_2O), sodium hydroxide (NaOH, Fisher Chemical, 98.2%), and potassium carbonate (K_2CO_3, Fisher Chemical, 99.8%) were used as aqueous alkaline electrolytes. Electrolyte flow rates were varied from 0.0 to 0.9 mL/min using a syringe pump (2200 PHD, Harvard Apparatus). Once the gas and liquid streams were introduced, the fuel cell was held at open circuit potential (OCP) for 5 min to ensure that the cell potential stabilized prior to testing. Fuel cell polarization curves were obtained by steady-state chronoamperometric measurements at different cell potentials. The geometric surface area used to calculate current and power density is 1 cm^2 (based on the electrolyte channel length and width). After exiting the fuel cell, the aqueous electrolyte stream collects in a beaker. The anode and cathode polarization losses are independently characterized using multimeters (15 XP Meterman, 87 III Fluke, or 179 Fluke) by placing a reference electrode (Ag/AgCl in saturated

NaCl, BASi) in the collection beaker [18-20]. No potential drop is observed along the plastic tubing (Cole Parmer, 1.57 mm ID) connecting the fuel cell and the reference electrode [21]. The open circuit potential of the Pt/C anode, exposed to 50 sccm H_2, was used to calibrate the reference electrode to the reversible hydrogen electrode (RHE) scale.

Electrochemical impedance spectroscopy (EIS) measurements were performed on the fuel cell using a Frequency Response Analyzer (FRA, EcoChemie) module controlled by a potentiostat (Autolab PGSTAT-30, EcoChemie). The spectra were recorded in constant voltage mode by decreasing frequencies from 10 kHz to 30 mHz at 9 points/decade. The modulating voltage was 10 mV root mean squared. Impedance measurements were performed at a cell potential of 0.4 V, coinciding with the peak power density of the cells studied. The high frequency x-axis intercepts represent the internal cell resistance (R_{cell}) which includes both electrolyte solution resistance and component contact resistances. The individual semi-circular features in the Nyquist plots were fitted with parallel RC equivalent circuits replacing the pure capacitive elements (C_{dl}) with constant phase elements (C_{cpe}) to describe the porous nature of the GDE [23]. The diameter of the medium-frequency semicircular feature represents the charge-transfer resistance (R_{ct}) associated with the Faradaic processes on the fuel cell electrodes. The low-frequency features represent the effects of mass transport limitations on fuel cell processes [24].

3.3 Results and Discussion

3.3.1 Effects of Acclimatization on Electrode Performance

After preparation, all the GDEs demonstrated significant hydrophobicity due to the presence of excess PTFE on the surface preventing catalyst wetting. To remove excess binder from the three-phase interface, *in-situ* cyclic voltammetry was performed on the electrodes within the

microfluidic fuel cell. Acclimation studies were conducted within the microfluidic fuel cell with gaseous N_2 and H_2 streams (50 sccm each) to create working electrode and counter / reference electrodes, respectively. A flowing acidic electrolyte of 0.5 M sulfuric acid (H_2SO_4, GFS Chemicals) was used because hydrogen oxidation kinetics are faster under acidic conditions than under alkaline conditions [25]. Using the dynamic hydrogen electrode (DHE) as a counter / reference electrode, the working electrode was cycled between 0.05 and 1.15 V vs. DHE at a scan rate of 0.5 V/s in 10 min intervals. After each interval, the microfluidic electrolyte-electrode assembly was inverted such that the working electrode became the counter / reference electrode and the counter / reference electrode became the working electrode. The second electrode was then acclimated under identical conditions. After acclimation sets were performed, both electrodes were removed from the microfluidic fuel cell, rinsed with Millipore water (18.2 MΩ) to remove any residues, and dried under a laboratory hood. Electrode performance was then investigated in the re-assembled microfluidic H_2/O_2 fuel cell operated with 1 M KOH flowing at 0.6 mL/min.

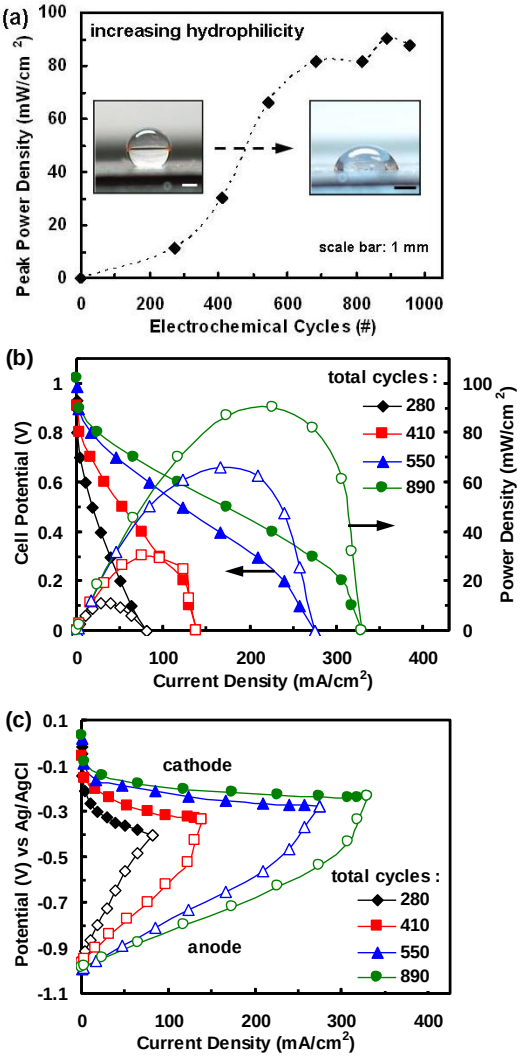

Figure 3.2. Pt/C-PTFE electrode acclimation studies via *in-situ* cyclic voltammetry in the microfluidic fuel cell. **(a)** Peak power density as a function of electrochemical cycles. **(b)** Representative polarization and power density curves as a function of cycles (280, 410, 550, and 890). **(c)** Corresponding individual anode and cathode polarization curves. Studies were performed at room temperature with 50 sccm H_2/O_2 flow rates, and 1 M KOH at 0.6 mL/min.

Figure 3.2 shows individual electrode and overall alkaline microfluidic H_2/O_2 fuel cell performance as a function of electrochemical acclimation cycles. Prior to cycling, the extreme electrode surface hydrophobicity coupled with the PMMA channel hydrophilicity leads to electrolyte plug / slug behavior in the microfluidic channel where the electrolyte wets the channel sidewalls but not the electrode surfaces. Consequently, initial fuel cell testing (at 0 electrode cycles) was not possible. As cycling removed excess PTFE, electrode surface hydrophilicity increased and the performance of the fuel cell dramatically improved (Figure 3.2a). As shown in Figure 3.2b, fuel cell peak power densities (PPDs) of 11.4, 30.4, 66.4, and 90.4 mW/cm^2 after 280, 410, 550, and 890 electrode cycles, respectively. Furthermore, fuel cell open circuit potentials (OCPs) of 0.93, 0.91, 0.99, and 1.02 V after 280, 410, 550, and 890 cycles, respectively. No further enhancements were observed with additional cycling. Figure 3.2c shows that the improved surface wetting enhances individual electrode performance by facilitating reactant transport to the catalytic sites, in this case water to the cathode and hydroxyl ions to the anode. Additional cycling was limited to prevent the electrode from becoming too hydrophilic which would lead to catalyst layer flooding and reduce cell performance.

3.3.2 Effects of Hot-pressing on Electrode Performance at 1 M KOH

For liquid-based fuel cells, hot-pressing is intended to compact the catalyst layer into the gas diffusion media to minimize electrical contact resistances and to prevent catalyst delamination into the flowing electrolyte stream [5,18,20,22]. For membrane-based fuel cells, membrane-electrode assemblies (MEAs) are also hot-pressed during fabrication to minimize contact resistances between interfacing layers [26]. In addition, pressure is also applied to the fuel cell stack during operation to prevent gas leaks and to ensure minimal contact resistance losses [27]. However, over-compression and uneven pressure distribution, which are both common in fuel

cell systems, can damage the intricate electrode microstructure leading to losses in porosity and hydrophobicity and consequently to reductions in performance and durability [14,27,28].

The effects of hot-pressing on the electrode performance are investigated in the an alkaline microfluidic H_2/O_2 fuel cell operated at varying 1 M KOH flow rates. While, a 1 M KOH concentration is lower than those typically used for liquid-based electrolyte AFCs, the pH (~14) more closely resembles the operating environment of membrane-based AFCs [29,30]. Figure 3.3 shows the performance of the fuel cell operated with hot-pressed (HP) and non hot-pressed (non-HP) electrodes as a function of electrolyte flow rate (0.0, 0.3, 0.6, and 0.9 mL/min) at 1 M KOH.

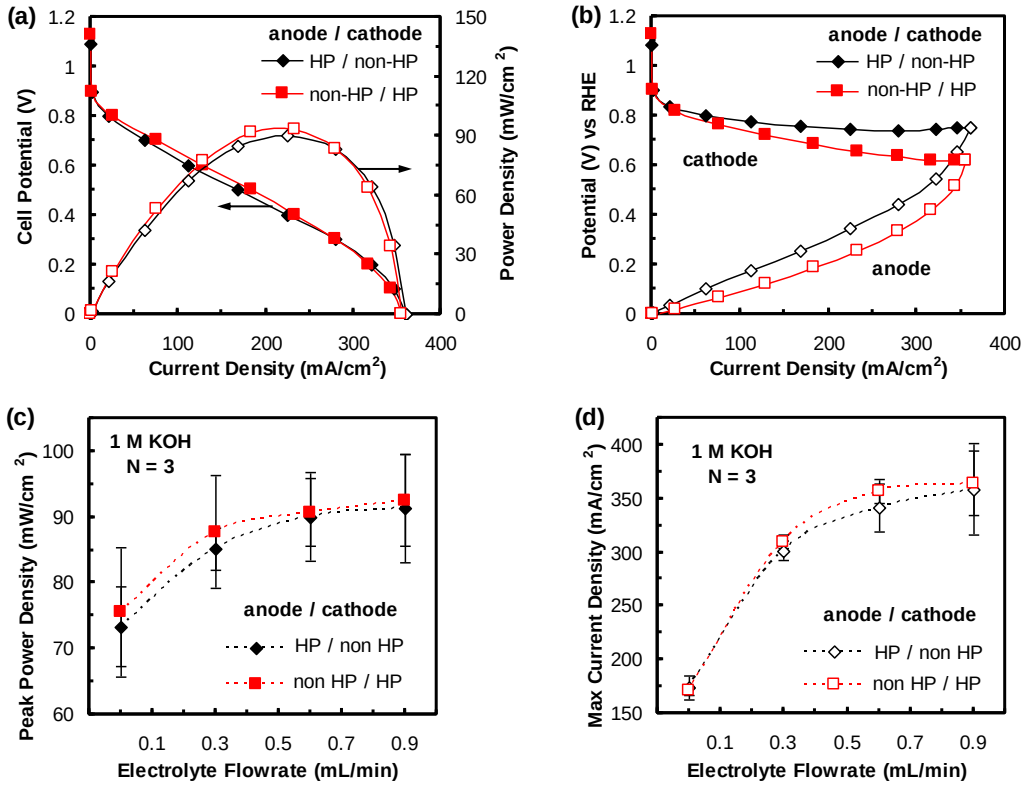

Figure 3.3. The two alkaline microfluidic H_2/O_2 fuel cell configurations studied at 1 M KOH are: HP anode / non-HP cathode (black diamonds) and non-HP anode / HP cathode (red squares). **(a)** Representative polarization and power density curves for cell operated with each configuration at 0.6 mL/min. **(b)** Corresponding anode and cathode polarization curves. **(c)** Peak power and **(d)** maximum current densities of the cell operated with each configuration as a function of electrolyte flowrate. Error bars represent a standard deviation in either direction from the average value at each flowrate (N = 3). Studies were performed at room temperature with 50 sccm H_2/O_2 flow rates, and 1 M KOH flowing electrolyte.

Furthermore, the effect of hot-pressing on electrode function, *i.e.*, oxygen reduction at the cathode or hydrogen oxidation at the anode, was studied by inverting the microfluidic electrolyte-electrode assembly between experiments. Figure 3.3a shows representative polarization and power density curves of the fuel cell at 0.6 mL/min utilizing: a HP anode and a non-HP cathode (HP anode / non-HP cathode); or a non-HP anode and a HP cathode (non-HP anode / HP cathode). For both configurations, the OCPs and PPDs are very similar with the non-HP anode / HP cathode configuration slightly outperforming the HP anode / non-HP cathode configuration. Both configurations appear to be mass transport-limited in high current density regimes. While the overall fuel cell performances are near identical, the corresponding individual anode and cathode polarization curves show that hot-pressing adversely impacts electrode performance (Figure 3.3b). For both configurations, the anode is the performance-limiting electrode and the non-HP anode outperforms the HP anode. Under these operating conditions, conclusions on the impact of hot-pressing on cathode performance are difficult to draw (discussed in detail below). Despite these differences, overall fuel cell performance is similar because the system is limited by the low electrolyte concentration. Under alkaline conditions, hydrogen oxidation on Pt occurs via a two-step process that requires two hydroxyl ions to diffuse to the anode surface and react with the hydrogen to form water and two electrons [31,32]. The low hydroxyl ion concentration in the electrolyte not only leads to low conductivity (ohmic losses) but also to anodic mass transport limitations as the rate of hydroxyl replenishment of the depletion boundary layer is insufficient.

Analyses of fuel cell peak power (Figure 3.3c) and maximum current densities (V_{cell} = 0 V, Figure 3.3d) as a function of electrolyte flow rate further highlight the impact of transport phenomena at 1 M KOH. Both peak power and maximum current densities improve with

increasing electrolyte flow rate. Higher electrolyte flow rates help to reduce the hydroxyl ion depletion gradient and, also, to improve water management, particularly water removal at the anode. The maximum current densities are more sensitive to electrolyte flow rate than peak power densities as more hydroxyl ions are required and more water molecules are generated. For both configurations, the peak power and maximum current densities appear to plateau around an electrolyte flow rate of 0.6 mL/min. At this point, the microfluidic configuration is no longer limited by hydroxyl replenishment at the anode though the system remains mass transport-limited by the low electrolyte concentration. Under all conditions, the non-HP anode / HP cathode configuration slightly outperforms the HP anode / non-HP cathode configuration due enhanced anode performance.

An interesting potential drift phenomenon was observed at high current density regimes where both the anode and cathode potentials shifted upwards, in the positive directions. This transient phenomenon is best illustrated by the fuel cell operated with the HP anode / non-HP cathode configuration (Figure 3.4a). The anode potential shift can be attributed to the low electrolyte concentration and poor water management at the HP anode which cause a decrease in local pH and; thus, a Nernstian shift in electrode potential. Because the fuel cell was

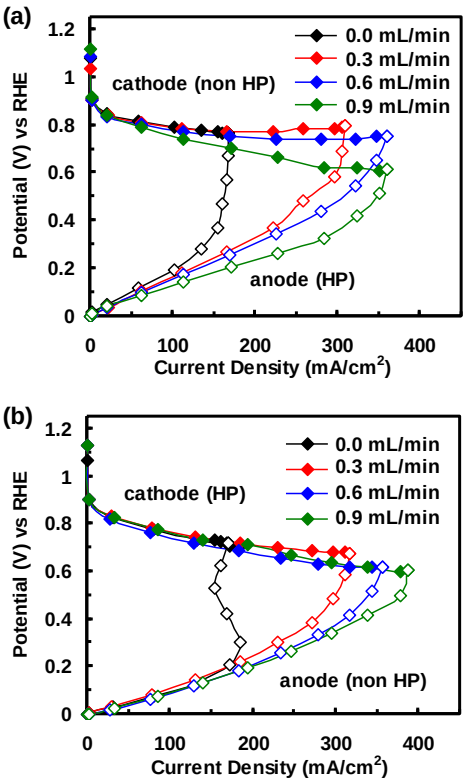

Figure 3.4. Representative individual anode and cathode polarization curves as a function of electrolyte flow rate (0.0, 0.3, 0.6 and 0.9 mL/min). Cells were operated in a **(a)** HP anode / non-HP cathode configuration and in a **(b)** non-HP anode / HP cathode configuration. Studies were performed at room temperature with 50 sccm H_2/O_2 flow rates, and flowing 1 M KOH.

operated in a potentiostatic mode, a constant potential must be maintained between electrodes; thus, the cathode potential also shifts upwards. Increasing the electrolyte flow rate reduced the drift phenomenon as hydroxyl ion gradients are minimized and water management at the anode is improved. Again, the performance appears to plateau at 0.6 mL/min electrolyte flow rate due to electrolyte concentration limitations. Note that the performance at 0.9 mL/min of the fuel cell operated with HP anode / non-HP cathode configuration is similar to that of cell operated with non-HP anode / HP cathode configuration (Figure 3.4b). This observation suggests that (*i*) enhanced flow rate can significantly improve anode performance and (*ii*) any conclusions regarding the impact of hot-pressing on cathode performance are difficult to draw as cell performance seems to be dominated by effects of anode performance and electrolyte flow rate. Similar individual electrode and overall cell behavior were observed by Zeng *et al.* in a H_2/O_2 fuel cell with an AAEM of varying thicknesses and an *in-situ* Pd-Pt reference electrode [33].

3.3.3 Effects of Hot-pressing on Electrode Performance at 3 M KOH

Further studies on the effects of hot-pressing on the electrode performance are investigated in an alkaline microfluidic H_2/O_2 fuel cell operated at varying flow rates of 3 M KOH. The higher KOH concentration addresses the electrolyte-based transport limitation in the previous section and enables access to higher current density regimes where electrode-based limitations may be studied. Figure 3.5 shows the performance of the fuel cell operated with a HP anode / non-HP cathode configuration and a non-HP anode / HP cathode configuration as a function of 3 M KOH flow rate (0.0, 0.3, 0.6, and 0.9 mL/min). Figure 3.5a shows representative polarization and power density curves for the each fuel cell configuration at a 0.6 mL/min electrolyte flow rate. While, the OCPs and PPDs are near identical for each fuel cell configurations, at high current densities, the non-HP anode / HP cathode configuration markedly outperforms the HP anode /

non-HP cathode configuration. The corresponding individual anode and cathode polarization curves indicate that mass transport effects, specifically water removal, limit the performance of the HP anode (Figure 3.5b). The HP and non-HP cathodes show identical performances suggesting that hot-pressing does not significantly impact the cathode performance (discussed in detail below). This result confirms that the difference in cathode performance observed at 1 M KOH was influenced by anode limitations, specifically the transient potential drift phenomena. Furthermore, unlike at 1 M KOH, the fuel cell performance is not limited by electrolyte concentration at 3 M KOH.

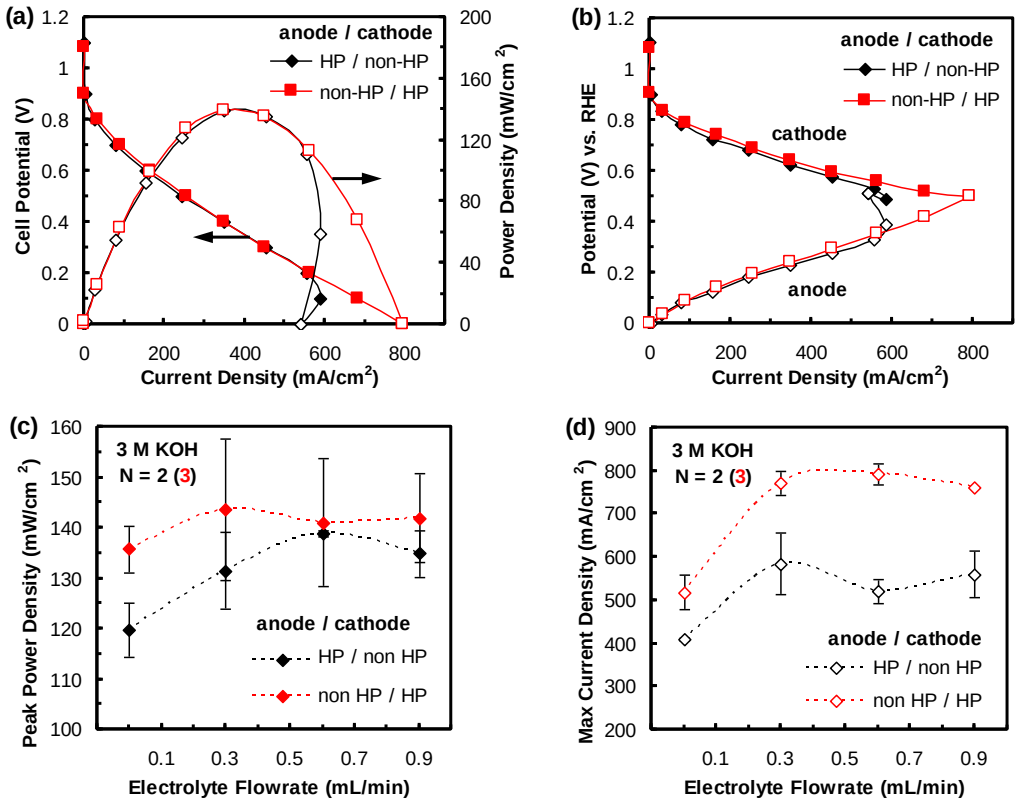

Figure 3.5. The two alkaline microfluidic H_2/O_2 fuel cell configurations studied at 3 M KOH are: HP anode / non-HP cathode (black diamonds) and non-HP anode / HP cathode (red squares). **(a)** Representative polarization and power density curves for cell operated with each configuration at 0.6 mL/min. **(b)** Corresponding anode and cathode polarization curves. **(c)** Peak power and **(d)** maximum current densities of the cell operated with each configuration as a function of electrolyte flow rate. Error bars represent a standard deviation in either direction from the average value at each flow rate (N = 2 or 3). Studies were performed at room temperature with 50 sccm H_2/O_2 flow rates, and 3 M KOH flowing electrolyte.

Further performance analyses as a function of peak power (Figure 3.5c) and maximum current densities (V_{cell} = 0 V, Figure 3.5d) at varying 3 M KOH flow rates (0.0, 0.3, 0.6, and 0.9 mL/min) also demonstrate the effects of hot-pressing electrodes. Under static conditions (0.0 mL/min), fuel cells operated with a non-HP anode / HP cathode outperform those operated with a HP anode / non-HP cathode in terms of both peak power and maximum current density. This performance enhancement is due to improved internal water management, specifically water removal, in the non-HP anode. In a stagnant electrolyte, mass transport limitations hinder cell performance as water formed at the anode does not diffuse from the electrode surface rapidly enough, particularly at higher current densities, leading to the formation of hydroxyl depletion layer. Consequently, cell performance is hindered by water formation at the anode which leads to a local electrolyte dilution (hydroxyl depletion gradient) and, to a lesser extent, anode catalyst layer flooding. By increasing the electrolyte flow rate, fuel cell performance is enhanced, especially at higher current densities, as the dynamic electrolyte stream facilitates the water removal from the anode surface which minimizes the hydroxyl depletion boundary layer. Under dynamic conditions (0.3, 0.6, and 0.9 mL/min), similar peak power densities are observed for both fuel cell configurations. However, at maximum current densities, the fuel cell operated with a non-HP anode / HP cathode outperforms that operated with a HP anode / non-HP cathode, as shown in Figures 3.5a and 3.5b. Here, large quantities of formed water must be rapidly removed from the anode necessitating optimal transport processes within the GDE structure. These results suggest that hot-pressing adversely affects water management within electrodes as fuel cells with non-HP anodes significantly outperform fuel cells with HP anodes.

For all 3 M KOH studies, cathode performance was both flow rate and hot-pressing independent. This is because internal cathode water management is not a concern as water is a

reactant in the alkaline ORR. Moreover, as the electrolyte is mostly water, increasing flow rate has minimal effect on reactant diffusion to the cathode surface. Also, no catalyst delamination was observed suggesting that hot-pressing may not enhance catalyst layer stability. Thus, hot-pressing appears to have negative effects on water transport processes within the GDE architecture which are likely due to changes in porosity as well as shifts in layer hydrophobicity. These *in-situ* results are supported by previously reported *ex-situ* studies by Bazylak *et al.* on the effects of compression on GDL microstructure and water management [28]. Microtomographic analyses of effects of hot-pressing on three-dimensional electrode structure may be found in Chapter 5. From here on, all fuel cell studies are performed using a non-HP anode / HP cathode configuration. Moreover, for all further fuel cell studies the electrolyte flow rate is held at 0.3 mL/min where peak power and maximum current densities appear to plateau for 3 M KOH.

In earlier work, Brushett *et al.* characterized the performance of Pt/C- and Ag/C-based cathodes using an identical alkaline microfluidic H_2/O_2 fuel cell with 2-mm electrode-to-electrode gap [18]. A Pt/C-based anode was used for all studies. In those studies, GDEs were prepared and hot-pressed under identical conditions as those described here (see section 3.2.1) however no mass-transport limitations were observed. This apparent discrepancy can be explained by the lower fuel cell performance due to the increased electrode-to-electrode distance (greater ohmic losses). As shown in Figure 3.6, the maximum current densities observed in the previous alkaline

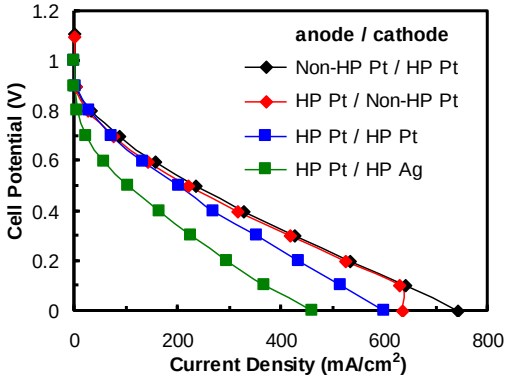

Figure 3.6. Polarization curves for alkaline microfluidic H_2/O_2 fuel cell operated with hot-pressed (HP) and non-hot-pressed (Non-HP) Pt/C- and Ag/C-based GDEs. Present work (diamonds) and previous work (squares) [18]. Studies were performed at room temperature with 50 sccm H_2/O_2 flow rates, and 3 M KOH at 0.3 mL/min.

microfluidic fuel cell, operated with either the hot-pressed Pt/C- or Ag-based cathodes, were not great enough to cause mass transport limitations.

3.3.4 Effects of KOH Concentration on Electrode Performance

As shown in Figure 3.7, fuel cell performance was then investigated as a function of electrolyte concentration (1, 3, 5, 7, and 9 M KOH). Determining the optimum KOH concentration in a liquid electrolyte-based AFC involves consideration of the tradeoffs between kinetics, conductivity, and viscosity, which all change as a function of concentration. Figure 3.7a shows the polarization and power density curves for a microfluidic fuel cell operated with KOH concentrations of 1 to 9 M. The fuel cell generated peak power densities of 83.6, 111.6, 110.4, 95.4 and 76 mW/cm^2 for 1, 3, 5, 7, and 9 M KOH, respectively. As previously discussed

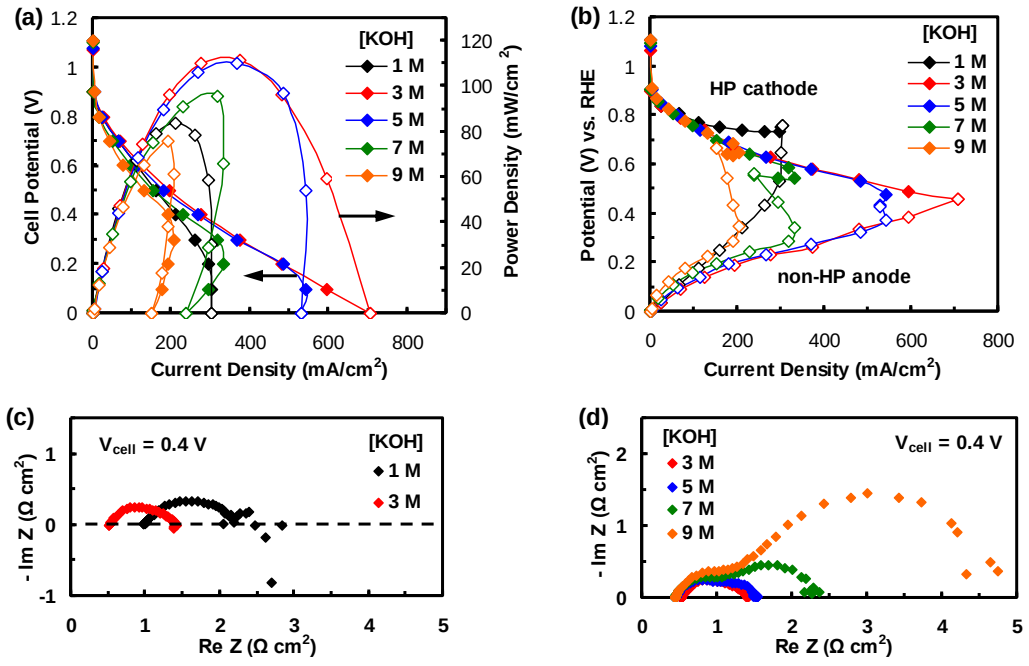

Figure 3.7. **(a)** Polarization and power density curves of alkaline microfluidic H_2/O_2 fuel cell as a function of KOH concentration; **(b)** corresponding HP cathode and non-HP anode polarization curves. EIS spectra of an alkaline microfluidic H_2/O_2 fuel cell operated with **(c)** 1 and 3 M KOH and **(d)** 3, 5, 7, and 9 M KOH. Fuel cell potential held at 0.4 V where peak power density is observed. Studies were performed at room temperature with 50 sccm H_2/O_2 flow rates, and 0.3 mL/min electrolyte flow.

in section 3.3.2, at 1 M KOH, fuel cell performance is limited by anode performance due to lower hydroxyl ion concentrations. Consequently, at low KOH concentrations, the anode performance is limited by the availability of hydroxyl ions. Optimal performance, in terms of peak power density, is observed at 3 and 5 M KOH. However, as concentration increases above 3 M KOH, cell performance lowers despite the increase in electrolyte conductivity, especially at low cell potentials (high current densities). Individual electrode polarization curves reveal several processes lead to the reduced performance at higher concentrations (Figure 3.7b). At higher KOH concentrations, reduced anode and cathode performances are observed due to increased solution viscosity which hampers transport processes [34]. This effect is especially pronounced at higher current densities where anode performance is limiting due to mass transport losses. Increased solution viscosity hampers the removal of formed water from the anode catalyst layer causing electrode flooding. In addition, at high current densities, high counter-ion concentrations may lead to anode shielding effects which could hamper fuel cell performance. Increasing kinetic limitations are observed at increased KOH concentrations due to competitive absorption of hydroxyl ions onto the electrode surface. Alcaide *et al.* observed similar competitive hydroxyl absorption effects at low current densities when studying alkaline hydrogen oxidation on single Pt-based GDEs at KOH $\geq$ 6 M within a 3-electrode electrochemical cell [31]. Similar performance trends were observed with fuel cells operated with varying NaOH concentrations (again, 1 to 9 M).

The effects of KOH concentrations on microfluidic fuel cell performance were further characterized via electrochemical impedance spectroscopy (EIS). EIS studies can be used to decouple the transport and electrochemical phenomena that govern the overall cell performance [35]. Previously, we have employed impedance analysis to investigate the performance of Ag/C

cathodes, in a similar microfluidic configuration, as a function of KOH concentration (1, 3, and 5 M KOH) [18]. Figures 3.7c and 3.7d shows the comparative EIS spectra for the microfluidic H_2/O_2 fuel cell operated at 1, 3, 5, 7, and 9 M KOH. The high frequency intercept of the real Z-axis (x-axis) corresponds to the internal cell resistance (R_{cell}) which decreases with increasing electrolyte concentration, primarily due to reducing solution resistances, until a minimum value is reached at 7 M KOH. At 9 M KOH, solvation of the potassium ions reduces the number of free water molecules in solution, decreasing electrolyte conductivity [36]. The medium-frequency semicircular feature describes the anode and cathode reactions as two overlapping R_{ct}-C_{cpe} parallel circuits with different time constants. The diameter of this feature represents the charge-transfer resistance (R_{ct}) associated with the Faradiac processes on the electrodes. Increasing KOH concentration from 1 to 3 M KOH reduces R_{ct} as the increasing hydroxyl ion concentration improves catalyst activity (Figure 3.7c). However, at KOH concentration greater than 3 M, the adverse effects of anode flooding, due to increased solution viscosity, on hydrogen mass transport limitations appear as a low-frequency semicircular feature impinging on the charge-transfer response (Figure 3.7d).

While, optimal performance in this present microfluidic configuration is observed at 3 M KOH, the majority of AFCs with liquid electrolytes, both stationary and circulating, reported peak performance at ~7 to 8 M KOH [1,5,36,37]. However, these reported AFC technologies operate at elevated temperatures, $\geq$ 65°C, which reduces electrolyte viscosity minimizing the adverse effects of flooding

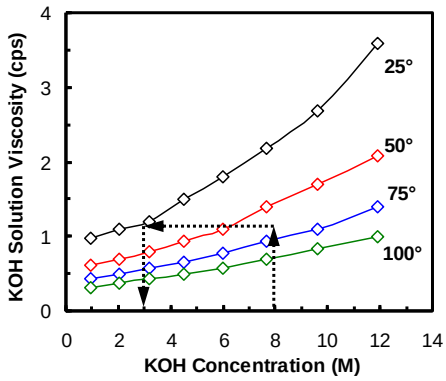

Figure 3.8. Changes in KOH solution viscosity as a function of concentration and temperature. Data was obtained at the following source [33].

observed in the present room temperature studies. In fact, as shown in Figure 3.8, the solution viscosity of 8 M KOH at 65°C is near-identical to that of 3 M KOH at room temperature [34]. Thus, for a room-temperature AFC with a liquid electrolyte, 3 M KOH appears to be the optimal electrolyte concentration. Note that further system-level studies to account for parasitic pumping losses and temperature effects are required to determine the feasibility of such room-temperature systems. Some preliminary work has been performed by Naughton *et al.* who employ a similar alkaline microfluidic fuel cell which is designed to more closely resemble an actual fuel cell-based power source (*i.e.*, air-breathing Ag-based cathode, low H_2 flow rate) [38].

3.3.5 Effects of Electrode-to-Electrode Distance on Electrode Performance

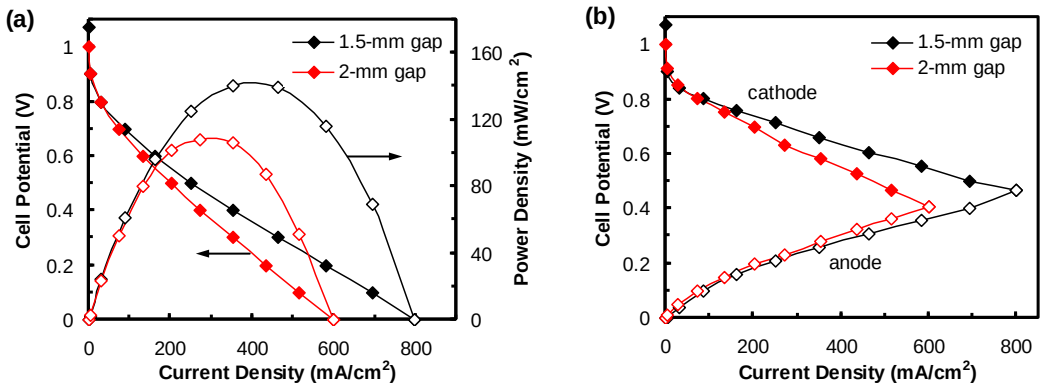

Figure 3.9. The two alkaline microfluidic H_2/O_2 fuel cell configurations studied are: 1.5-mm gap, non-HP anode / HP cathode (black) and 2-mm gap, HP anode / HP cathode (red) [18]. **(a)** Polarization and power density curves for each cell. **(b)** Corresponding electrode polarization curves. Studies were performed at room temperature with 50 sccm H_2/O_2 flow rates, and 3 M KOH at 0.3 mL/min.

In earlier work, Brushett *et al.* characterized the performance of Pt/C- and Ag/C-based cathodes using an identical alkaline microfluidic H_2/O_2 fuel cell with 2-mm electrode-to-electrode distance [18]. In those studies, GDEs were prepared and hot-pressed under identical conditions as those described here (see section 3.2.1). Optimal cell performance was observed at 3 M KOH using Pt/C-based electrodes. These results are compared to the present results obtained in alkaline microfluidic H_2/O_2 fuel cell using a non-HP and a HP cathode and with a

1.5-mm electrode-to-electrode distance (Figure 3.9). Figure 3.9a shows the polarization and power density curves of two fuel cell configurations, and indicates that the present configuration (1.5-mm gap) outperforms the previous configuration (2-mm gap) due to reduced cell resistance (ohmic losses). The corresponding individual electrode polarization curves indicate that this performance enhancement is due to a significant improvement in cathode performance. While that the linear stream velocities in the channels are different, *qualitative* comparisons are possible as both configurations show minimal sensitivity to variations in flow rates at 0.3 mL/min [18]. Furthermore, the slight improvement in anode performance indicates transport processes are optimized (flowing 3 M KOH). Note that the performance of 2-mm gap fuel cell performance does not reach the high current densities where anode flooding is observed (see Figure 3.6). These results indicate that, in the absence of anodic transport limitations, reducing cell resistance leads to improved cathode performance. This suggests that cathode performance is entirely independent of ohmic losses (*e.g.,* high electrolyte concentration) at high current densities, but appears so due to overriding anode performance limitations. Further analyses are required.

3.3.6 Utility of a Microfluidic Fuel Cell for Studying Carbonate Formation

Independent control of electrolyte composition provides a means by which contaminant species can be introduced into the alkaline microfluidic H_2/O_2 fuel cell. This unique feature of the microfluidic analytical platform enables the systematic analysis of the impact of contaminant species on individual electrode performance characteristics within an operating fuel cell. These studies enable the rapid determination of critical contaminant concentrations and exposure times as well as identify optimal catalyst materials and operating protocols. Developing a detailed understanding of the impact and nature of “real-world” impurities on fuel cell systems is a

critical step towards meeting the performance and durability benchmarks established by US, Japanese, and European Union governments [14].

The effects of carbonate formation are of particular importance to the viability of AFC technologies. Carbonate formation (CO_3^{2-} / HCO_3^-) occurs when the hydroxyl ions (OH^-) present in the electrolyte react with carbon dioxide (CO_2) mainly from either organic fuel oxidation, or the environment in which the system operates (*e.g.,* tailpipe emissions from automobiles). The effects of carbonate formation are two-fold. First, in the presence of mobile cations (*i.e.,* liquid electrolytes), carbonate salts can precipitate within the electrodes, where they damage the microporous structure and block electrocatalytic sites, which reduces AFC performance. Second, carbonate formation reduces the hydroxyl ion concentration in the electrolyte, thus gradually reducing both electrode kinetics and electrolyte conductivity. Alkaline anion-exchange membrane (AAEM) - based fuel cells are less susceptible to carbonate poisoning, than liquid electrolyte-based fuel cells, because no mobile cations exist *within the membrane* enabling less stringent operating conditions (*e.g.,* air-breathing cathodes) [7,10]. However, while carbonate ions cannot precipitate in AAEMs, their presence continues to cause adverse effects on both electrode kinetics and membranes conductivity (*e.g.,* pH gradients). Also, carbonate precipitation is still possible in the presence of metal ions that can originate from the electrode structure or the reactant streams [14]. In sum, understanding and mitigating the effects of these carbonate ions is critical for designing robust high-performance membrane-electrode assemblies (MEAs) for AFCs. An alkaline microfluidic H_2/O_2 fuel cell is an excellent analytical platform for the detailed investigation of these key parameters.

Flowing electrolyte-based AFCs are more carbonate tolerant than stagnant electrolyte-based AFCs because carbonate precipitation is dependent on saturation of the total electrolyte volume

rather than the local electrolyte composition [6]. Thus, like in AAEM-based fuel cells, only carbonate ions impact the short-term performance of the flowing electrolyte-based AFCs. Therefore, introducing carbonate species into the electrolyte stream enables the analysis of carbonate ions without the coupled effect of carbonate precipitation. To verify that the dynamic electrolyte could remove and/or prevent carbonate precipitation, two proof-of-concept studies were performed where carbonate formation was triggered by gaseous CO_2 poisoning.

In the first study, the ability of the flowing electrolyte stream to remove previously-formed carbonate species was investigated (Figure 3.10). In these studies, neat CO_2 was introduced on the anode side of a microfluidic H_2/O_2 fuel cell with a stationary 3 M KOH electrolyte. First, the cell performance is analyzed prior to CO_2 exposure to determine a baseline. Second, with the

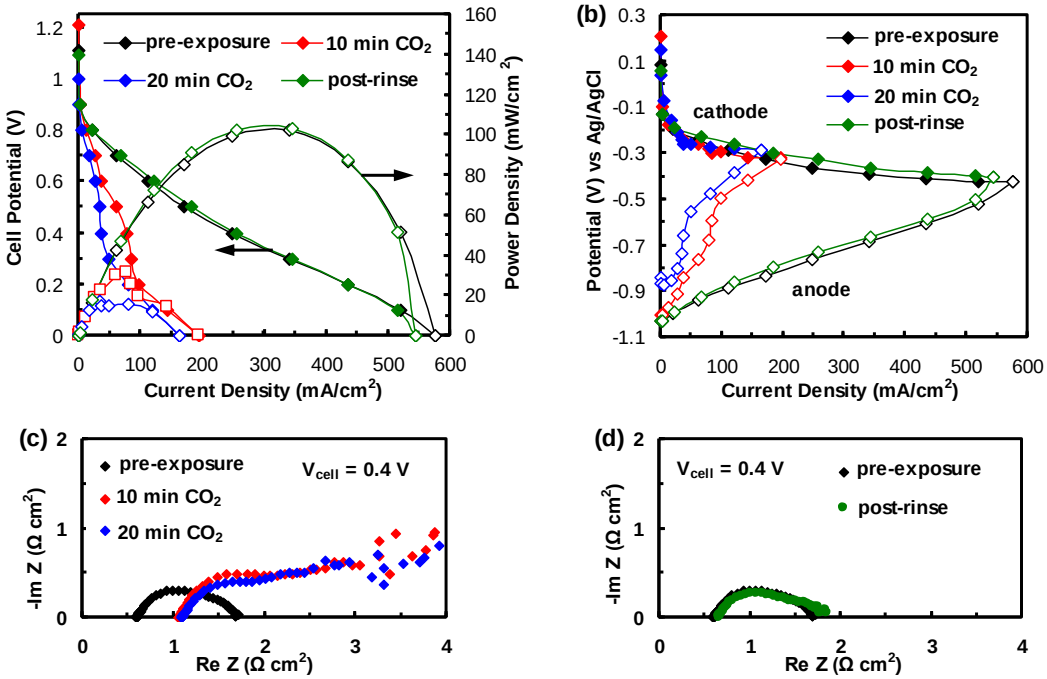

Figure 3.10. Proof-of-principle carbonate formation studies in an alkaline microfluidic H_2/O_2 fuel cell with a stagnant electrolyte. **(a)** Polarization and power density curves of the alkaline microfluidic H_2/O_2 fuel cell as a function of CO_2 poisoning; **(b)** corresponding anode and cathode polarization curves. EIS spectra of an alkaline microfluidic H_2/O_2 fuel cell as a function of **(c)** CO_2 poisoning and **(d)** recovery. Fuel cell potential held at 0.4 V where peak power density is observed. Studies were performed at room temperature with 50 sccm H_2/O_2 flow rates and 3 M KOH at 0.0 and 0.3 mL/min.

fuel cell off but not disassembled, pure CO_2 (15 sccm) flows over the anode for 10 min while N_2 (15 sccm) flows over the cathode. After the exposure, the microfluidic H_2/O_2 fuel cell is tested to determine performance shifts. Third, a second 10 min CO_2 exposure performed with the fuel cell off but not disassembled. After this second exposure, cell performance is again tested. Fourth, a 10 min KOH rinse is performed by flowing electrolyte, at 0.3 mL/min, through the microfluidic chamber. After this rinse, cell performance is tested, with a stationary electrolyte, to determine the effect of the convecting stream.

Figure 3.10a shows the polarization and power density curves of the microfluidic fuel cell, operating with a stationary 3 M KOH electrolyte, during this protocol. Exposure to CO_2 leads to significant performance losses as peak power density decreases from 102.3 to 31.2 mW/cm^2 after the first exposure (10 min total exposure) and then drops to 16 mW/cm^2 after the second exposure (20 min total exposure). However, after a KOH rinse, full peak power density of 103.2 mW/cm^2 is regained. In Figure 3.9b, individual electrode polarization curves indicate that the carbonate species impact the anode performance while the cathode performance appears unaffected by the exposure. After the KOH rinse, anode performance is fully restored. The slight reduction in the maximum current density observed in the recovery data can be attributed to the few remaining precipitants that would most likely to be flushed away by a longer KOH rinse.

Impedance studies are also performed to characterize the effects of CO_2 poisoning on the microfluidic fuel cell. As shown in Figure 3.10c, exposure to CO_2 leads to increased R_{cell} which can be attributed to an increase electrolyte solution resistance as carbonate ions replacing hydroxyl ions. The shape of the semicircular Nyquist plots also varies after exposure to CO_2. The Nyquist features shift from a surface reaction-limited process, as shown by the "closed"

semicircular feature, (pre-exposure) to a transport limited process (post-exposure), as shown by the "open" mass transport slope. This indicates that increased carbonate concentrations hinder hydroxyl ion transport to the catalyst sites. Furthermore, if any carbonate species have precipitated from the stagnant electrolyte, they would likely impact these medium and low frequency features by blocking electrochemical reactions on and transport to the anode catalyst sites. As shown in Figure 3.10d, after a KOH rinse a near-complete performance recovery in observed. Thus, the dynamic electrolyte stream appears to be an effective means of removing formed carbonates (both ions and precipitants) from the microfluidic AFC.

In the second study, the ability of the flowing electrolyte stream to prevent carbonate precipitation was investigated (Figure 3.11). In these studies, neat CO_2 was introduced on the anode side of a microfluidic H_2/O_2 fuel cell with a flowing 3 M KOH electrolyte. *During all experiments, the constant electrolyte flow rate of 0.3 mL/min is maintained.* First, the cell performance is analyzed prior to CO_2 exposure to determine a baseline. Second, with the fuel cell off but not disassembled, pure CO_2 (15 sccm) flows over the anode for 10 min while N_2 (15 sccm) flow over the cathode. After the exposure, the microfluidic H_2/O_2 fuel cell is tested to

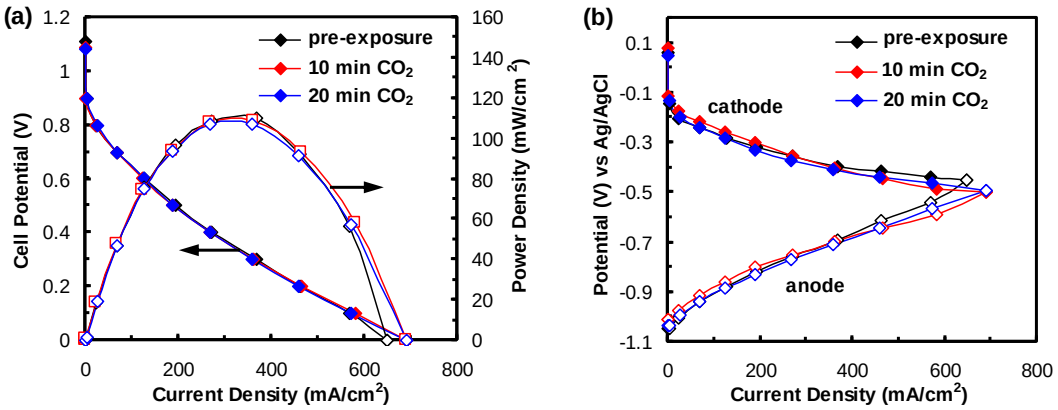

Figure 3.11. Proof-of-principle carbonate formation studies in an alkaline microfluidic H_2/O_2 fuel cell with a dynamic electrolyte. **(a)** Polarization and power density curves of the alkaline microfluidic H_2/O_2 fuel cell as a function of CO_2 exposure; **(b)** corresponding anode and cathode polarization curves. Studies were performed at room temperature with 50 sccm H_2/O_2 flow rates and 3 M KOH at 0.3 mL/min.

determine performance shifts. Third, a second 10 min CO_2 exposure performed with the fuel cell off but not disassembled. After this second exposure, cell performance is again tested.

Figure 3.11a shows the polarization and power density curves of the microfluidic fuel cell, operating with a 3 M KOH electrolyte flowing at 0.3 mL/min, during this protocol. With a dynamic electrolyte, fuel cell performance is unaffected by exposure to CO_2 as any carbonates formed at the three-phase interface are immediately removed. The individual electrode polarization curves confirm that both anode and cathode performance are unaffected by the exposure (Figure 3.11b).

These two studies show that: (*i*) prolonged CO_2 exposure leads to carbonate formation in the microfluidic AFC, and (*ii*) a dynamic electrolyte stream removes any formed carbonates for the electrode-electrolyte interface. This means that the dynamic electrolyte effectively decouples the two-fold effect of carbonate formation by preventing carbonate precipitation onto the electrode surface. Thus, the impact of soluble carbonate ions on individual electrode and overall fuel cell performance can be isolated and observed. Consequently, this microfluidic configuration can be used to investigate the impact of carbonates on electrode performances for both liquid electrolyte- and AAEM-based fuel cells.

3.3.7 Effects of Carbonates on Electrode Performance

Using this microfluidic platform, carbonate poisoning in an AFC can be simulated by systematically varying the composition of the electrolyte stream. The effects of increasing carbonate poisoning on individual electrode and overall cell performance are shown in Figure 3.12 by

Table 3.1. Tested KOH and K_2CO_3 concentration ratios for studies shown in Figure 3.12.

Legend	[KOH] : [K_2CO_3] (M : M)
A / A-rec	3 : 0
B	2 : 0.5
C	1 : 1
D	0 : 1.5

stoichiometrically replacing KOH with K_2CO_3 in increments of 0.5 M KOH, starting with 3 M KOH (Table 3.1). Figure 3.12a shows polarization and power density curves for the microfluidic H_2/O_2 fuel cell operating with a flowing electrolyte of varying composition. Note that the individual electrode curves shown in Figure 3.12b are qualitatively similar to those observed in Figure 3.10b indicating the effectiveness of this analytical method in simulating carbonate poisoning.

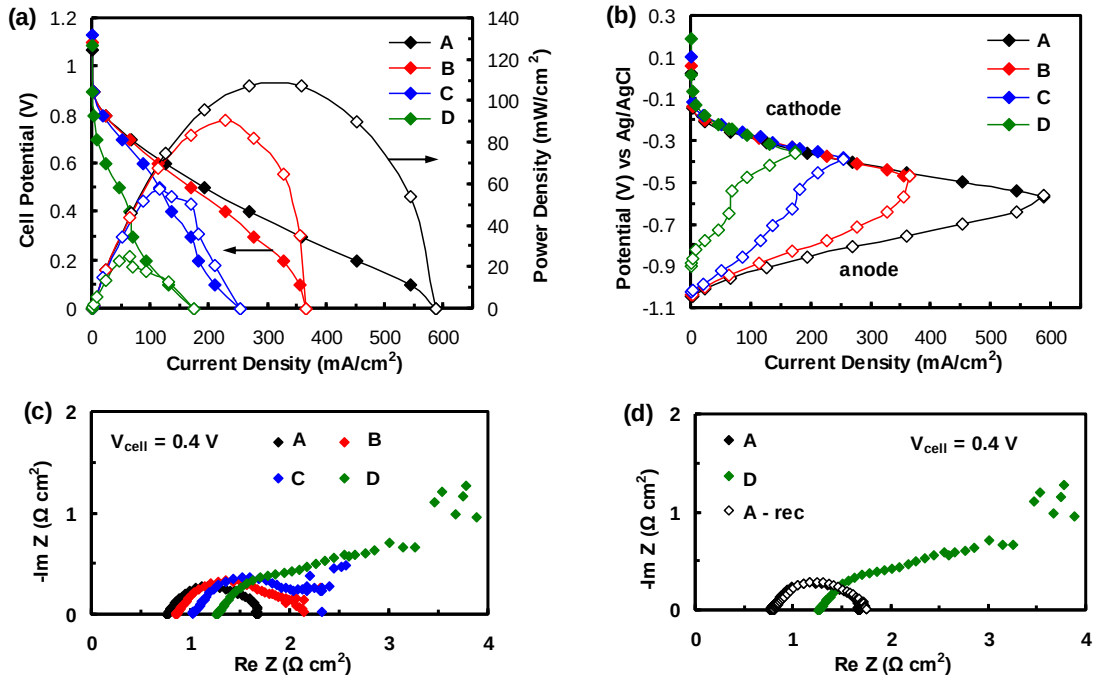

Figure 3.12. **(a)** Polarization and power density curves of alkaline microfluidic H_2/O_2 fuel cell as a function of carbonate content in the electrolyte stream; **(b)** corresponding anode and cathode polarization curves. EIS spectra of the alkaline microfluidic H_2/O_2 fuel cell show **(c)** the effects of carbonate content and **(d)** the process reversibility. Studies were performed at room temperature with 50 sccm H_2/O_2 flow rates and 3 M KOH at 0.3 mL/min.

Carbonate poisoning in the electrolyte significantly lowers fuel cell performance due to significant limitations in anodic processes (Figure 3.12b). As the carbonate ions are negatively charged species they migrate to the anode surface increasing the local carbonate concentrations, blocking the electrode surface and lowering pH [39]. These observations are in good agreement with recent AAEM-based fuel cell literature [9,10,39]. Notably, Yanagi *et al.* demonstrated a

CO_2 self-purging mechanism at the anode through power generation where carbonate species shifts back to hydroxyl ions and CO_2 which was measured by a mass spectrometer at the fuel cell anode outlet [10]. In the case, the microfluidic fuel cell operated with the carbonate-only solution (D in Figure 3.12), the open circuit anode potential shifts upwards as compared to the other solution (A-C) due to the pH shift. In this configuration, at open circuit potential, hydroxyl ions must be shifting carbonate ions back to hydroxyl ions and CO_2. This anode reaction is likely similar to the proposed anode reaction in a carbonate-based AAEM fuel cell developed by the Kohl group [40,41]. On the cathode side, the generation of negatively-charged hydroxyl ions not only prevents carbonates from travelling to that surface but also maintains a high local pH. Consequently, the cathode performance in Figure 3.11b, like in Figure 3.9b, appears to be independent of carbonate concentration. These fuel cell results are supported by recent observations in a 3-electrode electrochemical cell by Vega and Mustain [30].

Figures 3.12c and 3.12d show impedance spectra of the microfluidic H_2/O_2 fuel cell operated with varying alkaline electrolyte compositions (KOH : K_2CO_3 ratios). With increasing carbonate concentrations, R_{cell} increases indicating reduced electrolyte conductivity, which can expected due to the lowered hydroxyl ion concentrations. The shape of the semicircular Nyquist features also varies with increasing carbonate concentrations. The shift from a surface reaction-limited process, as indicated by "closed" semicircular feature, shown in curve A, to a transport limited process, as indicated by "open" mass transfer slope, shown in curve D. This can be attributed to increased carbonate concentrations in close proximity to the anodic catalytic sites which hinder hydroxyl ion transport. Furthermore, impedance analysis shows that these effects are reversible as changing the dynamic electrolyte composition from pure KOH (curves A) to pure K_2CO_3

(curve D), and back to pure KOH (curve A-rec) and (curve D) solutions, again indicating that no carbonate species precipitate (Figure 3.12d).

These initial carbonate studies highlight the greater utility of the microfluidic fuel cell as an analytical platform for measuring contaminant effects on individual electrode and overall cell performance. Building on these proof-of-concept demonstrations, Naughton *et al.* performed extensive studies of the critical parameters (*i.e.,* concentrations, exposure time) that govern the impact of carbonate species on air-breathing AFC performance and lifetime [38]. Indeed, beyond carbonates, similar techniques may be employed to rapidly characterize the effects of a broad range of contaminants (*e.g.*, unreacted organic fuels, by-products of incomplete fuel reformation, airborne pollutants) on the individual electrode and overall cell performance of both alkaline and acidic fuel cell systems [14].

3.3.8 Electrode Durability in Alkaline Microfluidic Fuel Cell

For all studies, the *same* two electrodes (one non-HP and one HP) were used as the anode and cathode. However, fuel cell performance steadily decreases over the course of experimentation. For example, the cell performance shown in Figure 3.5 is greater than that shown in Figure 12 though identical operating conditions are used in both trials. Note that presented results remain valid as the comparative studies were performed on the same day. Over the course of alkaline microfluidic fuel cell testing, performance decay was observed (Table 3.2).

Table 3.2. Fuel cell performance degradation as function of open circuit potential, peak power density and maximum current density. Maximum current density is defined as the current density at V_{cell} = 0 V. Studies were performed at room temperature with 50 sccm H_2/O_2 flow rates and 3 M KOH at 0.3 mL/min.

Fuel Cell Parameter	Fresh	Aged	% decrease
Open Circuit Potential (V)	1.12	1.07	4.5
Peak Power Density (mW/cm^2)	158.3	108	31.8
Maximum Current Density (mA/cm^2)	770	366	52.5

The effects of aging were characterized using the results from fuel cell experiments performed with 3 M KOH electrolyte flowing at 0.3 mL/min which was determined to be the optimal operating condition. Thus, the first 3 M KOH flow rate study is used as the beginning-of-life (BOL) test. The end-of-life (EOL) test was performed after ~58 days of testing including hot-pressing, electrolyte concentration, and carbonate formation studies. Note that a number of tests were performed after the data reported in the preceding sections.

Over the course of experiments, fuel cell open circuit potential decreased slightly while peak power and maximum current densities decreased significantly. This dramatic reduction in performance at higher current density regimes indicates that increased mass transport losses the primary result of electrode aging. Extended exposure to caustic alkaline environment causes gas diffusion electrode degradation due to peroxide radical formation that destroys the hydrophobic polytetrafluoroethylene (PTFE) within the catalyst and gas diffusion layers [6]. PTFE polymer degradation causes increased electrode hydrophilicity which adversely affects water management and leads to such phenomena as "electrode weeping" where the liquid electrolyte floods the porous diffusion layers of the electrode and severely hinders gaseous reactant transport.

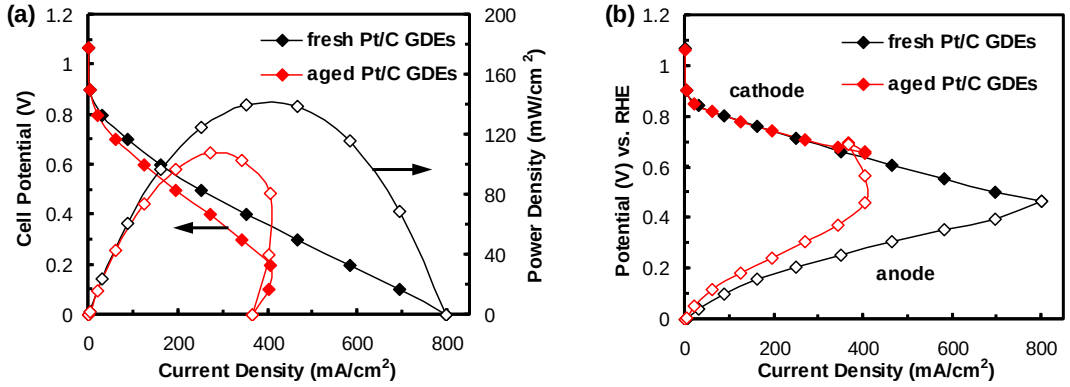

Figure 3.13. **(a)** Polarization and power density curves of alkaline microfluidic H_2/O_2 fuel cell operated with fresh and aged GDEs; **(b)** corresponding anode and cathode polarization curves. Studies were performed at room temperature with 50 sccm H_2/O_2 flow rates and 3 M KOH at 0.3 mL/min.

Figure 3.13 shows the effects of water mismanagement in aged electrodes on fuel cell performance. Figure 3.13a shows polarization and power density curves of an alkaline microfluidic H_2/O_2 fuel cell operated with fresh (*near* BOL) and aged (EOL) GDEs. The cell operated with fresh GDEs significantly outperforms the cell operated with aged GDEs primarily due to improved performance in the higher current densities were efficient water management is critical. Figure 3.13b shows that cell performance is limited by mass transport due to anodic water mismanagement. Moreover, the minimal cathode performance degradation was observed as flooding is less of a concern. Identical performance trends were observed for HP and non-HP GDEs. Microtomographic analyses of effects of prolonged alkaline operation on GDE structure may be found in Chapter 5.

In addition to the losses in GDE hydrophobicity, carbon corrosion is another source of degradation. Oxidation of carbonaceous catalyst supports and gas diffusion layer materials can occur at high potentials ($\geq$ 0.8 V vs. RHE) which can lead to losses in active surface area and catalyst layer delamination [14]. In Figure 3.14, the SEM-EDS micrographs show the effects of aging on the catalyst layer of a *different* Pt/C-based electrode that was used for AFC analysis. In

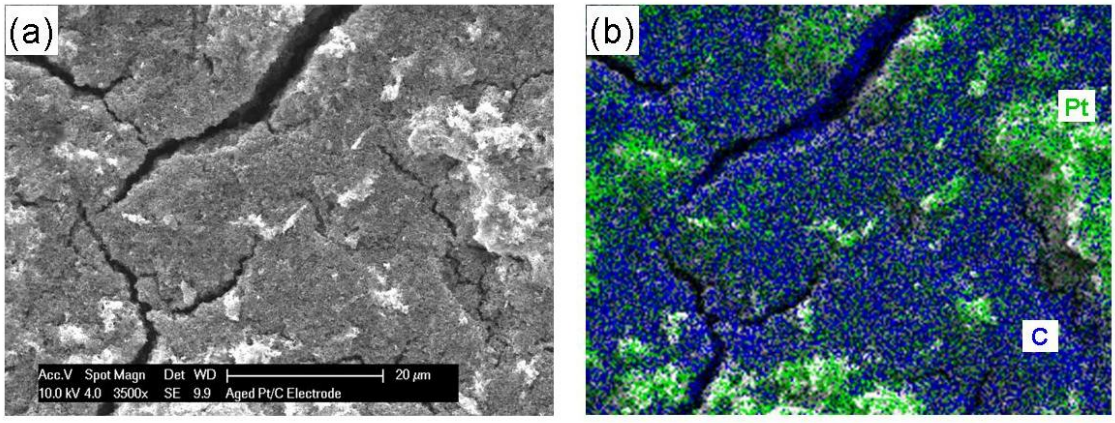

Figure 3.14. (a) SEM micrograph of the Pt/C catalyst layer of an aged electrode. **(b)** Corresponding SEM-EDX sample micrograph with Pt and C species location overlaid in false color.

addition to standard use in polarization curve studies, this electrode was also used for cathodic Tafel slope analyses which consisted of extended chronoamperometric runs at high potentials. The SEM-EDS micrographs indicate that carbon corrosion leads to local concentrations of Pt species which leads to reduce catalyst distribution and consequently lower electrode performance. The formation of these Pt-rich islands was not limited to area shown in the micrograph but occurred across the electrode surface (not shown).

3.4 Conclusions

With renewed interest in AFC systems, a need exists for a detailed understanding and subsequent optimization of electrode performance as a function of preparation methods and operating parameters for the development of robust and cost-effective power sources. A microfluidic H_2/O_2 fuel cell is a convenient and powerful platform for probing the underlying processes that govern the performance of electrodes within a working fuel cell. Detailed analyses of the performance of Pt/C-based electrodes, as a function of preparation procedures and fuel cell operating parameters, indicate that in hydrogen-fueled AFCs, *unlike in acidic PEM-based fuel cells*, transport processes to and from the anode significantly contribute to polarization losses and can limit performance. In fact, an AFC anode is more similar to an acidic fuel cell cathode since both must efficiently remove generated water to maintain performance. Water accumulation at the anode leads to both local electrolyte dilution (hydroxyl depletion layer and electrode flooding. AFC anode water management appears to be strong function of both physical structure and electrolyte viscosity. Thus, aside from the expected activation losses due to slow ORR kinetics, AFC cathodes do not limit performance as severely as acidic fuel cell cathodes. For example, typical electrode issues associated of acidic cathodes, such as mass transport losses due to electrode flooding, do not impact alkaline cathodes as significantly

because water is a reactant in the alkaline ORR. Furthermore, carbonate species, a common contaminant for all AFCs, limits anode performance by reducing local pH and blocking hydroxyl transport to the electrocatalytic sites. The cathode performance is unaffected by the presence of carbonate species as the generation of negatively-charged hydroxyl ions not only prevents carbonates from travelling to that surface but also maintains a high local pH. Also, because efficient water management is needed for optimal performance, anode degradation due to hydrophobicity losses limits long-term performance.

While continued research into improving cathode performance remains critical, these observations suggest that significant efforts must also be focused developing novel anode materials for AFC applications. Electrode materials and structures must be designed that improve water management and limit degradation. Furthermore, Pt-free anode electrocatalysts must be developed that operate efficiently at lower pHs and in the presence of carbonate species.

3.5 References

1. Carrette, L., K.A. Friedrich, and U. Stimming, *Fuel cells: Principles, types, fuels, and applications.* Chemphyschem, 2000. **1**(4): p. 162-193.
2. Dyer, C.K., *Fuel cells for portable applications.* Journal of Power Sources, 2002. **106**: p. 31-34.
3. Jacoby, M., *Analytics for Fuel Cells.* Chemical & Engineering News, 2009. **87**(13): p. 39-41.
4. Spendelow, J.S. and A. Wieckowski, *Electrocatalysis of oxygen reduction and small alcohol oxidation in alkaline media.* Physical Chemistry Chemical Physics, 2007. **9**(21): p. 2654-2675.
5. Gouerec, P., L. Poletto, J. Denizot, E. Sanchez-Cortezon, and J.H. Miners, *The evolution of the performance of alkaline fuel cells with circulating electrolyte.* Journal of Power Sources, 2004. **129**(2): p. 193-204.
6. Cifrain, M. and K.V. Kordesch, *Advances, aging mechanism and lifetime in AFCs with circulating electrolytes.* Journal of Power Sources, 2004: p. 234-242.
7. Varcoe, J.R. and R.C.T. Slade, *Prospects for alkaline anion-exchange membranes in low temperature fuel cells.* Fuel Cells, 2005. **5**(2): p. 187-200.
8. Lu, S.F., J. Pan, A.B. Huang, L. Zhuang, and J.T. Lu, *Alkaline polymer electrolyte fuel cells completely free from noble metal catalysts.* Proceedings of the National Academy of Sciences of the United States of America, 2008. **105**(52): p. 20611-20614.
9. Adams, L.A., S.D. Poynton, C. Tamain, R.C.T. Slade, and J.R. Varcoe, *A carbon dioxide tolerant aqueous-electrolyte-free anion-exchange membrane alkaline fuel cell.* Chemsuschem, 2008. **1**(1-2): p. 79-81.
10. Yanagi, H. and K. Fukuta, *Anion Exchange Membrane and Ionomer for Alkaline Membrane Fuel Cells (AMFCs).* ECS Transactions, 2008. **16**(2): p. 257-262.
11. McLean, G.F., T. Niet, S. Prince-Richard, and N. Djilali, *An assessment of alkaline fuel cell technology.* International Journal of Hydrogen Energy, 2002. **27**(5): p. 507-526.

12. Kordesch, K., J. Gsellmann, M. Cifrain, S. Voss, V. Hacker, R.R. Aronson, C. Fabjan, T. Hejze, and J. Daniel-Ivad, *Intermittent use of a low-cost alkaline fuel cell-hybrid system for electric vehicles.* Journal of Power Sources, 1999. **80**(1-2): p. 190-197.
13. Gülzow, E., *Alkaline Fuel Cells.* Fuel Cells, 2004. **4**(4): p. 251-255.
14. Borup, R., J. Meyers, B. Pivovar, Y.S. Kim, R. Mukundan, N. Garland, D. Myers, M. Wilson, F. Garzon, D. Wood, P. Zelenay, K. More, K. Stroh, T. Zawodzinski, J. Boncella, J.E. McGrath, M. Inaba, K. Miyatake, M. Hori, K. Ota, Z. Ogumi, S. Miyata, A. Nishikata, Z. Siroma, Y. Uchimoto, K. Yasuda, K.I. Kimijima, and N. Iwashita, *Scientific aspects of polymer electrolyte fuel cell durability and degradation.* Chemical Reviews, 2007. **107**(10): p. 3904-3951.
15. Ramasamy, R.P., E.C. Kumbur, M.M. Mench, W. Liu, D. Moore, and M. Murthy, *Investigation of macro- and micro-porous layer interaction in polymer electrolyte fuel cells.* International Journal of Hydrogen Energy, 2008. **33**(13): p. 3351-3367.
16. Hizir, F.E., S.O. Ural, E.C. Kumbur, and M.M. Mench, *Characterization of interfacial morphology in polymer electrolyte fuel cells: Micro-porous layer and catalyst layer surfaces.* Journal of Power Sources, 2010. **195**(11): p. 3463-3471.
17. Kucernak, A.R. and E. Toyoda, *Studying the oxygen reduction and hydrogen oxidation reactions under realistic fuel cell conditions.* Electrochemistry Communications, 2008. **10**(11): p. 1728-1731.
18. Brushett, F.R., W.P. Zhou, R.S. Jayashree, and P.J.A. Kenis, *Alkaline Microfluidic Hydrogen-Oxygen Fuel Cell as a Cathode Characterization Platform.* Journal of the Electrochemical Society, 2009. **156**(5): p. B565-B571.
19. Jayashree, R.S., M. Mitchell, D. Natarajan, L.J. Markoski, and P.J.A. Kenis, *Microfluidic Hydrogen Fuel Cell with a Liquid Electrolyte.* Langmuir, 2007. **23**(13): p. 6871-6874.
20. Brushett, F.R., H.T. Duong, J.W.D. Ng, A. Wieckowski, and P.J.A. Kenis, *Investigation of Pt, Pt_3Co and Pt_3Co/Mo cathodes for the Oxygen Reduction Reaction in an Acidic Microfluidic H_2/O_2 Fuel Cell.* Journal of the Electrochemical Society, 2010. **157**(6): p. B837-B845.
21. Choban, E.R., P. Waszczuk, and P.J.A. Kenis, *Characterization of limiting factors in laminar flow-based membraneless microfuel cells.* Electrochemical and Solid State Letters, 2005. **8**(7): p. A348-A352.
22. Ghouse, M., A. Alboeiz, H. Abaoud, and M. Algarni, *Preparation and evaluation of PTFE-bonded porous gas-diffusion carbon electrodes use in phosphoric-acid fuel cell applications.* Int. J. Hydrog. Energy, 1995. **20**(9): p. 727-736.
23. Varcoe, J.R., R.C.T. Slade, G.L. Wright, and Y.L. Chen, *Steady-state dc and impedance investigations of H_2/O_2 alkaline membrane fuel cells with commercial Pt/C, Ag/C, and Au/C cathodes.* Journal of Physical Chemistry B, 2006. **110**(42): p. 21041-21049.
24. Freire, T.J.P. and E.R. Gonzalez, *Effect of membrane characteristics and humidification conditions on the impedance response of polymer electrolyte fuel cells.* Journal of Electroanalytical Chemistry, 2001. **503**(1-2): p. 57-68.
25. Srinivasan, S., *Fuel Cells. From Fundamentals to Applications*. 2006, New York: Springer.
26. Gasteiger, H.A., S.S. Kocha, B. Sompalli, and F.T. Wagner, *Activity benchmarks and requirements for Pt, Pt-alloy, and non-Pt oxygen reduction catalysts for PEMFCs.* Applied Catalysis B - Environmental, 2005. **56**(1-2): p. 9-35.
27. Lee, W.K., C.H. Ho, J.W. Van Zee, and M. Murthy, *The effects of compression and gas diffusion layers on the performance of a PEM fuel cell.* Journal of Power Sources, 1999. **84**(1): p. 45-51.
28. Bazylak, A., D. Sinton, Z.S. Liu, and N. Djilali, *Effect of compression on liquid water transport and microstructure of PEMFC gas diffusion layers.* Journal of Power Sources, 2007. **163**(2): p. 784-792.
29. Vega, J.A., C. Chartier, and W.E. Mustain, *Effect of hydroxide and carbonate alkaline media on anion exchange membranes.* Journal of Power Sources, 2010. **195**(21): p. 7176-7180.
30. Vega, J.A. and W.E. Mustain, *Effect of CO2, HCO3- and CO3-2 on oxygen reduction in anion exchange membrane fuel cells.* Electrochimica Acta, 2010. **55**(5): p. 1638-1644.
31. Alcaide, F., E. Brillas, and P.L. Cabot, *Hydrogen oxidation reaction in a Pt-catalyzed gas diffusion electrode in alkaline medium.* Journal of the Electrochemical Society, 2005. **152**(10): p. E319-E327.

32. Schmidt, T.J., P.N. Ross, and N.M. Markovic, *Temperature dependent surface electrochemistry on Pt single crystals in alkaline electrolytes Part 2. The hydrogen evolution/oxidation reaction*. Journal of Electroanalytical Chemistry, 2002. **524**(SI): p. 252-260.
33. Zeng, R., S.D. Poynton, J.P. Kizewski, R.C.T. Slade, and J.R. Varcoe, *A novel reference electrode for application in alkaline polymer electrolyte membrane fuel cells.* Electrochemistry Communications, 2010. **12**(6): p. 823-825.
34. Products, O.C.A. *http://koh.olinchloralkali.com/TechnicalInformation/default.aspx*. 2009 [cited 2009 September 25].
35. Bard, A.J. and L.R. Faulkner, *Electrochemical Methods: fundamentals and applications*. 2nd ed. 2001, Hoboken: John Wiley & Sons, Inc. 368-388.
36. Lin, B.Y.S., D.W. Kirk, and S.J. Thorpe, *Performance of alkaline fuel cells: A possible future energy system?* Journal of Power Sources, 2006. **161**(1): p. 474-483.
37. Burchardt, T., P. Gouerec, E. Sanchez-Cortezon, Z. Karichev, and J.H. Miners, *Alkaline fuel cells: contemporary advancement and limitations.* Fuel, 2002. **81**: p. 2151-2155.
38. Naughton, M.S., F.R. Brushett, and P.J.A. Kenis, *Carbonate resilience of flowing electrolyte-based alkaline fuel cells.* Journal of Power Sources, 2010: p. accepted.
39. Wang, Y., L. Li, L. Hu, L. Zhuang, J.T. Lu, and B.Q. Xu, *A feasibility analysis for alkaline membrane direct methanol fuel cell: thermodynamic disadvantages versus kinetic advantages.* Electrochemistry Communications, 2003. **5**(8): p. 662-666.
40. Lang, C.M., K. Kim, and P.A. Kohl, *High-energy density, room-temperature carbonate fuel cell.* Electrochemical and Solid State Letters, 2006. **9**(12): p. A545-A548.
41. Unlu, M., J. Zhou, and P.A. Kohl, *Anion Exchange Membrane Fuel Cells: Experimental Comparison of Hydroxide and Carbonate Conductive Ions.* Electrochemical and Solid State Letters, 2009. **12**(3): p. B27-B30.

Chapter 4

A Carbon-Supported Copper Complex of 3,5-Diamino-1,2,4-triazole as a Cathode Catalyst*

4.1 Introduction

Fuel cell-based systems hold promise as alternative power sources for a range of applications due to their high efficiency, high energy density, and low emissions [1]. For low-temperature applications, acidic polymer electrolyte membrane-based fuel cells (PEMFCs) are considered most promising [2]. Widespread market penetration of these PEMFCs has yet to be realized mainly due to high costs (platinum (Pt) catalysts, Nafion membranes), insufficient durability, and system performance limitations as detailed in Chapter 1 [3]. A key challenge is the oxygen reduction reaction (ORR) on the cathode. Sluggish kinetics and high overpotentials associated with the ORR necessitate substantial loadings of expensive precious metal catalysts to achieve adequate performance [4]. Thus, reducing or eliminating Pt content in fuel cell cathodes, without sacrificing performance and durability, is a critical step towards improving the commercial viability of fuel cell technologies.

Alternative Pt-free ORR catalysts include pyrolyzed Fe(Co)/N/C systems [5,6] , ruthenium-based chalcogenides [7] , cobalt-polypyrrole-composites [8] , and enzymes [9] , but none have shown the necessary combination of activity and stability to replace Pt catalysts in acidic fuel cells. Of the catalysts listed above, enzymes, specifically multi-copper (Cu) oxidases (*e.g.*, laccases), are arguably the most intriguing due to their remarkable oxygen reduction activity at potentials approaching 1.2 V versus a reversible hydrogen electrode (RHE) [10-12]. In

* Part of this work has been published: F.R. Brushett, M.S. Thorum, N.S. Lioutas, M.S. Naughton, C. Tornow, H.R. Jhong, A.A. Gewirth, P.J.A Kenis, "A Carbon-Supported Copper Complex of 3,5-Diamino-1,2,4-triazole as a Cathode Catalyst for Alkaline Fuel Cell Applications", *Journal of the American Chemical Society*, 132, 12185-12187, 2010.

comparison, the onset of oxygen reduction on Pt catalysts occurs at approximately 1.0 V which is well below the reversible ORR potential of 1.23 V (vs. RHE) [1]. Unfortunately, despite their high efficiency, significant barriers hinder the practical application of enzyme-modified cathodes in fuel cells including high cost, limited durability, limited pH ranges (4-7), and low power densities due to low surface coverage (bulky protein structure) [13]. To overcome of these limitations without sacrificing the high activity, a number of biomimetic Cu complexes have been explored [14-22]. Synthetic multi-Cu^{II} complexes coordinated with bridging azole-type ligands appear to be the most promising choice as a fuel cell cathode catalyst [22]. Thorum *et al.* developed a novel method of directly preparing insoluble Cu complexes on carbon black supports and showed that a carbon-supported Cu complex of 3,5-diamino-1,2,4-triazole (Cu-tri/C) exhibits moderate ORR activity under acidic conditions, but high activity under alkaline conditions [22]. Indeed, ORR kinetics are often more facile and electrocatalytic materials are more stable under alkaline conditions as compared to acidic conditions [23]. For example, recent electrochemical studies by Meng *et al.* showed that Fe/N/C catalysts exhibited enhanced activity and stability under alkaline conditions (pH = 13) compared to acidic conditions (pH = 1) [24].

Building on the promising ORR performance of Cu-tri/C in a 3-electrode cell especially under alkaline conditions [22], the performance and durability of the Cu-tri/C catalyst, when integrated in an actual electrode, are characterized for fuel cell applications. Electrode performance is investigated using a pH-flexible microfluidic H_2/O_2 fuel cell as an analytical platform (see Figure 2.4) [25-27]. Instead of a polymeric membrane between the two electrodes, this cell has a flowing electrolyte stream which enables independent control over electrolyte parameters (*i.e.*, composition), and allows for *in-situ* analyses of individual electrode performance via a reference electrode. Thus, this platform is convenient for studying the

performance and durability of novel catalysts integrated in gas diffusion electrodes (GDEs), closely resembling the way in which they will be employed in fuel cells [27]. The Cu-tri/C-based cathode performance is compared to other commonly employed cathode catalyst materials for acidic and alkaline fuel cell applications.

4.2 Experimental

4.2.1 Synthesis of Cu-tri/C

The Cu-tri/C was synthesized in the Gewirth group in the Chemistry Department at the University of Illinois [22]. Vulcan XC-72 (1.00 g, Cabot), $Cu(SO_4)_2 \cdot 5H_2O$ (0.200 g, 0.801 mmol, Aldrich, 99.995%), and water (20 mL, Milli-Q UV Plus, 18.2 MΩ) were combined and sonicated to form a viscous suspension. A solution of 3,5-diamino-1,2,4-triazole (0.159 g, 1.60 mmol, Aldrich, 98%) in water (10 mL, Milli-Q UV Plus, 18.2 MΩ) was then added dropwise with stirring. After the mixture was stirred for 18 hr, the solids were collected by suction filtration, dried *in-vacuo* for 3 hr at 90°C, and pulverized with a mortar and pestle. Elemental analysis (wt%) found: C 85.2, H 0.14, N 5.36, Cu 3.76. The Cu-tri content on carbon supports was varied by reducing the amount of Vulcan XC-72 particles in the solution.

4.2.2 Gas Diffusion Electrode Preparation

Commercial Pt/C (50 wt% Pt, E-Tek) and Cu-tri/C (3.76 wt% Cu, *in-house* synthesized), were investigated as cathode catalyst materials. Pt/C was used for the anode catalyst material. The Pt/C electrodes had total loadings of 2 mg/cm^2, resulting in a metal loading of 1 mg Pt/cm^2. The Cu-tri/C electrodes had total loadings ranging from 1 to 4 mg/cm^2. For all studies, Nafion (5 wt% solution, Solution Technology) was also added as a binder at a 30:1 ratio of catalyst to binder [25]. Catalyst inks were prepared by mixing the desired amounts of catalyst and binder

with 200 μL of Millipore water (18.2 MΩ) and 200 μL of isopropyl alcohol which function as carrier solvents. The inks were sonicated (Branson 3510) for at least 1 hr and then were hand-painted onto teflonized carbon-side of ELAT carbon cloth gas diffusion layers (BASF) over a geometric area of 4 cm^2 (4 (L) x 1 (W) cm^2).

4.2.3 Fuel Cell Assembly and Testing

Two gas diffusion electrodes (GDEs), an anode and a cathode, were placed onto either side of a 0.15-cm thick polymethyl(methylacrylate) (PMMA) sheet with a precision-machined 3.3-cm long and 0.3-cm wide channel, which enables the passage of liquid electrolytes through the fuel cell during experimentation. GDEs were placed facing inward on either side of the channel, such that the catalyst-covered layer interfaces directly with flowing electrolyte. Two 0.1-cm thick graphite plates with access windows (3.8 (L) x 0.7 (W) cm^2) are placed on the outside of the GDEs and served as current collectors. Polycarbonate flow chambers (4 (L) x 1 (W) x 0.2 (H) cm^3) were placed on outside the graphite windows for the introduction of reactant gases. The multilayer assembly was all held together using binder clips. Prior to experimentation, the fuel cell assembly was leak-tested by flowing deionized water through the fluidic chamber for several minutes. In the few cases leaking was observed, typically due to misalignment of the layers, the cell was disassembled and realigned. No leaking was observed during subsequent operation.

Fuel cell experiments were conducted using NOVA Software (EcoChemie) controlled by a potentiostat (Autolab PGSTAT-30, EcoChemie). Oxygen and hydrogen gases (S.J. Smith, laboratory grade) were run through the gas flow chambers at a flow rate of 50 sccm each. The cell was supplied with either 0.5 M sulfuric acid (H_2SO_4, GFS Chemicals) or 1 M potassium hydroxide (KOH, Aldrich). Electrolyte flow rates were held at 0.6 mL/min using a syringe pump (2200 PHD, Harvard Apparatus). Once the gas and liquid streams were introduced, the fuel cell

was held at open circuit potential (OCP) for 5 min to ensure that the cell potential stabilized prior to testing. Fuel cell polarization curves were obtained by steady-state chronoamperometric measurements at different cell potentials using the potentiostat. Potentiostat leads were attached to the anodic and cathodic graphite current collectors via copper alligator clips. The working electrode lead was attached to the anode while the reference and counter electrode leads were combined and attached to the cathode. The potentiostat was used to generate an applied potential, and a multimeter (15 XP Meterman, 87 III Fluke, or 179 Fluke), with its leads attached to the anodic and cathodic graphite current collectors, was used to determine the actual cell potential. This configuration enables the elimination of any resistive contributions due to connection resistances between the alligator clips of the leads and the graphite current collector plates. The geometric surface area used to calculate current and power density is 1 cm^2 (based on the electrolyte channel length and width). After exiting the fuel cell, the electrolyte stream collects in a beaker with a reference electrode (Ag/AgCl in saturated NaCl, BASi). The anode and cathode polarization losses are independently characterized using two multimeters, functioning in voltmeter mode, and attached to the reference electrode and each of the graphite plate current collectors. No potential drop is observed along the plastic tubing (Cole Parmer, 1.57 mm ID) connecting the fuel cell and the reference electrode [28]. The open circuit potential of the Pt/C anode, exposed to 50 sccm H_2, was used to calibrate the reference electrode to the RHE scale. All studies are performed at room temperature.

4.2.4 Accelerated Cathode Durability Studies

All cathode durability studies were performed in a single compartment 3-electrode electrochemical cell using O_2-saturated 1 M KOH (Fisher) electrolyte with an O_2 atmosphere above the solution. The GDE used as the working electrode was immersed in the electrolyte to a

sufficient depth to wet the entire applied catalyst layer. A graphite rod served as a counter electrode and the reference electrode was a "no leak" Ag/AgCl electrode (Cypress Systems). The working electrode was replaced with Pt at the end of an aging experiment, the cell was saturated with H_2, and the open circuit potential was recorded and used to calibrate the reference electrode to the RHE scale.

4.3 Results and Discussion

4.3.1 Cu-tri/C-based Cathode Performance in Acidic and Alkaline Conditions

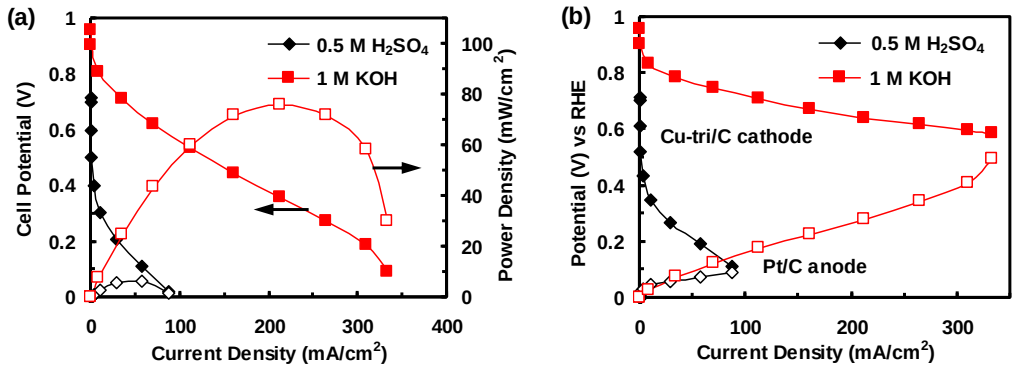

Figure 4.1. **(a)** Polarization and power density curves for microfluidic H_2/O_2 fuel cell operated with a Cu-tri/C cathode under 1 M KOH and 0.5 M H_2SO_4. **(b)** Corresponding individual anode and cathode polarization curves. Studies were performed at room temperature using a 4 mg Cu-tri/C/cm^2 cathode and 2 mg Pt/C/cm^2 anode, with 0.6 mL/min electrolyte flow and 50 sccm H_2/O_2 gas flow.

The pH sensitivity of the Cu-tri/C-based cathode (4 mg/cm^2) performance is investigated using a microfluidic H_2/O_2 fuel cell with a flowing electrolyte of 0.5 M H_2SO_4 (pH~0.3) and 1 M KOH (pH~14). Figure 4.1a shows representative polarization and power density curves of a fuel cell operated with a Cu-tri/C-based cathode and a Pt/C-based anode under acidic and alkaline conditions. Cell performance is significantly lower under acidic conditions as compared to under alkaline conditions. The fuel cell OCPs and peak power densities (PPDs) are 0.72 V and 6.4 mW/cm^2 and 0.96 V and 76 mW/cm^2 under acidic and alkaline conditions, respectively. The corresponding individual electrode polarization curves indicate that the reduced acidic

performance is due to the lower onset potential and the significant kinetic losses of the Cu-tri/C-based cathode (Figure 4.1b). This 11-fold performance increase by shifting from an acidic to alkaline fuel cell operating environment is in agreement with previously reported results by the Gewirth group [22]. Their electrochemical studies found that the oxygen reduction onset potential of the Cu-tri/C catalyst increased by ~30 mV per pH unit and thus predicted a ~410 mV increase in cathode onset potential when pH shifts from 0.3 to 14. From this fuel cell data, cathode onset potentials can be *roughly estimated* as ~0.90 V (0.31 mA/cm^2) and as ~0.52 V (0.38 mA/cm^2) for operation under alkaline and acidic conditions, respectively. This increase of ~380 mV is comparable, though slightly lower, to the enhancement predicted by the electrochemical results. Further increasing the pH may lead to additional improvements in Cu-tri/C-based cathode performance. From here on, due to the superior ORR activity at high pH, the Cu-tri/C-based cathodes are studied under alkaline conditions.

4.3.2 Comparative Analysis of Cu-tri/C-, Pt/C-, & Ag/C-based Cathodes

The cathode performance of the Cu-tri/C catalyst was compared with that of known ORR catalysts, Pt/C and Ag/C, in a microfluidic H_2/O_2 fuel cell with a flowing electrolyte of 1 M KOH. The respective cathode loadings were 4 mg Cu-tri/C/cm^2 (3.76 wt% Cu, in-house synthesized), 2 mg Pt/C/cm^2 (50 wt% Pt on Vulcan, E-Tek), and 6.7 mg Ag/C/cm^2 (60 wt% Ag on Vulcan, E-Tek). Thus the cathode metal loadings are 0.150 mg Cu/cm^2, 1 mg Pt/cm^2, and 4 mg Ag/cm^2. The Ag/C cathode data is from prior studies under similar conditions in an alkaline microfluidic H_2/O_2 fuel cell [26]. For all fuel cell studies, the anode loading was 2 mg Pt/C/cm^2 (again, 50 wt% Pt, so 1 mg Pt/cm^2). Thus, differences in fuel cell performance can be attributed to the different cathode catalyst materials.

The performance of an alkaline microfluidic H_2/O_2 fuel cell operated with Cu-tri/C-, Pt/C-, and Ag/C-based cathodes (Figure 4.2). Figure 4.2a shows representative polarization and power density curves of a fuel cell operated with either Pt/C- or Cu-tri/C-based cathodes which demonstrated peak power densities of 97.8 ± 8.1 and 74.4 ± 2.7 mW/cm^2, respectively (N = 3 for both). The difference in performance can be mainly attributed to the lower open circuit potential of the fuel cell operated with the Cu-tri/C-based cathode, 0.96 ± 0.01 V as compared to the Pt/C-based cathode, 1.06 ± 0.02 V (N = 3 for both). Figure 4.2b shows the corresponding anode and cathode polarization curves for the representative fuel cell data shown in Figure 4.2a. The individual electrode and overall fuel cell performance are similar to those reported in literature [29]. The lower performance of the cell operated with the Cu-tri/C-based cathode can be attributed to a reduced onset potential, which is 103 ± 26 mV lower than that of the Pt/C-based cathode. However, absolute cathode performance may potentially be enhanced by increasing the total Cu-tri/C catalyst loading (> 4 mg/cm^2), as Cu-tri/C is inexpensive compared to Pt/C. As shown in Figure 4.2c, on a per metal basis, the Cu-tri/C-based cathode dramatically

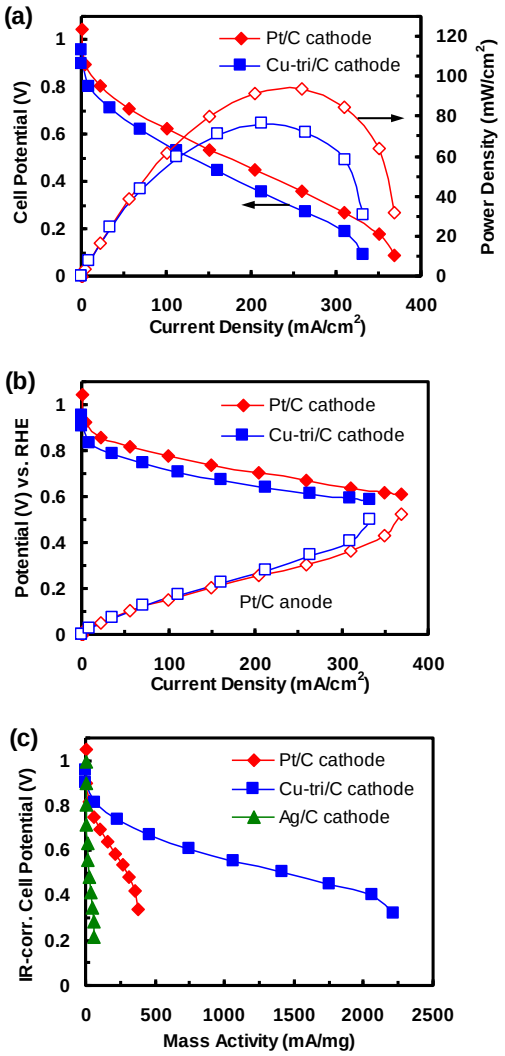

Figure 4.2. **(a)** Polarization and power density curves for a microfluidic H_2/O_2 fuel cell with different cathode catalysts (GDE). **(b)** Corresponding individual electrode polarization curves. **(c)** IR-corrected polarization curves as a function of cathode catalyst metal content (Pt, Cu, and Ag). In all studies a Pt/C anode was used. Studies are performed at room temperature with 50 sccm H_2/O_2 flows and flowing 1 M KOH.

outperforms both the Pt/C-based cathode and the Ag/C-based cathode as shown by the IR-corrected polarization curves as a function of mass activity (mA/mg). The mass activity enhancement is especially pronounced at lower potentials (0.5–0.7 V) and higher current densities where commercial fuel cell-based systems would most likely operate. The mass activities of the fuel cell operated with Cu-tri/C-, Pt/C- and Ag/C-based cathodes are 746 mA/mg (at 0.61 $V_{IR\text{-}corr.}$), 149 mA/mg (at 0.64 $V_{IR\text{-}corr.}$) and 9.5 mA/mg (at 0.63 $V_{IR\text{-}corr.}$), respectively. While the electrodes have not been systematically optimized for mass-specific activity [5,24], these values highlight the potential of the Cu-tri/C as a cathode material for alkaline fuel cell applications.

These results represent the first report of a synthetic multi-Cu complex as a cathode material for alkaline fuel cell applications. Promisingly, the Cu-tri/C cathode performance, which has yet to be optimized, is comparable with that of a Pt/C cathode. Presently, directly comparing the Cu-tri/C performance to that of other Pt-free catalysts is difficult as these studies are performed in either an electrochemical cell [6,24,30] or embedded in a GDE within an operating acidic PEMFCs [5,8].

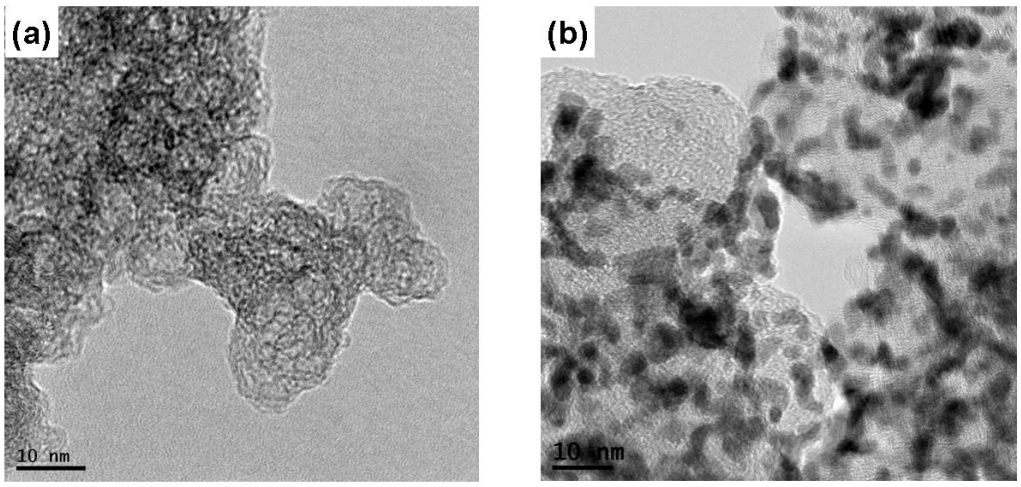

Figure 4.3. Comparative TEM micrographs of **(a)** *in-house* synthesized Cu-tri/C (3.76 wt% Cu) and **(b)** commercial Pt/C (50 wt% Pt on Vulcan, E-Tek). TEM images were captured by Tom Bassett **(a)** and Dr. John Haan **(b)**.

Transmission Electron Microscopy (TEM) micrographs of the catalyst particles show that the high Cu-tri/C-based cathode performance can be attributed, at least in part, to superior catalyst distribution (Figure 4.3). In Figure 4.3a, the Cu-tri species appear well-dispersed on the carbon support suggesting that a significant percentage of the electrocatalytic sites are available. In contrast, the Pt nanoparticles (~3-5 nm) appear to be poorly-dispersed on the carbon support where they tend to overlap and, in some cases, agglomerate (Figure 4.3b). Furthermore the internal volume of the Pt nanoparticles is not electrochemically accessible. Thus, the Pt/C catalyst appears to be using its electrocatalytic sites less efficiently leading to a lower mass activity.

4.3.3 Accelerated Cu-tri/C-based Cathode Durability Studies

The stability of Cu-tri/C-based cathodes is investigated under alkaline fuel cell operating conditions. Initial (0^{th} order) aging studies are performed by studying the degradation of 4 different Cu-tri/C-based cathodes (total loading: 1, 2, 3, and 4 mg/cm^2) over the course of 10 polarization curves. For all studies, the same Pt/C-based anode (total loading: 2 mg/cm^2) was used. As shown in Figure 4.4, all the cathodes experienced marked performance losses over the course of the 10 experiments. The key results are summarized in Table 4.1. From expt. 1 to 10, the fuel cells with 4, 3 and 2 mg/cm^2 Cu-tri/C-based cathodes exhibited a decrease in PPD of ~32 ± 2%. The 1 mg/cm^2 sample experienced a ~47% drop in PPD. This discrepancy can largely be attributed to the scattered performance observed in the

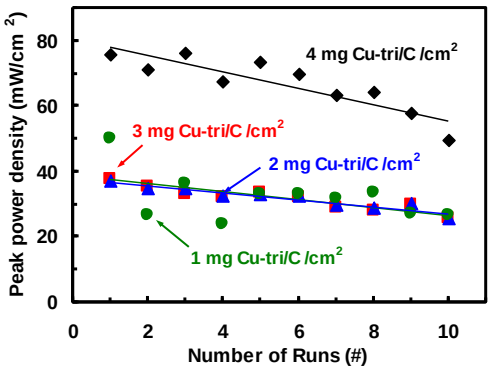

Figure 4.4. Initial aging studies of fuel cells operated with four different Cu-tri/C cathode catalyst loadings. In all studies a Pt/C-based anode was used. Studies are performed at room temperature with 50 sccm H_2/O_2 flows and 0.6 mL/min 1 M KOH flows.

first 4 trials. This variability is also noted in the previous section. In general, the linear fits ascribed to each cathode loadings are comparable indicating that the observed performance degradation may be due to a common (loading-independent) mechanism. Unfortunately, over the course of these studies, the performance of the Pt/C-based anode also significantly degraded; thus, some losses must be attributed to anode deterioration (not shown). Indeed, while each Cu-tri/C-based cathode was used for 10 trials, the Pt/C-based anode was used for 40 trials. Thus, further studies are needed to isolate and quantify the effects of degradation on the cathode under fuel cell operating conditions.

Table 4.1: Performance losses in a fuel cell operated with 4 different Cu-tri/C-based cathode loadings, before and after 10 polarization curves. The *same* Pt/C-based anode was used for all runs. Studies are performed at room temperature with 50 sccm H_2/O_2 flows and 0.6 mL/min 1 M KOH flows.

Cu-tri/C Cathode Loading (mg/cm^2)	Peak Power Density (mW/cm^2)		% decrease
	Initial	Final	
1	49.83	26.45	46.92
2	37.17	25.78	30.64
3	37.65	25.59	32.02
4	75.85	49.38	34.89

To isolate and probe the long-term durability of the Cu-tri/C-based cathodes, accelerated cathode aging studies were performed in a 3-electrode electrochemical cell where the GDEs were subjected to near-realistic fuel cell operating conditions. Two aging techniques employed were potential cycling and potential hold. In Figure 4.5, the Cu-tri/C-based cathode was aged in O_2-saturated 1 M KOH by potential cycling between 0.535 and 1.035 V vs RHE at a 5 mV/s scan rate. This range was chosen to simulate the potentials that could be experienced by a cathode in an operating alkaline fuel cell (see Figure 4.2b). The ORR activity of the Cu-tri/C-based cathode degrades substantially over 6000 cycles. As the insert in Figure 4.5 shows, the cathode performance drops ~61% over the course of the aging experiment. The initial degradation rates

appear more rapid than the later rates. In the first 100 cycles, the performance drops ~16% (~0.16% decay per cycle). From 3000 to 6000 cycles, the performance drops ~29% (~0.01% decay per cycle).

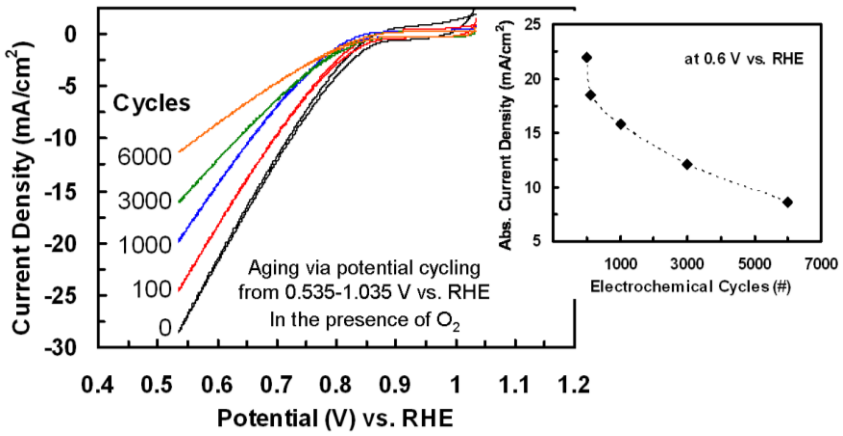

Figure 4.5. Cu-tri/C-based cathode (GDE) aging as a function of electrochemical cycles between 0.535 and 1.035 V vs. RHE at a 5 mV/s scan rate in a 3-electrode cell in O_2-saturated 1 M KOH at room temperature. **Insert:** absolute current density at 0.6 V vs. RHE as a function of cycles. Cathode loading: 4 mg Cu-tri/C/cm^2; geometric electrode surface area: 4 cm^2.

In Figure 4.6, the Cu-tri/C-based cathode was aged in O_2-saturated 1 M KOH by holding the potential at 0.535 V vs. RHE for a 24 hr period. The cathode potential would correspond to a fuel cell operating at a very high current density (low cell potential). Figure 4.6a shows the chronoamperometric response of the cathode during the 24 hr potential hold. Over the 24 hr period, the cathode performance drops ~45%. Most of these performance losses occur in the first 14 hrs of operation. In Figure 4.6b, the cyclic voltammograms of oxygen reduction performance are obtained at 0, 14 and 24 hrs by potential cycling between 0.535 and 1.035 V vs RHE at a 5 mV/s scan rate. These CVs also show that the majority of the performance losses are observed between 0 and 14 hrs.

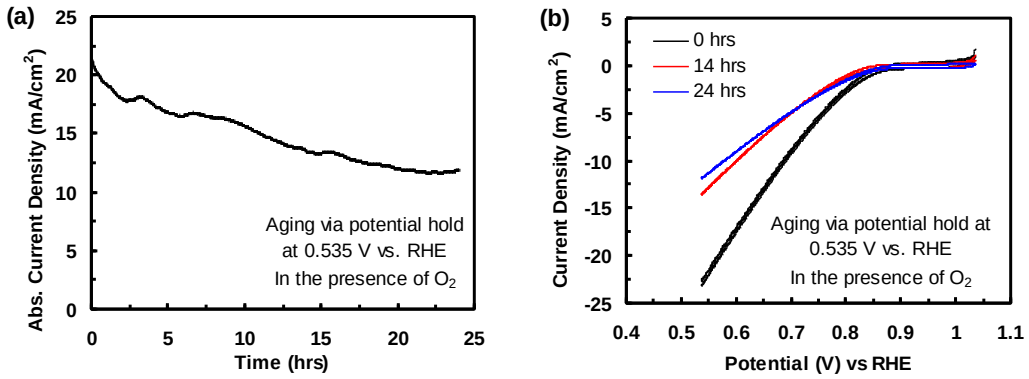

Figure 4.6. Cu-tri/C-based cathode aging via potential hold at 0.535 V vs. RHE. **(a)** The cathode chronoamperometric response (in absolute current density) as a function of constant potential aging. **(b)** Cyclic voltammograms are taken at 0, 14 and 24 hrs between 0.535 and 1.035 V vs. RHE at a 5 mV/s scan rate. Studies are performed in a 3-electrode cell in an O_2-saturated 1 M KOH at room temperature. Cathode loading: 4 mg Cu-tri/C /cm^2; geometric electrode surface area: 4 cm^2

Both accelerated cathode durability studies reveal similar trends suggesting the presence of multiple degradation regimes with an initial region of rapid losses followed by a second broader region of slower losses. Further durability analyses are required to better understand, and hopefully mitigate, these adverse processes.

One possible degradation process is the formation of copper dihydroxide ($Cu(OH)_2$), which would occur when any free Cu ions combine with hydroxyl ions to rapidly form insoluble greenish precipitant. Due to the high hydroxyl ion concentrations at the alkaline fuel cell cathodes, any copper dihydroxide that forms would immediately precipitate onto the Cu-tri/C particles possibly creating an electrochemically inactive film. This process would likely occur over a short time-frame as any unstable or incompletely formed Cu-tri species would react. In the longer term, this process could also contribute to the slower *in-situ* cathode degradation patterns.

4.3.4 Effects of Cu Content on Carbon Support

The Cu-tri/C-based cathode performance is investigated as a function of Cu content on the Vulcan carbon content. Given that high cathode performance is obtained with a relatively low Cu loading, the effects of increasing Cu concentration on the Vulcan support are studied. The two higher Cu concentration catalysts investigated are 7.52 and 11.28 wt%, which correspond to 2 and 3 times the original Cu loading.

Table 4.2. Open circuit potentials and peak power densities for an alkaline microfluidic H_2/O_2 fuel cell operated with Cu-tri/C-based cathodes with 3.76, 7.52 and 11.28 wt% Cu (N = 3). For all studies, the total loading of the Cu-tri/C-based cathodes was 4 mg/cm^2 and a Pt/C-based anode was used. Studies are performed at room temperature with 50 sccm H_2/O_2 flows and 0.6 mL/min 1 M KOH flows.

Cu content (wt%)	Open Circuit Potential (V)	Peak Power Density (mW/cm^2)
3.76	0.96 ± 0.01	74.4 ± 2.7
7.52	0.96 ± 0.03	59.6 ± 10.4
11.28	0.95 ± 0.04	86.9 ± 13.7

Table 4.2 shows the comparison of OCPs and PPDs for fuel cells operated with three different Cu-tri/C-based cathodes (3.76, 7.52, and 11.28 wt% Cu). In general, increasing the Cu content on the Vulcan support does not appear to lead to any substantial enhancement in cathode performance. In fact, the cathode performance appears to be less stable, in terms of both OCP and PPD, with increasing Cu content. Furthermore, on a per metal basis, the cathode performance actually reduces significantly with increasing Cu content. As seen in the TEM micrograph in Figure 4.4a, the catalyst appears well-distributed on the carbon surface at low Cu loadings. Thus, increasing the Cu content may lead to agglomeration where the bulky triazole ligands hinder reactant transport to the electroactive Cu sites. Moreover, as the ligands are not good electron conductors, the Cu sites must be in close proximity to the carbon surface for the ORR to occur; thus, only a fraction may be electrochemically active. While increasing Cu

content does not appear to improve cathode performance, reducing Cu content may increase stability without sacrificing activity.

4.4 Conclusions

Building on the promising ORR performance of Cu-tri/C catalyst in a 3-electrode cell especially under alkaline conditions [22], the performance and durability of the Cu-tri/C-based cathodes were investigated for fuel cell applications. For alkaline fuel cell applications, biomimetic Cu-tri/C-based cathodes appear a promising alternative to Pt/C-based cathodes. Despite the reduced electrocatalyst loading, the absolute performance of the Cu-tri/C-based cathode is comparable to the Pt/C-based cathode. Furthermore, at a commercially-relevant fuel cell potential (~0.6 V), the measured mass activity of an unoptimized Cu-tri/C-based cathode was significantly greater than that of similar Pt/C- and Ag/C-based cathodes. Accelerated cathode durability studies suggested multiple degradation regimes at various time scales and highlight the need for improvements in Cu-tri/C-based cathode stability under fuel cell operating conditions.

Looking ahead, the performance and, in particular, the durability of these unoptimized cathodes may be enhanced via optimizing synthesis procedures such as tailoring ligand design, and varying support materials. For example, at present, Cu and ligand species are physically deposited via precipitation on the Vulcan supports. However, such a technique can be inefficient as catalyst materials must be appropriately spaced and attached to the carbon surface which limits the effective loadings and extended stability of these species. Targeted deposition of Cu and ligand species onto carbon nanotube supports via electrochemical grafting may improve catalyst utilization, performance, and stability under fuel cell operating conditions [31,32].

Furthermore, the performance, specifically the mass activity, and reproducibility of Cu-tri/C-based cathodes may be enhanced via improved GDE preparation methods such as optimizing catalyst loading, particle distribution and uniformity, and catalyst-to-binder ratios [5,24]. For example, at present, the nominal loading of Cu-tri/C catalyst on the gas diffusion layer is 4 mg/cm^2 but the actual loading may vary depending upon the "experimenter". Furthermore, depending on the uniformity of this loading, the electrochemically available area may vary significantly depending on the electrolyte channel position. Improving and standardizing GDE preparation procedures will enable greater electrode-to-electrode reproducibility. Moreover, these optimizations will enable better comparisons between this catalyst and other Pt-free catalysts reported in literature. In particular, volumetric ORR activity measurements, which are the most appropriate criterion for comparing cathodes based on Pt-free catalysts [1,5], can only be made if the catalyst layer thickness is uniform and reproducible.

4.5 References

1. Gasteiger, H.A., S.S. Kocha, B. Sompalli, and F.T. Wagner, *Activity benchmarks and requirements for Pt, Pt-alloy, and non-Pt oxygen reduction catalysts for PEMFCs.* Applied Catalysis B - Environmental, 2005. **56**(1-2): p. 9-35.
2. Carrette, L., K.A. Friedrich, and U. Stimming, *Fuel Cells - Fundamentals and Applications.* ChemPhysChem, 2001. **1**: p. 5-39.
3. Borup, R., J. Meyers, B. Pivovar, Y.S. Kim, R. Mukundan, N. Garland, D. Myers, M. Wilson, F. Garzon, D. Wood, P. Zelenay, K. More, K. Stroh, T. Zawodzinski, J. Boncella, J.E. McGrath, M. Inaba, K. Miyatake, M. Hori, K. Ota, Z. Ogumi, S. Miyata, A. Nishikata, Z. Siroma, Y. Uchimoto, K. Yasuda, K.I. Kimijima, and N. Iwashita, *Scientific aspects of polymer electrolyte fuel cell durability and degradation.* Chemical Reviews, 2007. **107**(10): p. 3904-3951.
4. Norskov, J.K., J. Rossmeisl, A. Logadottir, L. Lindqvist, J.R. Kitchin, T. Bligaard, and H. Jonsson, *Origin of the overpotential for oxygen reduction at a fuel-cell cathode.* Journal of Physical Chemistry B, 2004. **108**(46): p. 17886-17892.
5. Lefevre, M., E. Proietti, F. Jaouen, and J.P. Dodelet, *Iron-Based Catalysts with Improved Oxygen Reduction Activity in Polymer Electrolyte Fuel Cells.* Science, 2009. **324**(5923): p. 71-74.
6. Kothandaraman, R., V. Nallathambi, K. Artyushkova, and S.C. Barton, *Non-precious oxygen reduction catalysts prepared by high-pressure pyrolysis for low-temperature fuel cells.* Applied Catalysis B-Environmental, 2009. **92**(1-2): p. 209-216.
7. Guinel, M.J.F., A. Bonakdarpour, B.A. Wang, P.K. Babu, F. Ernst, N. Ramaswamy, S. Mukerjee, and A. Wieckowski, *Carbon-Supported, Selenium-Modified Ruthenium-Molybdenum Catalysts for Oxygen Reduction in Acidic Media.* Chemsuschem, 2009. **2**(7): p. 658-664.

8. Bashyam, R. and P. Zelenay, *A class of non-precious metal composite catalysts for fuel cells.* Nature, 2006. **443**(7107): p. 63-66.
9. Cracknell, J.A., K.A. Vincent, and F.A. Armstrong, *Enzymes as working or inspirational electrocatalysts for fuel cells and electrolysis.* Chemical Reviews, 2008. **108**(7): p. 2439-2461.
10. Mano, N., V. Soukharev, and A. Heller, *A laccase-wiring redox hydrogel for efficient catalysis of O-2 electroreduction.* Journal of Physical Chemistry B, 2006. **110**(23): p. 11180-11187.
11. Blanford, C.F., C.E. Foster, R.S. Heath, and F.A. Armstrong, *Efficient electrocatalytic oxygen reduction by the 'blue' copper oxidase, laccase, directly attached to chemically modified carbons.* Faraday Discussions, 2008. **140**: p. 319-335.
12. Blanford, C.F., R.S. Heath, and F.A. Armstrong, *A stable electrode for high-potential, electrocatalytic O-2 reduction based on rational attachment of a blue copper oxidase to a graphite surface.* Chemical Communications, 2007(17): p. 1710-1712.
13. Gewirth, A.A. and M.S. Thorum, *Electroreduction of Dioxygen for Fuel-Cell Applications: Materials and Challenges.* Inorganic Chemistry, 2010. **49**(8): p. 3557-3566.
14. McCrory, C.C.L., X. Ottenwaelder, T.D.P. Stack, and C.E.D. Chidsey, *Kinetic and mechanistic studies of the electrocatalytic reduction of O-2 to H2O with mononuclear Cu complexes of substituted 1,10-phenanthrolines.* Journal of Physical Chemistry A, 2007. **111**(49): p. 12641-12650.
15. Zhang, J.J. and F.C. Anson, *Electrochemistry of the Cu(II) Complex of 4,7-Diphenyl-1,10-Phenathrolinedisulfonate Adsorbed on Graphite-Electrodes and Its Behavior as an Electrocatalyst for the Reuduction of O_2 and H_2O_2.* Journal of Electroanalytical Chemistry, 1992. **341**(1-2): p. 323-341.
16. Zhang, J.J. and F.C. Anson, *Complexes of Cu(II) with Electroactive Chelating Ligands Adsorbed on Graphite-Electrodes - Surface Coordination Chemistry and Electrocatalysis.* Journal of Electroanalytical Chemistry, 1993. **348**(1-2): p. 81-97.
17. Slowinski, K., Z. Kublik, R. Bilewicz, and M. Pietraszkiewicz, *Electrocatalysis of Oxygen Reduction by a Copper(II) Hexaazamamacrocylic Complex.* Journal of the Chemical Society-Chemical Communications, 1994(9): p. 1087-1088.
18. Kim, J. and A.A. Gewirth, *Electrocatalysis of oxygen reduction by Cu-containing polymer films on glassy carbon electrodes.* Bulletin of the Korean Chemical Society, 2007. **28**(8): p. 1322-1328.
19. Cai, C.X., K.H. Xue, X.Y. Xu, and Q.H. Luo, *Electrocatalysis for the reduction of O-2 and H2O2 based on complex of copper(II) with the tris(3-aminopropyl)amine and imidazole ligands.* Journal of Applied Electrochemistry, 1997. **27**(7): p. 793-798.
20. Dias, V.L.N., E.N. Fernandes, L.M.S. da Silva, E.P. Marques, J.J. Zhang, and A.L.B. Marques, *Electrochemical reduction of oxygen and hydrogen peroxide catalyzed by a surface copper(II)-2,4,6-tris(2-piridil)-1,3,5-triazine complex adsorbed on a graphite electrode.* Journal of Power Sources, 2005. **142**(1-2): p. 10-17.
21. Fukuzumi, S., H. Kotani, H.R. Lucas, K. Doi, T. Suenobu, R.L. Peterson, and K.D. Karlin, *Mononuclear Copper Complex-Catalyzed Four-Electron Reduction of Oxygen.* Journal of the American Chemical Society, 2010. **132**(20): p. 6874-+.
22. Thorum, M.S., J. Yadav, and A.A. Gewirth, *Oxygen Reduction Activity of a Copper Complex of 3,5-Diamino-1,2,4-triazole Supported on Carbon Black.* Angewandte Chemie-International Edition, 2009. **48**(1): p. 165-167.
23. Spendelow, J.S. and A. Wieckowski, *Electrocatalysis of oxygen reduction and small alcohol oxidation in alkaline media.* Physical Chemistry Chemical Physics, 2007. **9**(21): p. 2654-2675.
24. Meng, H., F. Jaouen, E. Proietti, M. Lefevre, and J.P. Dodelet, *pH-effect on oxygen reduction activity of Fe-based electro-catalysts.* Electrochemistry Communications, 2009. **11**(10): p. 1986-1989.
25. Jayashree, R.S., M. Mitchell, D. Natarajan, L.J. Markoski, and P.J.A. Kenis, *Microfluidic hydrogen fuel cell with a liquid electrolyte.* Langmuir, 2007. **23**(13): p. 6871-6874.
26. Brushett, F.R., W.P. Zhou, R.S. Jayashree, and P.J.A. Kenis, *Alkaline Microfluidic Hydrogen-Oxygen Fuel Cell as a Cathode Characterization Platform.* Journal of the Electrochemical Society, 2009. **156**(5): p. B565-B571.
27. Brushett, F.R., H.T. Duong, J.W.D. Ng, R.L. Behrens, A. Wieckowski, and P.J.A. Kenis, *Investigation of Pt, Pt_3Co, and Pt_3Co/Mo cathodes for the ORR in a Microfluidic H_2/O_2 Fuel Cell.* Journal of the Electrochemical Society, 2010. **157**(6): p. B837-845.

28. Choban, E.R., P. Waszczuk, and P.J.A. Kenis, *Characterization of limiting factors in laminar flow-based membraneless microfuel cells.* Electrochemical and Solid State Letters, 2005. **8**(7): p. A348-A352.
29. Zeng, R., S.D. Poynton, J.P. Kizewski, R.C.T. Slade, and J.R. Varcoe, *A novel reference electrode for application in alkaline polymer electrolyte membrane fuel cells.* Electrochemistry Communications, 2010. **12**(6): p. 823-825.
30. Olson, T.S., S. Pylypenko, P. Atanassov, K. Asazawa, K. Yamada, and H. Tanaka, *Anion-Exchange Membrane Fuel Cells: Dual-Site Mechanism of Oxygen Reduction Reaction in Alkaline Media on Cobalt-Polypyrrole Electrocatalysts.* Journal of Physical Chemistry C, 2010. **114**(11): p. 5049-5059.
31. Le Goff, A., V. Artero, B. Jousselme, P.D. Tran, N. Guillet, R. Metaye, A. Fihri, S. Palacin, and M. Fontecave, *From Hydrogenases to Noble Metal-Free Catalytic Nanomaterials for H-2 Production and Uptake.* Science, 2009. **326**(5958): p. 1384-1387.
32. Griveau, S., D. Mercier, C. Vautrin-Ul, and A. Chausse, *Electrochemical grafting by reduction of 4-aminoethylbenzenediazonium salt: Application to the immobilization of (bio)molecules.* Electrochemistry Communications, 2007. **9**(12): p. 2768-2773.

Chapter 5

X-ray Micro-computed Tomography Analyses of Fuel Cell Electrodes

5.1 Introduction

Due to their high efficiency, high energy density and low emissions, fuel cell-based power sources have been extensively investigated as energy conversion systems for both next-generation portable electronics and transportation applications [1-4]. Unfortunately, broad commercialization of fuel cell technologies is hampered by prohibitive component cost (*i.e.,* platinum catalysts) and insufficient operational lifetimes of various components [2]. Developing a better understanding of the complex electrochemical, transport and degradation processes that govern the performance and durability of catalysts / electrodes *within an operating fuel cell* is critical to designing the robust, cheaper configurations required for commercial introduction [5-8]. Detailed *in-situ* studies of individual electrode processes in fuel cells, however, are complicated by other factors such as water management, uneven performance across the electrode areas, and temperature gradients. Indeed, too many processes are interdependent of the same parameters necessitating the development of novel analytical platforms with high degrees of freedom.

To this end, pH-flexible microfluidic H_2/O_2 fuel cells have been developed as versatile electro-analytical platforms for the characterization of catalyst / electrode performance under realistic fuel cell operating conditions (*e.g.,* high current densities) without aforementioned adverse factors complicating experiments and data analysis [9,10]. While this platform provides detailed electrochemical information on electrode performance characteristics, the dynamic relationship between these events and the physical properties of these materials remain unknown.

For example, the choice of gas diffusion layer (GDL) is critical to performance as the material is responsible for (*i*) the transport of reactants from the flow channel to the catalyst layer, (*ii*) the drainage of liquid from the catalyst layer into either the flow channel or the electrolyte / membrane, and (*iii*) conduction of electrons with low resistance from the catalyst layer to the current collectors [11]. Furthermore, the electrochemical activity of an electrode is dependent on catalyst layer morphology (*i.e.*, particle distribution, catalyst site availability). Thus, improving fuel cell performance and durability requires a detailed understanding of fundamental shifts in electrochemical activity and physical structure of components, particularly gas diffusion electrodes, as a function of operating conditions and working lifetime [2].

In general, gas diffusion electrodes (GDEs) consist of (*i*) a catalyst layer which interfaces with the electrolyte / membrane, (*ii*) a microporous layer (a mixture of hydrophobic polytetrafluoroethylene (PTFE) and carbon particles) which prevents gas diffusion layer flooding, and (*iii*) a macroporous backing layer (often PTFE treated) which distributes reactant gases across the GDE (Figure 5.1) [11-13]. Understanding and optimizing each composition and structure layer is critical for overall electrode performance. For example, Lin and Van Nyugen demonstrated that the PTFE content in the macroporous backing layer and the presence of microporous layer have significant implication on the efficiency of water and gas transport in the electrode structure and; consequently, on the electrode performance [13]. Furthermore, Roshandel *et al.* showed that non-uniform compression (*i.e.*, from a serpentine channel within a fuel cell stack) adversely effects the pore distribution in the macroporous backing layer, which, in turn, leads to poor mass transport in those regions (*i.e.*, flooding) [14].

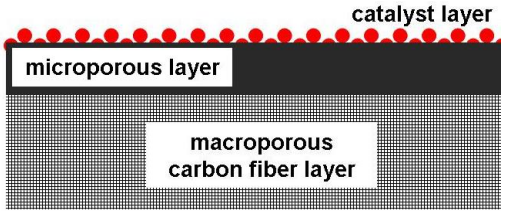

Figure 5.1. Simple schematic of gas diffusion electrode (GDE)

Moreover, the performance and operating lifetimes of liquid electrolyte-based alkaline fuel cells (AFCs) are limited by GDE hydrophobicity losses, due to PTFE degradation via peroxide radical attacks [15].

A wide range of experimental techniques are used to probe the physical and chemical structure of gas diffusion electrodes. The most commonly employed method is scanning electron microscopy (SEM), often in conjunction with energy dispersive spectroscopy (EDS). A versatile technique, SEM / EDS enables simultaneous analysis the chemical and physical characteristics of a material surface over a broad range of magnifications (10x - 100,000x). SEM / EDS analyses provide detailed information about morphology and composition of external electrode surfaces (*i.e.*, catalyst layer, gas diffusion layer). However, using SEM / EDS to probe internal electrode structure requires cross-sectional imaging and; thus, sample destruction (*e.g.*, nitrogen cracking, focused ion beam). Furthermore, SEM / EDS apparatuses require high vacuum (10^{-6} - 10^{-9} torr for traditional systems, $1 - 50$ torr for environmental systems) which limit their applicability for *in-operandi* fuel cell studies (*e.g.*, liquid water distribution in a GDE). Transmission electron microscopy (TEM) is another common analytical technique, which routinely used for physical characterization of nano-scale fuel cell catalyst particles (*e.g*, size distribution, morphology). However, TEM has limited applicability for full electrode analysis because sample thicknesses must be < 500 nm which necessitates electrode destruction. In addition, TEM apparatuses require high vacuum for imaging.

The most common technique for probing internal electrode porosity is mercury intrusion porosimetry (MIP), while other fluids are also utilized to verify MIP (*i.e.*, decane-wetting) [16]. While MIP is a non-destructive technique, the method is an "indirect" measure that provide bulk porosity value but give little to no information about the internal structure, heterogeneous

distribution or anisotropy of pores within electrodes [17]. However, such quantitative information is critical for the development of accurate micro- and macro-scale fuel cell numerical models. Furthermore, these porosimetry methods are incompatible with *in-situ* fuel cell analyses.

The distribution and transport of liquid water within fuel cells are commonly studied via direct visualization [18], neutron radiography [19-22], and/or magnetic resonance imaging (MRI) [23-25]. Water accumulation at different locations in flow-fields and on the GDL surface may be observed using custom-made transparent components and high resolution cameras [18]. These analyses provide useful data for water behavior in fuel cell flow channels, but provide little to no information about water content within the GDEs. Neutron radiography enables two-dimensional visualization of liquid water distribution within large-scale operating fuel cell without the need to custom manufactured components [19,20]. This is because neutrons are strongly attenuated by water relative to other fuel cell component materials. For example, neutrons can penetrate more than 2-3 cm of carbon and aluminum, whereas sensitivities to 30 μm of water can be achieved [22]. However, neutron radiography is hindered by (*i*) lack of accessibility to high flux neutron sources and (*ii*) low spatial and temporal resolution which limit the ability to locate the liquid water within three-dimensional gas diffusion layers and flow-fields within operating fuel cells [22,26]. MRI enables three-dimensional visualization of liquid water transport across polymer electrolyte membranes (PEMs) and within flow-fields [23,24]. However, due to the presence of magnetically inductive carbonaceous materials in a fuel cell, measurements often require custom-made architectures, such graphite-coated Teflon flow-fields, whose properties may differ from an actual fuel cell design. Furthermore, the high electrical conductivity of the carbonaceous GDL prevents the analysis of internal water distribution [26].

Newly-emerging X-ray micro/nano-computed tomography (Micro/NanoCT) techniques enable multi-scale high-resolution three-dimensional visualizations of GDE architectures as well as liquid species transport through those components [17,26-38]. A powerful visualization technique, tomographic imaging identifies different phases / elements as well as heterogeneous densities via variations in X-ray absorption [36]. Though employed in other disciplines (*i.e.*, geological materials, cellular solids) for some time [31], researchers have only recently begun to explore the utility of Micro/NanoCT imaging for low temperature fuel cell applications. To date, fuel cell driven MicroCT investigations have been focused on liquid water saturation in acidic fuel cell cathodes [26,30,38] and, most recently, structural analysis of electrode architectures with a focus on providing more accurate parameters for numerical models [17,29,35]. NanoCT has also been employed for electrode structural analyses; however, this method are both financially and computationally more expensive than MicroCT [27,32-34,37]. *However, to date, no efforts have focused on developing structure-activity relationships for electrodes within operating fuel cells.* This chapter seeks to develop robust methods for analyzing electrode structures using MicroCT imaging and then to use these methods to correlate shifts in electrode performance to changes in physical structure. These combined studies can then be used to probe the individual electrode structure-activity relationships as a function of preparation protocols and fuel operating conditions.

5.2 Experimental

5.2.1 Gas Diffusion Electrode Preparation

For acidic fuel cells, electrode inks consisted of a desired amount of catalyst, Nafion (5 wt% solution, Solution Technology) as a binder, and 200 µL Millipore water (18.2 MΩ) and 200 µL of isopropyl alcohol as carrier solvents. For all acidic electrodes, the catalyst to Nafion ratio was

maintained at 30:1 [10]. For alkaline fuel cells, electrode inks consisted of a desired amount of catalyst, polytetrafluoroethylene powder (PTFE, Aldrich) as a binder, and 200 µL Millipore water (18.2 MΩ) and 200 µL of isopropyl alcohol as carrier solvents. For all alkaline electrodes, the PTFE loading was 40 wt% of the total catalyst layer loading (catalyst + PTFE) [9]. All catalyst inks are sonicated (Branson 3510) for at least two hours to ensure uniform mixing and painted on a teflonized carbon side of gas diffusion layers to create a gas diffusion electrode (GDE). Two different GDLs are used: EFCG "S" type (E-Tek), and EFCG Phosphoric Acid Fuel Cell Electrode (E-Tek). Both GDLs consist of a PTFE-treated Toray carbon paper TGP-H-120 with a teflonized microporous layer one side. The alkaline electrodes were then sintered under a nitrogen (N_2) atmosphere at 330°C for 20 min in a preheated tube furnace (Lindberg/Blue) [39]. The geometric surface area of the electrodes was 4 cm^2. Some of the fabricated GDEs were hot-pressed in a Carver 3851-0 manual press at varying pressures and 125 ± 10 °C for 5 min.

5.2.2 Fuel Cell Assembly and Testing

Two GDEs were placed on opposite sides of a 0.15-cm thick polymethylmethacrylate (PMMA) sheet, such that the catalyst-covered sides interfaced with the 3-cm long and 0.33-cm wide precision-machined window. The window has an inlet and outlet on either side such that the aqueous electrolyte flows between the electrodes. Two 0.1-cm thick graphite plates with access windows (4 (L) x 0.6 (W) cm^2) are placed on the outside of the GDEs and served as current collectors. The hydrogen and oxygen gas flow chambers (5 (L) x 1 (W) x 0.5 (H) cm^3) were precision-machined into polycarbonate sheets. This multilayered assembly was held together using binder clips (Highmark). Prior to experimentation, the fuel cell assembly was leak tested by flowing DI water through the fluidic chamber for several minutes. In the few

cases leaking was observed, typically due to misalignment of the layers, the cell was disassembled and realigned. No leaking was observed during subsequent operation.

All fuel cell experiments were conducted using either General Purpose Electrochemical Software (GPES, EcoChemie) or NOVA Software (EcoChemie) controlled by a potentiostat (Autolab PGSTAT-30, EcoChemie). Sulfuric acid (H_2SO_4, GFS Chemicals), perchloric acid ($HClO_4$, Aldrich), and potassium hydroxide (KOH, Mallinckrodt, 88%, balance of H_2O) were used as electrolytes. Electrolyte flow rates were varied from 0.0 to 0.9 mL/min using a syringe pump (2200 PHD, Harvard Apparatus). Oxygen and hydrogen gases (S.J. Smith, laboratory grade) were run through the gas flow chambers at flow rates from 10 to 50 sccm each. Once the gas and liquid streams were introduced, the fuel cell was held at open circuit potential (OCP) for 5 min to ensure that the cell potential stabilized prior to testing. Fuel cell polarization curves were obtained by steady-state chronoamperometric measurements at different cell potentials using a potentiostat. Potentiostat leads were attached to the anodic and cathodic graphite current collectors via copper alligator clips. The working electrode lead was attached to the anode while the reference and counter electrode leads were combined and attached to the cathode. The potentiostat was used to generate an applied potential, and a multimeter (15 XP Meterman, 87 III Fluke, or 179 Fluke), with its leads attached to the anodic and cathodic graphite current collectors, was used to determine the actual cell potential. This configuration enables the elimination of any contributions due to connect resistances between the alligator clips of the leads and the graphite current collector plates. The exposed geometric electrode surface area (1 cm^2) was used to calculate the current and power densities. After exiting the fuel cell, the aqueous electrolyte stream was collected in a beaker with a reference electrode (Ag/AgCl in saturated NaCl, BASi). The anode and cathode polarization losses are independently

characterized using two multimeters, functioning in voltmeter mode, and attached to the reference electrode and each of the graphite plate current collectors.

5.2.3 MicroCT Experimental Set-up

All gas diffusion electrodes were imaged using either a Micro-XCT 200 or a Micro-XCT 400 (both Xradia with proprietary operating and reconstruction software). Both instruments are located in the Microscopy Suite of the Imaging Technology Group in the Beckman Institute of Advanced Science and Technology at the University of Illinois in Urbana-Champaign [40] In both instruments are closed systems which use a cone beam reconstruction method where a micro-focus X-ray tube (Hamamatsu) was used as a X-ray source and a scintillator with a 4-megapixel thermoelectrically-cooled charged-coupled device camera (Andor) was used a X-ray collector. During imaging, as the sample was rotated stepwise over 180 °, 365 to 369 projection images, typically called shadow-graphs, were captured. From these shadow-graphs, 2D radiographic cross-sectional image stacks and 3D tomographic virtual models of the GDE are computed providing detailed information about layer thickness, internal architecture and species location. The resolution of these generated images was determined by the sample distance from both the X-ray source and the X-ray collector.

Two different sample preparation methods, referred to as procedures #1 and #2 in this chapter, were used (Figure 5.2). In the first method (procedure #1), an approximately 1.5 (W) x 5 (L) mm^2 section was *cut from* the GDE and mounted in a polyimide tube (0.0641 in inner diameter, 0.0125 in wall thickness, Small Parts) (Figure 5.2a). The sample was then placed on a rotating stand between the source and the collector within the MicroCT (Figure 5.2a). In the second method (procedure #2), the *whole* GDE is clamped in a rotating stand such that only a small corner is exposed to the X-ray beam between the source and the collector within the

MicroCT (Figure 5.2b). Unless specified mentioned, all sample images shown were prepared using procedure #1.

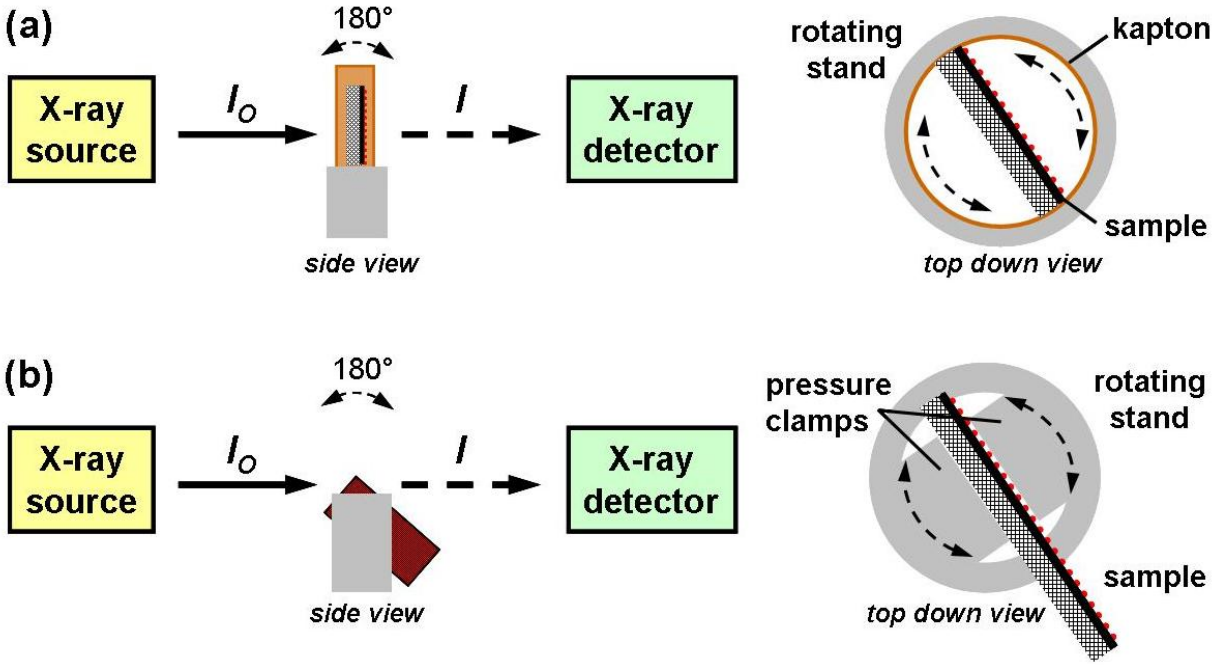

Figure 5.2. Cartoon of the MicroCT experimental set-up for GDE analysis. **(a)** In procedure #1 a slice is cut from the GDE, placed in a kapton sheath and rotated in the X-ray beam field. **(b)** In procedure #2 the whole GDE is clamped in a rotating stand and a corner is exposed to the X-ray beam field.

5.2.4 Multi-point Thickness Measurements

Sample thickness measurements, in the z-direction, were performed on the 2D radiographic image stacks produced by MicroCT analyses. Measurements were performed using the ruler tool in the proprietary Xradia controller software. Local layer thicknesses were measured at multiple points ($N \geq 38$) across each GDE sample, in the xy plane, to determine overall average thicknesses. Prior to calculating the mean and standard deviation, a quartile technique is employed to eliminate outliers from the data set. Initially, find the median value of the data set of *n* points (Eq. 5.1):

$$Median = \frac{n+1}{2} \tag{5.1}$$

Once this median value is obtained, quartiles are determined. The first quartile, Q_1, cuts off the lowest 25% of the data (Eq. 5.2), the second quartile, Q_2, cuts the data in half, and the third quartile, Q_3, cuts off the highest 25% of the data set (Eq. 5.3). The interquartile range, *IQR*, is the difference between the third quartile and the first quartile (Eq. 5.4).

$$Q_1 = 0.25(n+1) \tag{5.2}$$

$$Q_3 = 0.75(n+1) \tag{5.3}$$

$$IQR = Q_3 - Q_1 \tag{5.4}$$

The *IQR* is defined as a standard deviation and is used to measure inner and outer fences in the distributions. The inner and outer fences can be shown by Eq. 5.5 and Eq. 5.6:

$$F_{inner} = Q_2 \pm 1.5 * IQR \tag{5.5}$$

$$F_{outer} = Q_2 \pm 3 * IQR \tag{5.6}$$

Therefore the inner fence can be defined as 1.5 standard deviations in either direction. The outer fence can be defined as 3 standard deviations in either direction. There are two different types of outliers, mild and extreme. Mild outliers are defined as any points beyond the inner fence but inside the outer fence on either side. Extreme outliers are defined as any points beyond the outer fence on either side. Only the extreme outliers are excluded from data set when calculating the mean and standard deviation for the layers in the GDE sample.

5.2.5 Quantitative Image Analysis

Quantitative image reconstruction was performed using Amira software package (Version 5.3, Visage Imaging) on a computer workstation (2x 3.00 GHz Intel Quadcore Xeon processor, 32 GB RAM, Windows Vista x64 operating system). The workstation is located in the

Visualization Laboratory of the Imaging Technology Group in the Beckman Institute of Advanced Science and Technology at the University of Illinois in Urbana-Champaign [40].

5.3 Results & Discussion

5.3.1 Overview of MicroCT Analysis

As mentioned in the section 5.1, microtomography (MicroCT) is an X-ray absorption method identifies different phases / elements as well as heterogeneous densities via variations in X-ray attenuation. For these experiments, X-rays are generated in tube within the MicroCT system. Here, electrons flow through a filament (*e.g.*, tungsten) at a potential kVp relative to the target (*e.g.*, copper, molybdenum). Electrons emitted from the filament bombard the metal target and produce a continuous spectrum, a characteristics radiation, and a substantial amount of heat. Note that, unlike synchrotron radiation, the incident beam generated by X-ray tube is polychromatic including contributions from both the characteristic radiation and the continuous spectrum. Often lower energy radiation (softer X-rays) is filtered (beam hardening) prior to exposure to the specimen to prevent detector saturation. The incident beam intensity can be controlled by changing the accelerating voltage and the current passing through the filament.

The interaction of X-rays with matter can be described by the following expression [36]:

$$I = I_O \exp\left[\left(\frac{-\mu}{\rho}\right)\rho x\right] \tag{5.7}$$

Where I_o is the intensity of the unattentuated X-ray beam, I is the intensity of the attenuated X-ray beam, x is the material thickness, μ is the material linear attenuation coefficient, and ρ is the material density. As shown, by the mass attenuation coefficient (μ/ρ), the fundamental basis of the amount of attenuation is the number of atoms encountered by the X-ray beam. Mass

attenuation coefficients are a materials property and a strong function of the absorber atomic number (Z) and the X-ray wavelength (λ) [36].

For these experiments, a cone beam reconstruction method is used. In this technique, X-rays diverge in three dimensions from the source, pass through the specimen, and are recorded on a 2D area detector consisting of a scintillator and a CCD camera. As the sample rotates in the beam field, a number of projection images, often referred to as shadow-graphs are collected. From, these projection images, 2D radiographic cross-sectional image stacks and 3D tomographic virtual models of the GDE are computed providing detailed information about layer thickness, internal architecture and species location. Image resolution is determined by magnification, and the sample distance from detector and source. Image contrast is determined by the X-ray beam intensity and by the amount of time the image exposed to the X-ray beam. A detailed discussion of the MicroCT principles made by found in the following reference [36].

5.3.2 Qualitative Visualization of 2- and 3-D GDE Structure using MicroCT

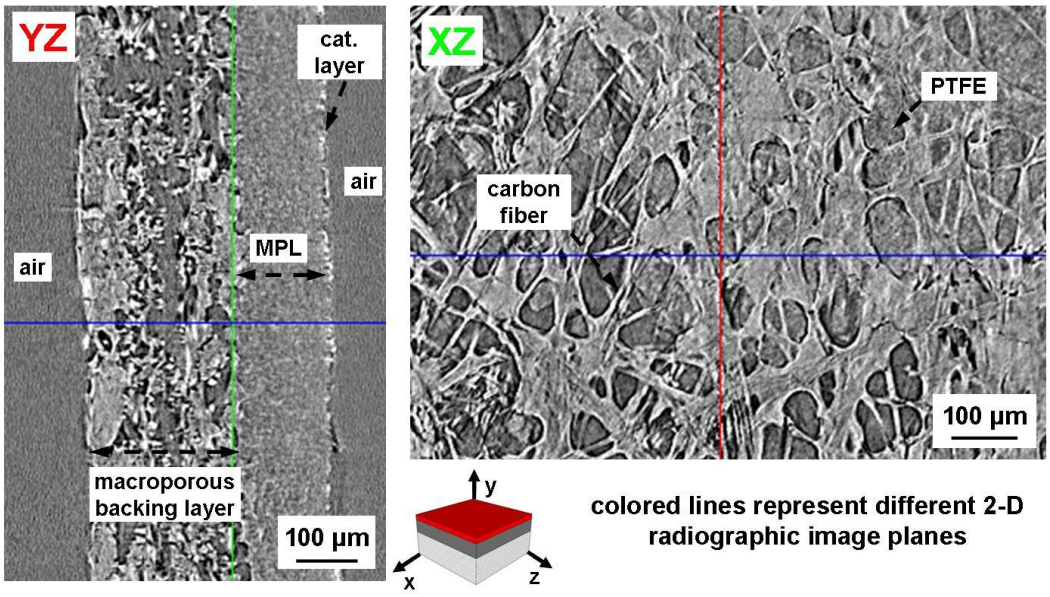

Figure 5.3. Representative 2-D images of an aged EFCG "S" Type electrode with a hand-painted Pt/C catalyst layer. The YZ plane image is 503/1004 and the XZ plane image is 513/1024. The X-ray source was at 60 kV and 100 µA. The magnification is 10x and a resolution of 1 pixel = 1.317 µm.

Using the Xradia reconstruction software, which accompanies the MicroCT hardware, an experimentally-aged EFCG "S" Type electrode (E-TEK) with a hand-painted Pt/C catalyst layer is imaged (discussed in section 5.3.5). Figure 5.3 shows through-plane (YZ) and in-plane (XZ) 2-D radiographic images of the GDE in with a component labeled. The colored lines on the images represented the planes, such that the red line is the YZ plane, the green line is the XZ plane, and the blue line is the XY plane (not shown). In addition to provide through-plane information such as comparative layer thicknesses, these images also enable the non-destructive analysis of internal interfaces within the GDE structure. For example, the XZ plane image shown in Figure 5.3 is at the interface between the macroporous carbon fiber backing layer and the hydrophobic microporous layer (MPL) of PTFE and carbon particles. Probing these internal interfaces is critical as they govern water management within the GDE structure.

In addition to these 2-D images, a 3-D virtual model of the GDE can be generated (Figure 5.4). This tomographic image enables qualitative visualization of internal architecture and organization of the GDE. Several initial observations can be made when viewing these MicroCT

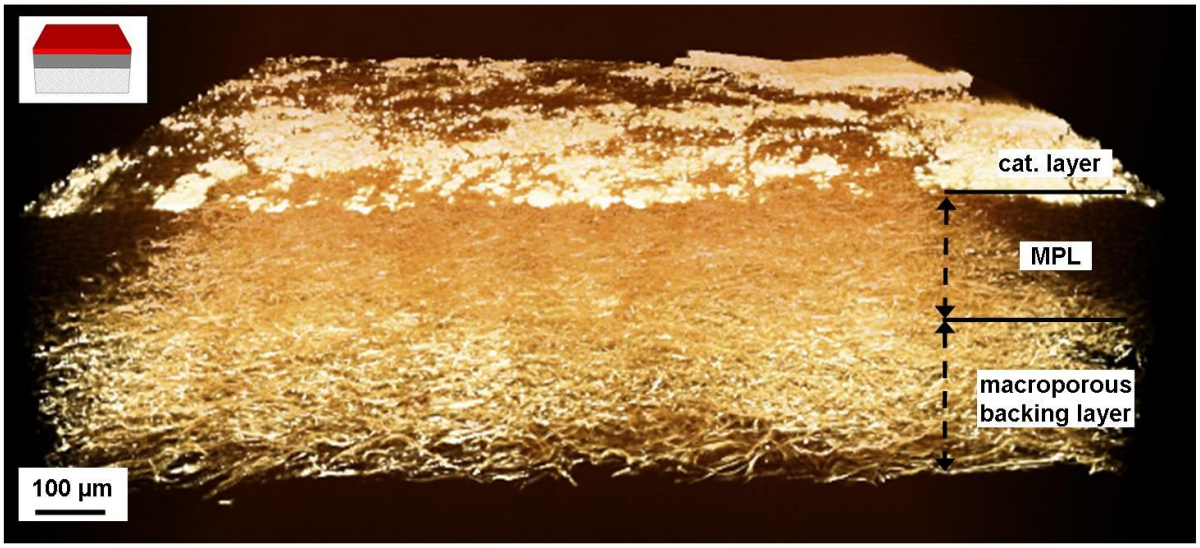

Figure 5.4. 3-D rendering of an aged EFCG "S" Type electrode with a hand-painted Pt/C catalyst layer (with false color). The X-ray tube was at 60 kV and 100 µA. The magnification is 10x and a resolution of 1 pixel = 1.317 µm and 1 voxel = 2.284 μm^3. The scale bar represents the image foreground.

images of the GDE. First, the macroporous backing layer has complex internal architecture and makes up a significant fraction of the electrode volume. This layer consists of PTFE-treated carbon fibers that govern the distribution and delivery of gaseous reactants to and by-products from the catalytic surface. The fiber distribution in this layer appears non-uniform and appears denser towards the outside and less dense in the middle. Second, the MPL appear to have little internal structure on the micro-scale. Furthermore, X-ray absorption in the MPL is very low, almost indistinguishable from air, due to the uniformity of the PTFE and carbon particle mixture. Third, the hand-painted catalyst layer appears non-uniformly distributed on the electrode surface which leads to poor catalyst utilization and lowered performances.

5.3.3 Observation of Catalyst Layer Distribution using MicroCT imaging

Figure 5.5 shows the general non-uniformity of catalyst distribution on a typical GDE with a hand-painted catalyst layer. Note that while GDE pictured is not the exact sample used for

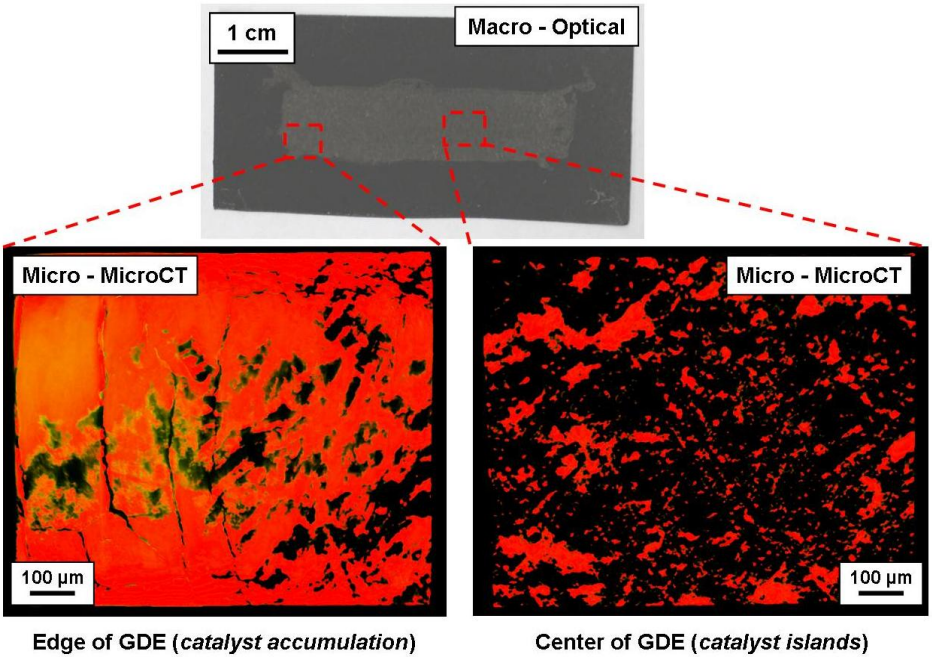

Figure 5.5. Representative image of metallic catalyst layer non-uniformity on a hand-painted GDE (with false color). The X-ray tube was between 44 - 45 kV and 60 - 66 µA. The magnification is 20x and a resolution of 1 pixel = 1.078 µm.

MicroCT analysis, it is identically prepared and thus suitable for a qualitative representation. The variations in catalyst distribution at different points on the GDE surface are due to the hand-painting technique. After catalyst inks are sonicated, a paint brush is used to spread the catalyst ink onto the hydrophobic MPL surface. While catalyst distribution appears uniform on the macro-scale, significant variability exists on the micro-scale. First, towards the edge of the catalyst layer, particles tend to accumulate whereas in the middle of the GDE less catalyst tends to deposit. This is due uneven catalyst ink distribution which is pushed from the GDE center towards the corner via the paint brush strokes. Thus, more catalyst can accumulate and slowly deposit at the edges and corners of the catalyst layer. Second, the distribution of catalyst islands in the middle of the GDE is non-uniform indicating variability in catalyst deposition from the paint brush even under similar conditions. These observations suggest that hand-painting, a widely-employed catalyst deposition technique in both academic and industrial laboratories for small-scale fuel cell experiments, may not be as uniform as optically perceived.

Uneven catalyst distribution on the electrode is a significant concern as critical fuel cell performance metrics (*e.g.*, volumetric activity for Pt-free catalysts

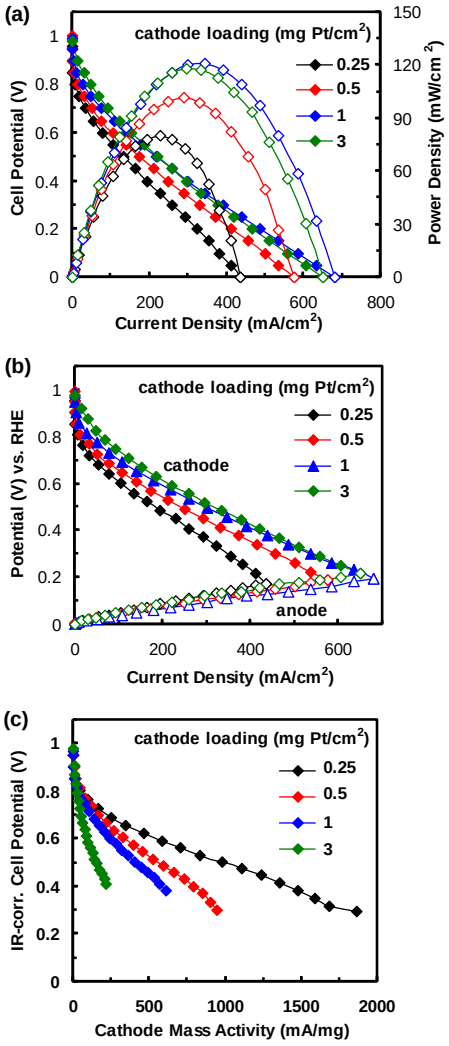

Figure 5.6. Acidic microfluidic H_2/O_2 performance as a function of cathode catalyst loading (in mg Pt/cm^2). **(a)** Polarization & power density curves, **(b)** individual electrode plots, and **(c)** cathode mass activity. Anode is 3 mg Pt/cm^2. Studies are performed at room temperature with 50 sccm H_2/O_2 gas flows and 0.5 M H_2SO_4 at 0.3 mL/min.

[41]) are based on the assumption of uniform layers. For example, Figure 5.6 shows the performance of an acidic microfluidic H_2/O_2 fuel cell operated with different cathode catalyst loadings (0.25, 0.5, 1, and 3 mg Pt/cm^2). As shown in Figures 5.6a and 5.6b fuel cell cell performance plateaus at a cathode loading of 1 mg Pt/cm^2 with a significantly higher cathode loading (3 mg Pt/cm^2) actually leading to a slight reducing in performance. However, the cathode mass activity of the fuel cell with a 1 mg Pt/cm^2 loading is lower than the fuel cell with 0.25 and 0.5 mg Pt/cm^2 loadings (Figure 5.6c) due to less efficient use of catalyst. As previously mentioned, reducing Pt content in acidic fuel cell cathodes,without sacrificing performance is a critical step towards improving the commercial viability of fuel cell technologies. This requires balancing catalyst utilization with absolute cathode performance. However, non-uniform catalyst layer distribution leads to lower than expected electrode performance, as the nominal catalyst loading (amount in catalyst ink), the actual catalyst loading (amount deposited on the electrode) and the utilized catalyst loadings (amount exposed to electrolyte / membrane) may be very different. Thus, further reduction in catalyst loading may be possible via the use of more efficient and uniform deposition strategies. For example, catalyst inks could be vacuum-filtered and deposited onto the GDL via transfer printing. Qualitative MicroCT imaging is a useful tool for such deposition analyses.

5.3.4 A Quantitative Analytical Method for GDE Macroporous Layers

While qualitative visualization of MicroCT images provides useful information about electrode architecture and catalyst layer distribution, the quantitative determination of critical parameters (*e.g.*, local porosity, uniformity of layer thicknesses) is necessary to understand the extent of physical changes in electrode structure and to correlate those transformations to variations in electrode performance. This requires the development of robust analytical

protocols. While simpler analyses, such as multi-point thickness measurements (described in section 5.2.4), can be performed using the Xradia software, more detailed analyses, such as porosity measurements, require the use of more sophisticated computational programs. Thus, methodology development and quantitative analysis are performed using Amira software package (Version 5.3, Visage Imaging) on a high-performance computer workstation.

First, properties of the macroporous layer are investigated with a focus on determining both bulk and local porosities. Figure 5.7 shows a representative gray-scale orthogonal slice (orthoslice) of the EFCG "S" type electrode with a bounding box around the area of analytical interest, the macroporous layer (TGP-H-120). As shown, this bounding box is applied to every orthoslice in the image stack, effectively "cropping" each 2D image to form the volume of interest. For quantitative analysis, each grayscale image in the MicroCT stack must be converted, via segmentation, into a binary image to identify voxels (volumetric pixels) of material and void space. In MicroCT literature, image thresholding is the most common segmentation method [17,29,32-34,37]. This process is non-trivial as typical images do not contain well defined minima and maxima, from which a threshold value can be intuitively defined [17]. Furthermore, the choice of thresholding cutoff values can significantly impact the reported porosity, with variations up to 0.43% per gray-scale value [33]. Thus segmentation is often aided by a series of

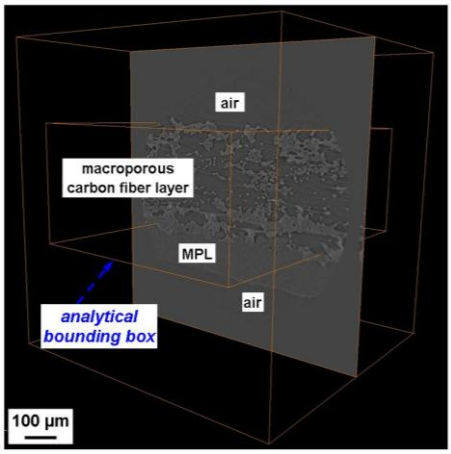

Figure 5.7. Representative 2D orthogonal slice (orthoslice) within a 3D stack with an analytical that captures the macroporous layer volume. Sample is a fresh EFCG "S" Type electrode. The resolution is 1 pixel = 1.078 µm and 1 voxel = 1.252 μm^3.

median filters [29], calibration to previously-determined MIP values, or independent statistical methods (*i.e.*, Otsu's method) [17].

For these analyses, two segmentation techniques are explored: thresholding at a certain gray-scale value and filament tracing. In the thresholding method, a single gray-scale range is chosen for the porous layer volume that attempts to account for all of material without capturing excessive void space. In the filament tracing method, first connected fibers are selected in a single orthoslice using a semi-automated selection tools (*e.g.*, edge detection, threshold masking). These fibers are then automatically traced throughout the entire porous layer volume such that only connected volumes, within the gray-scale range, are captured. Porosity is defined by the following equation:

$$\varepsilon = 1 - \frac{\text{material}_{vox}}{\text{total}_{vox}} = 1 - \frac{\text{material}_{vox}}{\text{material}_{vox} + \text{void}_{vox}} \tag{5.8}$$

Where material_{vox} is the number of materials voxels which are carbon fibers, binder, PTFE (all of which are assumed to be impermeable) and void_{vox} is the number of void voxels. The results of the two segmentation methods are shown in Figure 5.8. The porosities were determined be 76.2% and 70.0% for the thresholding and filament segmentation methods, respectively (Figure

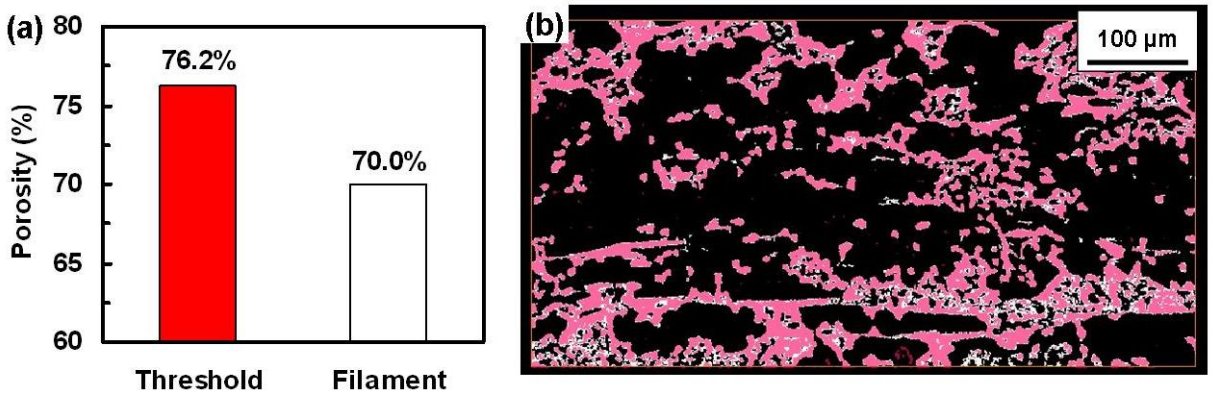

Figure 5.8. **(a)** Comparative porosity analysis for the macroporous layer volume for the thresholding (red) and filament tracing (white) segmentation methods. **(b)** A representative orthoslice with these two segmentation methods overlaid. The pink areas represent overlap the segmentation methods, the black areas represent void space. The resolution is 1 pixel = 1.078 µm and 1 voxel = 1.252 μm^3.

5.8a). In Figure 5.8b, the effectiveness of the two methods can be compared by overlaying the thresholding method values (red) on an orthoslice generated using the filament method values (white). The pink and black areas represent method overlap and void space, respectively. The values obtained by thresholding method appear less accurate than those obtained by the filament tracing method as image noise, due to polychromatic beam, is difficult to completely filter out. Consequently, common gray-scale values may be found in the fibrous masses and also in the void space (particularly close to fiber samples). Because the filament tracing utilizes structural connectivity and a grey-scale threshold range, rather than range alone, the method can better differentiate fibrous masses from void space leading to a more accurate estimate. The accuracy of the filament tracing segmentation method is further verified by a side-by-side comparison of the gray-scale orthoslice (left) and the same gray-scale orthoslice with the segmentation values overlaid (Figure 5.9).

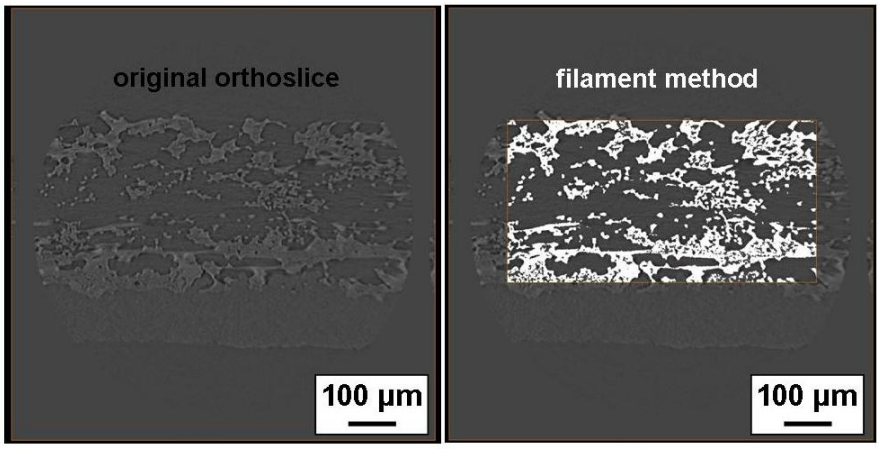

Figure 5.9. Side-by-side comparison of orthoslice of the raw gray-scale MicroCT data and the results of filament tracing based segmentation overlaid on that original orthoslice. The resolution is 1 pixel = 1.078 µm and 1 voxel = 1.252 μm^3.

The bulk porosity value obtained by this filament tracing method are comparable to other values reported in literature using different measurement techniques (Table 5.1) [13,17,42,43]. The EFCG "S" type electrode utilizes a Toray TGP-H-120 carbon paper which is PTFE-treated

to increase hydrophobicity (between 10 - 60 wt%). The specimen investigated here is believed to have 20 wt% PTFE. Increasing the PTFE content decreases the porosity [16] thus the values obtained in the present investigation are lower than those obtained by Fishman *et al.* who used a similar MicroCT-based technique to analyze untreated TGP-H-120 carbon paper [17].

Table 5.1. Reported literature on bulk porosities of Toray TGP-H-120 carbon paper (with and without PTFE) using different measurement techniques.

Gas Diffusion Material	Porosity (%)	Measurement Technique	Author
Toray TGP-H -120 (no PTFE content)	78	unknown	Manufacturer's Spec. sheet [41]
Toray TGP-H -120 (no PTFE content)	78.7	MicroCT	Fishman *et al.* [17]
Toray TGP-H -120 20 wt% PTFE	70.5	Weight per unit area & uncompressed thickness	Lin *et al.* [13]
Toray TGP-H -120 (unknown PTFE wt%) (1)	75.6 (75.9)	Weighing (Porosimetry)	Williams *et al.* [42]
EFCG carbon paper (unknown PTFE wt%) (2)	75.8 (73.8)		
Toray TGP-H-120 as part of EFCG carbon paper (~20 PTFE wt%)	70.6 ± 0.9	MicroCT Proc #1	this work

(1) Toray carbon paper is simply described as 'bare' which may mean either no MPL and/or no PTFE content
(2) According to E-Tek specification, EFCG carbon paper have 10 - 60 wt% PTFE.

As compared to these other techniques, the advantage of MicroCT analyses is that local pore distribution within the macroporous carbon fiber layer can be identified and quantified. The local porosity distribution while the macroporous layer is analyzed by dividing the segmented volume into a number of slices and computing porosity of each slice. The overall porosity distribution can then be compared on a normalized scale. While a certain minimal number of segmentation slices are required to accurately capture local trends, generating too many slices is computationally expensive. Initially pore distribution is characterized in the through-plane direction (y-axis) which is the primary direction of gas and liquid transport in the fuel cell

electrode. Figure 5.10 shows the pore distribution as a function of the number of segmentation slices (1, 5, 10, 20, and 40 segments). The bulk porosity is used for the single segment line. Figure 5.10 shows a spike in porosity (~93%) towards the center of the layer suggesting the TGP-H-120 layer was constructed pressing two thinner carbon layers together via ply molding manufacturing. Similar observations have been reported by others [17]. This region of increased porosity is more hydrophilic than the rest of the porous layer structure due to the lack of PTFE-treated fibers. Thus, this volume may be a location where liquid water can accumulate during fuel cell operation under flooding conditions (*e.g.*, higher current densities). The porosity drops at the corner edges due to the uneven distribution of PTFE throughout the sample including the formation of a PTFE "skin" on the backing layer outer edges which has been reported by Fluckiger *et al.* [16] and independently observed via SEM analysis (not shown). The porosity increase observed at zero for the higher numbers of segmentation slices (*i.e.*, 20, 40 segments) can be attributed to a slightly oversized bounding box. Thus, 10 segment slices appears to be the sufficient for surveying the porous layer for local trends. If areas of interest are identified then finer analyses (more segments) can be used.

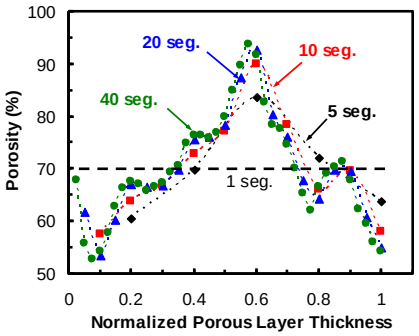

Figure 5.10. Through-plane (y-direction) porosity of a carbon fiber layer as a function of segmentation (1, 5, 10, 20, and 40 slices). The normalized zero is on the GDE side where gas enters.

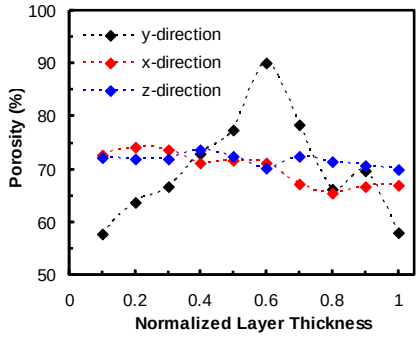

Figure 5.11. Through-plane (y-direction) and in-plane (x- and z-directions) porosity in a carbon fiber layer. 10 segments are used to normalize the contributions of each plane.

Figure 5.11 shows the porosity distribution in through-plane (y-direction) and the in-planes (x- and z- directions). The in-plane porosity of the TGP-H-120 layers varies

slightly as compared to the through-plane porosity indicating the anisotropy of the carbon paper. Similar results were reported by Fishman *et al.* [17].

5.3.5 Initial Structure-Activity Correlations of Alkaline Fuel Cell Electrodes

Now that quantitative protocols have been developed for MicroCT analyses of porous layer structure, these techniques are applied to fuel cell electrodes to probe what physical changes accompany shifts in electrochemical performance. First, beginning-of-life (BOL) and end-of-life (EOL) structural analyses are performed on alkaline fuel cell electrodes (described in Chapter 3). BOL structural studies are performed on fresh HP and non-HP E-Tek GDLs (with no catalyst layer). EOL structural studies are performed on the E-Tek GDEs which were used in the Chapter 3. Changes in porous layer thickness and porosity are quantified as a function of hot-pressing and aging. The results of these measurements are summarized in Tables 5.2 and 5.3.

Table 5.2. Electrode macroporous layer thickness as a function of hot-pressing and aging (through extensive experimental use), respectively. Multiple measurements are taken at different points across the electrode structure. An outlier analysis technique was employed (detailed in section 5.2.4). The layer is a PTFE-treated Toray TGP-H-120 in an EFCG "S" type electrode.

GDE State	Porous Layer Thickness (μm)		
	Non-HP	HP	Difference
Fresh (1)	357.6 ± 20.5	334.1 ± 14.7	23.5 ± 25.2
Aged (2)	235.3 ± 25.1	224.9 ± 25.8	10.4 ± 36.0
Difference	122.3 ± 32.4	109.2 ± 29.7	--

(1) N = 49 for thickness, (2) N = 128 for thickness

Table 5.3. Electrode macroporous layer porosity as a function of hot-pressing and aging (through experimental extensive use), respectively. Bulk porosity values are determined by analyzing MicroCT images using Amira software. The layer is a PTFE-treated Toray TGP-H-120 in an EFCG "S" type electrode.

GDE State	Bulk Porosity (%)		
	Non-HP	HP	Difference
Fresh (1)	70.6 ± 0.9	69.9 ± 0.0	0.7 ± 0.9
Aged (2)	67.8 ± 0.0	64.9 ± 0.0	2.9 ± 0
Difference	2.8 ± 0.9	5.0 ± 0.0	--

(1) N = 3 for porosity, (2) N = 3 for porosity

The thicknesses and porosity of the original uncompressed GDL are very similar to values reported in literature [13,17]. While, hot-pressing the GDE (at 340 psi) seems only slightly reduce both the porous layer thickness and bulk porosity, this reduction is important in high current density regimes (see Figure 3.5). Small shifts in pore distribution within the macroporous layer may alter the hydrophobicity and hydrophilicity of local regions, particularly at the interface between the GDL and the gas flow channel, which could alter environment enough to induce flooding under higher current density regimes. Systematic analyses of hot-pressing on local electrode structure and electrochemical performance are on-going.

Prolonged use of electrodes under alkaline fuel cell operating conditions leads to significant reductions in both porous layer thickness and bulk porosity. Table 2 shows ~30% decrease in porous layer thickness for both non-HP and HP GDEs. The decrease in thickness can be correlated to mechanical degradation (due extended compression in the fuel cell) [2]. Structure

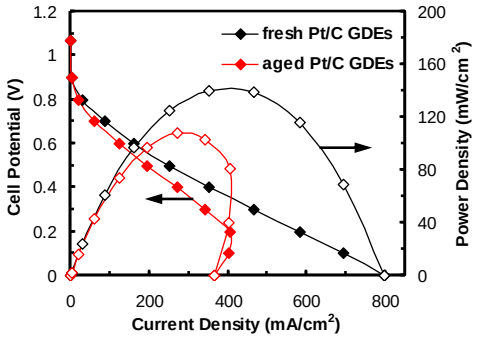

Figure 5.12. Effects of prolonged fuel cell operation under alkaline conditions. **(a)** Polarization and power density curves for fuel cells operated with fresh (*near* BOL) and aged (EOL) GDEs. Studies were performed at room temperature with 50 sccm H_2/O_2 flow rates and 3 M KOH at 0.3 mL/min.

shifts can also be correlated to losses in hydrophobicity due to PTFE degradation which may weaken the GDE architecture [15]. Table 5.3 shows that the porous compression is accompanied by a ~3-5% decrease in bulk porosity for both non-HP and HP GDEs. Figure 5.12 shows the alkaline microfluidic H_2/O_2 fuel cell performance as a function of electrode aging. Significant performance losses are observed particularly at higher current densities where anode flooding was observed (see section 3.3.7). Even when aged, non-HP anodes always outperformed HP anodes. This observation correlates with the observed difference in porosity between the aged HP GDE than in the aged non-HP GDE. Thus, these preliminary structure-activity analyses suggest that in liquid electrolyte-based AFCs: (*i*) electrode performance reductions can be attributed to significant decreases in macroporous layer thickness and bulk porosity and (*ii*) while hot-pressing does not lead to significant shifts in total thickness or porosity, slight shifts may alter the hydrophobicity and hydrophilicity of local regions within the GDE (a suggested area of future research).

5.3.6 Systematic Structure-Activity Analyses of Acidic Fuel Cell Cathodes

Beyond beginning and end-of-life studies, MicroCT imaging and microfluidic fuel cell analyses can be coupled to characterize the impact of compression on electrode structure and performance during the working lifetime of the component. As detailed in section 3.3.2, electrodes within operating fuel cell systems are often subjected to over-compression and uneven pressure distribution, which can damage the intricate electrode microstructure leading to losses in porosity and hydrophobicity and, consequently, to reductions in performance and durability [2,14,44,45]. Though an important area of research, to date, only a few literature papers have been published on the effects of this mechanical compression on electrode performance [2]. Combined MicroCT imaging and fuel cell analyses can be used to systematically probe the

impact of compression, in the form of hot-pressing, on the physical structure and electrochemical performance of GDEs.

In all previous studies, a sample was *cut from* the GDE and characterized in the MicroCT (Figure 5.2a). However, this preparation procedure is destructive and, thus, does not allow for analyses of the same electrode under multiple experimental conditions (*i.e.*, different pressures). Thus, a second method is employed were the *whole* GDE is clamped in a rotating stand such that only a small corner is exposed to the X-ray beam between the source and the collector within the MicroCT (Figure 5.2b). This enables multiple *ex-situ* analyses of the same electrode area over a range of experimental conditions. Note that only GDE corners can be analyzed using this method, thus the catalyst layer, which is towards the center of GDE (see Figure 5.5) cannot be studied.

The effects of hot-pressing on the performance of an acidic fuel cell cathode are probed using combined MicroCT and microfluidic fuel cell studies. As detailed in earlier chapters, the cathode performance typically limits overall acidic fuel cell performance due to sluggish oxygen reduction reaction (ORR) kinetics and insufficient removal of water, generated by the ORR, which leads to flooding. Thus cathode performance is dependent on the ability of the electrode to efficiently deliver oxygen to the catalyst sites and remove formed water from the porous

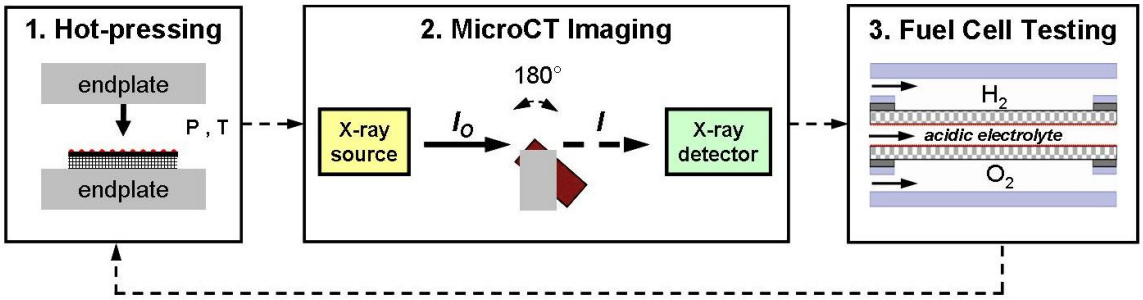

Figure 5.13. Experimental protocol for studying the relationship between the physical structure (via MicroCT imaging) and electrochemical performance (via fuel cell testing) of acidic cathodes as a function of compression. For all hot-pressing studies the temperature is 125 ± 10°C. Fuel cell studies are performed at room temperature with 10 sccm H_2/O_2 and 1.0 M $HClO_4$ flowing at 0.6 mL/min.

structure. The effects of mechanical compression of these abilities are probed using the experimental protocol shown in Figure 5.13. Electrodes are investigated at 0, 1000, 2000, 5000, and 10000 lbs_f. In all hot-pressing studies, the platen temperatures are 125 ± 10°C. Fresh electrodes (0 lbs_f) are first analyzed via MicroCT and then characterized via fuel cell testing. Analyses are performed on E-TEK PAFC cathodes with hand-painted Pt/C catalyst layers (3 mg Pt/C/cm^2, 50 wt% Pt). Like the EFCG "S" Type electrode, the macroporous layer is PTFE-treated TGP-H-120. The total electrode surface area is ~12 cm^2 (6 (L) x 2 (W) cm^2). For comparison, the hot-pressed electrodes described earlier chapters were subjected to ~340 psi which is ~650 lbs_f (for a 12 cm^2 GDE).

The effects of hot-pressing the physical structure of the cathode are shown in Figure 5.14. Figure 5.14a shows multi-point thickness measurements of the total GDE and the individual layers as a function of hot-pressing pressure. For each point, 72 measures are taken across the electrode. The outlier analysis method is described in section 5.2.4. Initially, at low compression (1000 lbs_f), the reduction in total GDE thickness is primarily due to the microporous layer of teflonized carbon compacting into the macroporous layer of carbon fibers. At 2000 lbs_f, both the micro- and macroporous layer compress. Between 2000 and 5000 lbs_f, macroporous layer compresses significantly whereas the microporous layer plateaus. Above 5000 lbs_f total electrode thicknesses appears to approach a minimum

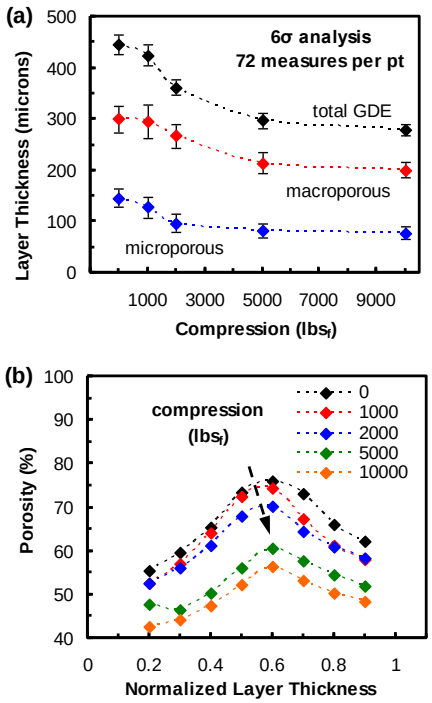

Figure 5.14. Effects of hot-pressing pressure on electrode structure. **(a)** Multi-point measurements of total GDE and individual layer thicknesses. **(b)** Local through-plane porosity in the macroporous layer. Outlier analyses are performed on the thickness measurements.

value below which is cannot easily compact further. At this point, macroporous layer is more like a solid layer than a porous network (not shown). Further reductions in thickness would require crushing of the carbon fibers. Figure 5.14b shows the shifts in local through-plane porosity as a function of hot-pressing pressure. The normalized zero is on the GDE side where gas enters. Like the EFCG "S" type electrode, the porosity peaks towards the center of the layer. This, again, suggests that the TGP-H-120 layer is constructed of two thinner layers. Initially, at low compression (1000 lbs_f), the porosity distribution shifts and reduces slightly as the microporous layer compacts in the macroporous layer. Note that the segmentation method can distinguish between the carbon fibers and teflonized carbon particles. Between 1000 and 5000 lbs_f, the porosity distribution remains constant but reduces significantly. Above 5000 lbs_f the porosity, like the GDE thicknesses, appears to approach a minimum value below which is cannot easily reduce further.

The effects of hot-pressing the electrochemical performance of the cathode within an acidic fuel cell are shown in Figure 5.15. Figure 5.15a shows fuel cell polarization curves as a function of hot-pressing pressure. As compression increases the overall fuel cell performance decreases. The corresponding individual electrode polarization curves show that the changes in overall fuel cell performance can be attributed to the decreases in cathode performance (Figure 5.15b). The anode is not compressed. In general, as the cathode

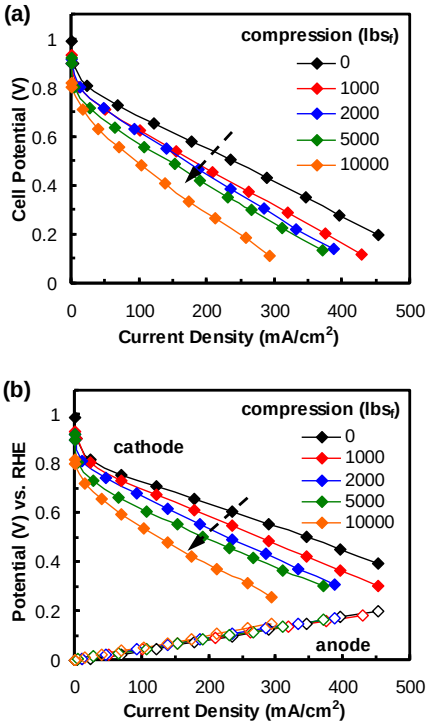

Figure 5.15. Effects of hot-pressing pressure on cathode performance. **(a)** Polarization curves and **(b)** individual electrode plots. Both electrodes have 3 mg Pt/C/cm^2. Studies are performed at RT with 10 sccm H_2/O_2 gas flows and 1.0 M $HClO_4$ at 0.6 mL/min.

compresses, the onset potentials decrease and ohmic losses increase. Thus losses can be attributed to reduced reactant transport to the catalyst layer and, to a lesser extent, to damaged carbon fiber connectivity (higher resistivity). Mass transport losses were not observed, likely due to the lower current density regimes. To probe these effects, further studies should be performed at high current densities (*e.g.,* increased electrolyte concentration, reduced electrode-to-electrode distance) and/or for longer durations. Furthermore, the results show the electrode performance directly after hot-pressing. Interestingly, the cathode performance gradually improves though never returns to the original state, in terms of power output (not shown). These shifts may be attributed to the formation of new hydrophobic and hydrophilic pathways throughout the electrode structure which enables increasingly efficient water management and thus improved performance. Developing a deeper understanding of formation of these transport pathways within compressed porous structures is, again, a suggested area of future research (*e.g.,* length of required fuel cell start-up and break-in).

Figure 5.16 shows an initial comparison between cathode porosity, obtained via MicroCT imaging, and fuel cell performance as a function of hot-pressing pressure. In general, as cathode porosity decreases so does fuel cell performance. At higher compressions ($\geq$ 2000 lbs_f), shifts in cathode porosity correlate well with changes in electrode performance. However, at lower compressions (*i.e.,* 1000 lbs_f) deviations occur as the fuel cell peak power appears to be very sensitive to even slight compression. At these low compressions, shifts in microporous and catalyst layer structure, both not captured in Figure 5.16, are likely responsible for the reductions

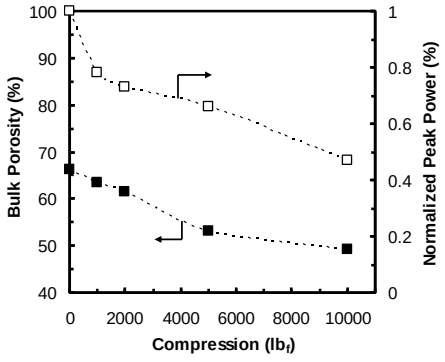

Figure 5.16. Bulk cathode porosity and normalized acidic fuel cell peak power as a function of compression.

in electrode performance. Investigations of these changes via coupled structural (MicroCT, SEM, XRF…) and electrochemical studies are on-going.

5.4 Conclusions

Microfluidic H_2/O_2 fuel cells with flowing pH-flexible electrolytes are versatile electro-analytical platforms for investigating individual catalyst and electrode performance characteristics over a range of fuel cell operating conditions. However, even though these studies can provide detailed electrochemical information, the relationship between *in-situ* electrode performance and the physical properties of these materials remains poorly understood. A comprehensive analysis of structural changes must employ visualization methods that can determine shifts in complex internal architectures as well as distinguish between different species. MicroCT imaging techniques enable multi-scale high-resolution 3D visualizations of electrode architectures. With the development and validation of quantitative analytical protocols, combined electrochemical and structural studies can now be performed using microfluidic fuel cells and MicroCT imaging. In a preliminary demonstration shifts in AFC electrode performance as a function of hot-pressing and prolonged exposure to alkaline electrolytes have been correlated to changes in electrode structure and porosity. In further initial studies, the effects of compression on the structure and performance of acidic fuel cell cathodes is systematically characterized. Further detailed studies on (*i*) the quantitative relationship between catalyst layer distribution and electrode performance and (*ii*) on the effects of PTFE degradation on the structure, hydrophobicity, and performance of alkaline fuel cell electrodes are on-going.

All studies reported in this chapter have focused on combining *ex-situ* structural analysis with *in-situ* electrode performance. While these investigations provide critical information that

may guide the development of novel components and improved fabrication techniques (*e.g.*, catalyst deposition); looking ahead, opportunities exist to develop microfluidic platforms for simultaneous MicroCT and fuel cell analyses. The X-ray beam used for MicroCT imaging (*i*) does not affect the electrical operation of the fuel cell, (*ii*) is sensitive to water formation in the electrode structure, (*iii*) is sensitive to electrolyte solution (*i.e.*, KOH) which are similar to image contrasting agents. Thus such combined systems may be probe transient effects in fuel cell systems such as the effects of hydration and temperature cycles on architecture electrode-electrolyte interfaces, and the formation of depletion gradients along electrode surfaces in membraneless fuel cell systems.

5.5 References

1. Carrette, L., K.A. Friedrich, and U. Stimming, *Fuel Cells - Fundamentals and Applications.* ChemPhysChem, 2001. **1**: p. 5-39.
2. Borup, R., J. Meyers, B. Pivovar, Y.S. Kim, R. Mukundan, N. Garland, D. Myers, M. Wilson, F. Garzon, D. Wood, P. Zelenay, K. More, K. Stroh, T. Zawodzinski, J. Boncella, J.E. McGrath, M. Inaba, K. Miyatake, M. Hori, K. Ota, Z. Ogumi, S. Miyata, A. Nishikata, Z. Siroma, Y. Uchimoto, K. Yasuda, K.I. Kimijima, and N. Iwashita, *Scientific aspects of polymer electrolyte fuel cell durability and degradation.* Chemical Reviews, 2007. **107**(10): p. 3904-3951.
3. Jacoby, M., *Analytics for Fuel Cells.* Chemical & Engineering News, 2009. **87**(13): p. 39-41.
4. Dyer, C.K., *Fuel cells for portable applications.* Journal of Power Sources, 2002. **106**(1-2): p. 31-34.
5. Kucernak, A.R. and E. Toyoda, *Studying the oxygen reduction and hydrogen oxidation reactions under realistic fuel cell conditions.* Electrochemistry Communications, 2008. **10**(11): p. 1728-1731.
6. Ramasamy, R.P., E.C. Kumbur, M.M. Mench, W. Liu, D. Moore, and M. Murthy, *Investigation of macro- and micro-porous layer interaction in polymer electrolyte fuel cells.* International Journal of Hydrogen Energy, 2008. **33**(13): p. 3351-3367.
7. Hizir, F.E., S.O. Ural, E.C. Kumbur, and M.M. Mench, *Characterization of interfacial morphology in polymer electrolyte fuel cells: Micro-porous layer and catalyst layer surfaces.* Journal of Power Sources, 2010. **195**(11): p. 3463-3471.
8. Kim, S., M. Khandelwal, C. Chacko, and M.M. Mench, *Investigation of the Impact of Interfacial Delamination on Polymer Electrolyte Fuel Cell Performance.* Journal of the Electrochemical Society, 2009. **156**(1): p. B99-B108.
9. Brushett, F.R., W.P. Zhou, R.S. Jayashree, and P.J.A. Kenis, *Alkaline Microfluidic Hydrogen-Oxygen Fuel Cell as a Cathode Characterization Platform.* Journal of the Electrochemical Society, 2009. **156**(5): p. B565-B571.
10. Jayashree, R.S., M. Mitchell, D. Natarajan, L.J. Markoski, and P.J.A. Kenis, *Microfluidic Hydrogen Fuel Cell with a Liquid Electrolyte.* Langmuir, 2007. **23**(13): p. 6871-6874.
11. Cindrella, L., A.M. Kannan, J.F. Lin, K. Saminathan, Y. Ho, C.W. Lin, and J. Wertz, *Gas diffusion layer for proton exchange membrane fuel cells-A review.* Journal of Power Sources, 2009. **194**(1): p. 146-160.
12. Park, G.G., Y.J. Sohn, T.H. Yang, Y.G. Yoon, W.Y. Lee, and C.S. Kim, *Effect of PTFE contents in the gas diffusion media on the performance of PEMFC.* Journal of Power Sources, 2004. **131**(1-2): p. 182-187.

13. Lin, G.Y. and T. Van Nguyen, *Effect of thickness and hydrophobic polymer content of the gas diffusion layer on electrode flooding level in a PEMFC.* Journal of the Electrochemical Society, 2005. **152**(10): p. A1942-A1948.
14. Roshandel, R., B. Farhanieh, and E. Saievar-Iranizad, *The effects of porosity distribution variation on PEM fuel cell performance.* Renewable Energy, 2005. **30**(10): p. 1557-1572.
15. Cifrain, M. and K.V. Kordesch, *Advances, aging mechanism and lifetime in AFCs with circulating electrolytes.* Journal of Power Sources, 2004: p. 234-242.
16. Fluckiger, R., S.A. Freunberger, D. Kramer, A. Wokaun, G.G. Scherer, and F.N. Buchi, *Anisotropic, effective diffusivity of porous gas diffusion layer materials for PEFC.* Electrochimica Acta, 2008. **54**(2): p. 551-559.
17. Fishman, Z., J. Hinebaugh, and A. Bazylak, *Microscale Tomography Investigations of Heterogeneous Porosity Distributions of PEMFC GDLs.* Journal of the Electrochemical Society, 2010. **157**(11): p. B1643-B1650.
18. Rosli, M.I., D.J. Borman, D.B. Ingham, M.S. Ismail, L. Ma, and M. Pourkashanian, *Transparent PEM Fuel Cells for Direct Visualization Experiments.* Journal of Fuel Cell Science and Technology, 2010. **7**(6): p. 06015-1 - 06015-7.
19. Satija, R., D.L. Jacobson, M. Arif, and S.A. Werner, *In situ neutron imaging technique for evaluation of water management systems in operating PEM fuel cells.* Journal of Power Sources, 2004. **129**(2): p. 238-245.
20. Turhan, A., K. Heller, J.S. Brenizer, and M.M. Mench, *Quantification of liquid water accumulation and distribution in a polymer electrolyte fuel cell using neutron imaging.* Journal of Power Sources, 2006. **160**(2): p. 1195-1203.
21. Pekula, N., K. Heller, P.A. Chuang, A. Turhan, M.M. Mench, J.S. Brenizer, and K. Unlu, *Study of water distribution and transport in a polymer electrolyte fuel cell using neutron imaging.* Nuclear Instruments & Methods in Physics Research Section a-Accelerators Spectrometers Detectors and Associated Equipment, 2005. **542**(1-3): p. 134-141.
22. Hickner, M.A., N.P. Siegel, K.S. Chen, D.S. Hussey, D.L. Jacobson, and M. Arif, *In situ high-resolution neutron radiography of cross-sectional liquid water profiles in proton exchange membrane fuel cells.* Journal of the Electrochemical Society, 2008. **155**(4): p. B427-B434.
23. Dunbar, Z. and R.I. Masel, *Quantitative MRI study of water distribution during operation of a PEM fuel cell using Teflon (R) flow fields.* Journal of Power Sources, 2007. **171**(2): p. 678-687.
24. Dunbar, Z.W. and R.I. Masel, *Magnetic resonance imaging investigation of water accumulation and transport in graphite flow fields in a polymer electrolyte membrane fuel cell: Do defects control transport?* Journal of Power Sources, 2008. **182**(1): p. 76-82.
25. Wang, M.T., K.W. Feindel, S.H. Bergens, and R.E. Wasylishen, *In situ quantification of the in-plane water content in the Nafion (R) membrane of an operating polymer-electrolyte membrane fuel cell using H-1 micro-magnetic resonance imaging experiments.* Journal of Power Sources, 2010. **195**(21): p. 7316-7322.
26. Sinha, P.K., P. Halleck, and C.Y. Wang, *Quantification of liquid water saturation in a PEM fuel cell diffusion medium using x-ray microtomography.* Electrochemical and Solid State Letters, 2006. **9**(7): p. A344-A348.
27. Rama, P., Y. Liu, R. Chen, H. Ostadi, K. Jiang, X.X. Zhang, R. Fisher, and M. Jeschke, *An X-Ray Tomography Based Lattice Boltzmann Simulation Study on Gas Diffusion Layers of Polymer Electrolyte Fuel Cells.* Journal of Fuel Cell Science and Technology, 2010. **7**(3): p. 12.
28. Bazylak, A., *Liquid water visualization in PEM fuel cells: A review.* International Journal of Hydrogen Energy, 2009. **34**(9): p. 3845-3857.
29. Becker, J., R. Fluckiger, M. Reum, F.N. Buchi, F. Marone, and M. Stampanoni, *Determination of Material Properties of Gas Diffusion Layers: Experiments and Simulations Using Phase Contrast Tomographic Microscopy.* Journal of the Electrochemical Society, 2009. **156**(10): p. B1175-B1181.
30. Buchi, F.N., R. Fluckiger, D. Tehlar, F. Marone, and M. Stampanoni, *Determination of Liquid Water Distribution in Porous Transport Layers.* ECS Transactions, 2008. **16**(2): p. 587.
31. Stock, S.R., *Recent advances in X-ray microtomography applied to materials.* International Materials Reviews, 2008. **53**(3): p. 129-181.
32. Ostadi, H., P. Rama, Y. Liu, R. Chen, X. Zhang, and K. Jiang, *Nanotomography based study of gas diffusion layers.* Microelectronic Engineering, 2010. **87**(5-8): p. 1640-1642.

33. Ostadi, H., P. Rama, Y. Liu, R. Chen, X.X. Zhang, and K. Jiang, *Influence of threshold variation on determining the properties of a polymer electrolyte fuel cell gas diffusion layer in X-ray nano-tomography.* Chemical Engineering Science, 2010. **65**(6): p. 2213-2217.
34. Ostadi, H., P. Rama, Y. Liu, R. Chen, X.X. Zhang, and K. Jiang, *3D reconstruction of a gas diffusion layer and a microporous layer.* Journal of Membrane Science, 2010. **351**(1-2): p. 69-74.
35. Hinebaugh, J., Z. Fishman, and A. Bazylak, *Unstructured Pore Network Modeling with Heterogeneous PEMFC GDL Porosity Distributions.* Journal of the Electrochemical Society, 2010. **157**(11): p. B1651-B1657.
36. Stock, S.R., *MicroComputed Tomography : methodology and applications*. 2009, Boca Raton: CRC Press. 331.
37. Ostadi, H., K. Jiang, and P.D. Prewett, *Micro/nano X-ray tomography reconstruction fine-tuning using scanning electron microscope images.* Micro & Nano Letters, 2008. **3**(4): p. 106-109.
38. Sinha, P.K., P.P. Mukherjee, and C.Y. Wang, *Impact of GDL structure and wettability on water management in polymer electrolyte fuel cells.* Journal of Materials Chemistry, 2007. **17**(30): p. 3089-3103.
39. Ghouse, M., A. Alboeiz, H. Abaoud, and M. Algarni, *Preparation and evaluation of PTFE-bonded porous gas-diffusion carbon electrodes use in phosphoric-acid fuel cell applications.* Int. J. Hydrog. Energy, 1995. **20**(9): p. 727-736.
40. *Imaging Technology Group, Beckman Institute of Advanced Science & Technology, University of Illinois*. 2010 [cited 2010 October 2]; Available from: http://itg.beckman.illinois.edu/.
41. Lefevre, M., E. Proietti, F. Jaouen, and J.P. Dodelet, *Iron-Based Catalysts with Improved Oxygen Reduction Activity in Polymer Electrolyte Fuel Cells.* Science, 2009. **324**(5923): p. 71-74.
42. *Toray Industries, Inc., manufacturer specification sheet*. 2010 [cited 2010 October 4]; Available from: http://www.torayca.com/properties/en/images/report_eng09_2.html.
43. Williams, M.V., E. Begg, L. Bonville, H.R. Kunz, and J.M. Fenton, *Characterization of gas diffusion layers for PEMFC.* Journal of the Electrochemical Society, 2004. **151**(8): p. A1173-A1180.
44. Lee, W.K., C.H. Ho, J.W. Van Zee, and M. Murthy, *The effects of compression and gas diffusion layers on the performance of a PEM fuel cell.* Journal of Power Sources, 1999. **84**(1): p. 45-51.
45. Bazylak, A., D. Sinton, Z.S. Liu, and N. Djilali, *Effect of compression on liquid water transport and microstructure of PEMFC gas diffusion layers.* Journal of Power Sources, 2007. **163**(2): p. 784-792.

Chapter 6

A Vapor Feed Direct Methanol Fuel Cell with Flowing Electrolyte*

6.1 Introduction

The desire for ever-increasing capabilities and longer off-the-grid run times for portable electronics (*i.e.*, laptops, cell phones) has spurred research and development of fuel cell-based power sources, which have the potential of achieving superior energy densities than rechargeable batteries [1-4]. However, as shown in Figure 6.1, fuel cell-based power sources are significantly more complex than battery-based power sources. A rechargeable battery is a compact energy storage system where an active cation, typically lithium (Li), shuttles between two porous electrodes as a function of charging or discharging cycles. A fuel cell-based system is more like a "liquid plant" where ancillary systems (*i.e.*, pumps, internal circuitry) are required to transport reactants to and from the fuel cell unit and control system operation. In fact, fuel cell-based systems often incorporated batteries for handling transient operating conditions (*e.g.*, start-up, power fluxes). Consequently, the successful implementation of fuel cell-based power sources requires careful consideration of how operating factors may impact individual fuel cell performance *and* overall system performance. For example, while active reactant delivery improves individual cell performance, the parasitic power losses required to pump the reactants may negate these performance enhancements.

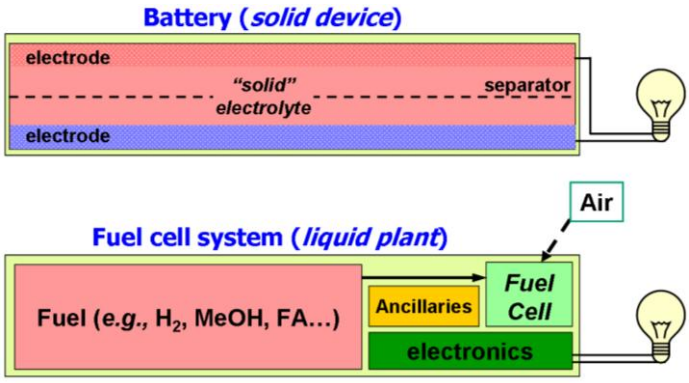

Figure 6.1. Comparative schematics of rechargeable battery- and fuel cell-based power sources.

* Part of this work has been published: F.R. Brushett, M. Mitchell, R.S. Jayashree, W.P. Zhou, and P.J.A. Kenis, *Vapor Feed Direct Methanol Fuel Cell with Flowing Electrolyte*, ECS Transactions 2007, Vol. 11(1), 1419-1424.

Moreover, designing and packaging pumping units into a fuel cell system increases device complexity which in turn hampers manufacturing. Thus, maximizing system energy density and minimizing system complexity are considered key challenges in small-scale fuel cell development.

Though hydrogen-fueled polymer electrolyte membrane-based fuel cells (PEMFCs) are most extensively developed low-temperature configurations, they have limited utility for portable applications due to safety concerns and practical challenges associated with high energy density storage of hydrogen fuel. On-board reforming of high energy density liquids to hydrogen is a possible alternative. However the required ancillary systems increase device complexity, hinder scalability, and reduce system energy density. Moreover, products of incomplete reforming (*e.g.*, carbon monoxide) may dramatically reduce fuel cell performance and lifetime. A second alternative is the use of direct liquid fuel cells which benefit from the high energy density and easy storage of organic fuels [5]. Indeed, direct methanol fuel cells (DMFCs) hold promise as power sources for next-generation portable electronics due to the low cost and high theoretical volumetric energy density (4798 Wh/L) of methanol [5]. While DMFC technologies have experienced moderate success in niche applications, *i.e.* military and telecommunications, their broad development remains hindered by several technical challenges such as fuel crossover and electrode water management (dry-out / flooding) [6,7]. Fuel crossover occurs when unreacted fuel migrates (via electro-osmosis and/or diffusion) through the membrane (or electrolyte) and reacts on the cathode causing mixed potentials, thereby reducing cell performance and efficiency [8,9]. To reduce fuel crossover, conventional DMFCs are operated at relatively low methanol concentrations (0.5 - 2 M), necessitating an ancillary system for diluting the highly concentrated or neat methanol stored in the fuel reservoir [7]. In acidic DMFCs, anode dry-out occurs while

operating at high current densities due to the osmotic drag of water molecules along with protons transported across the membrane, from the anode to the cathode. The osmotic drag, in combination with water formation, causes flooding of the cathode, which hampers oxygen transport to electrocatalytic sites. In alkaline DMFCs, these processes occur on the opposite electrodes, changing to cathode dry-out and anode flooding. Several active (*i.e.*, electro-osmotic pumps) [10,11] and passive (*i.e.*, component modification) [12] water management strategies have been proposed to overcome this limitation. Unfortunately, such strategies often require ancillary components which complicate fuel cell design and reduce overall system energy density. In addition to these performance limitations, challenges associated with system costs and durability remain [13]. However, note that, unlike the automotive market, the portable electronics market is less sensitive to high prices as the competing technology, rechargeable Li-ion batteries, is also relatively expensive [2].

To address these aforementioned challenges, extensive research efforts have been focused on developing small-scale passive DMFCs which do not utilize any auxiliary liquid pumps, gas blowers or compressors but rather rely on diffusion and natural convection for reactant delivery [7,14-40]. In general, all-passive liquid-feed DMFCs (LF-DMFCs) consist of an air-breathing cathode and a built-in liquid methanol reservoir that directly contacts with the anode. Carbon dioxide formed by the methanol oxidation reaction escapes via a selective vent in anode reservoir [41,42]. While these passive DMFCs systems have lower individual cell performance than active DMFCs, at a system-level they offer several key advantages including lower costs, reduced device complexity (enhanced durability), and increased system energy density [14]. Furthermore, passive DMFCs may self-heat due to the heat generated from the methanol oxidation and oxygen reduction reactions which, in turn, leads to enhanced cell performance [14].

However, passive transport mechanisms for reactant supply / products removal are slower and harder to control than the convection-based transport mechanisms that govern conventional active DMFCs. Indeed, a number of trade-offs exist. For example, use of higher methanol concentrations leads to increased system energy density and greater diffusive fluxes to the anode surface, which enhances cell performance. However, use of higher methanol concentrations can also lead to increased methanol crossover, which reduces fuel cell energy efficiency, and increased water management issues due to the greater reaction rates and reduced water content (*i.e.*, anode dry-out, cathode flooding). To balance these trade-offs, passive LF-DMFCs are operated with relatively dilute solutions (3 - 5 M) which lead to lower system energy densities and reduced operational lifetimes due to the rapid decrease in the preset methanol concentration [14,20,32]. Ideally, passive DMFCs systems would operate with highly-concentrated methanol to maximize system energy density but also have passive methods to increase mass-transport resistance between the fuel reservoir and the anode catalyst layer to limit crossover [7]. Several strategies have been proposed to address this challenge including modification of existing components (*e.g.*, integrated anode structures, hybrid membranes) [37,43,44], addition of novel barrier layers (*e.g.*, hydrogels, porous carbon plates) [45,46], and introduction of innovative passive control loops (*e.g.*, self-regulated fuel supply systems) [16,47]. Unfortunately, these modifications often add to device size and complexity.

Another, simpler, approach to efficiently utilizing highly-concentrated fuel is to exploit the high vapor pressure of methanol to develop passive vapor feed DMFCs (VF-DMFCs). By using natural evaporation to transport fuel to the anode, these systems can achieve high energy density and can reduce fuel crossover due to the low methanol concentration in the vapor phase. In fact, compared to LF-DMFCs, VF-DMFCs have a relatively lower methanol crossover and are more

suitable for concentrated methanol solutions or neat methanol as the feed [38]. Consequently, semi- and fully-passive VF-DMFCs, operated at near-ambient conditions and fed with concentrated methanol solutions, have begun to attract increasing attention as possible power sources for portable electronics [18,19,24-26,30,34,38]. Kim demonstrated a semi-passive VF-DMFC where pure liquid methanol was supplied to a porous foam via a syringe pump [30]. Methanol was passively vaporized through a membrane (Nafion 112) and then diffused through several barrier layers to get to anode. Water for the methanol oxidation reaction was supplied via back diffusion, from the cathode, through the membrane-electrode assembly (MEA). Compared to an identical LF-DMFC, the VF-DMFC showed 70% higher fuel efficiency (utilization) and 1.5 times higher energy density at ambient conditions. Guo and Faghri developed a novel VF-DMFC with a passive integrated thermal fluids management system where neat methanol was wicked from a fuel reservoir to a porous evaporation pad [26]. The cell was able to stably operate for 600 hrs, though it should be noted that this system employed a catalytic burner to heat the evaporation pad. Chang *et al.* developed a semi-passive VF-DMFC where neat liquid methanol was continuously fed into a reservoir via a syringe pump [18,19]. Methanol evaporates from the reservoir to the anode through a flow channel while water was supplied via back diffusion from the cathode. Eccarius *et al.* developed a fully-passive VF-DMFC where methanol vapor was generated through polydimethylsiloxane (PDMS) pervaporation membrane and evaporation rate was controlled by a solid plate with different open area ratios [24,25]. The cell performance was characterized and optimized as a function of operating conditions (*e.g.*, methanol concentration) and structural parameters (*e.g.*, gas diffusion layer (GDL) material, evaporator opening ratio, cathode structure). These VF-DMFC studies were performed at an elevated temperature (50°C) and used forced humidified air (40 sccm).

Most recently, Xu *et al.* developed and optimized a completely-passive VF-DMFC by varying the area of methanol evaporation, the distance over which the methanol vapor travels and the thickness of water management layer on the cathode [38]. A brief summary of the literature on semi-passive and passive VF-DMFCs is shown in Table 6.1. For these cell designs, the critical performance-limiting factors are determined to be water management, in particular anode dry-out, methanol crossover, and heat generation [7,24]. For example, because the configurations typically rely on back diffusion from the cathode to provide water for the anodic methanol oxidation reaction, prolonged operation under in a dry environment may not be possible.

Table 6.1. A representative literature survey of semi-passive and passive VF-DMFCs that operate at near ambient conditions and utilize highly-concentrated liquid methanol.

Reference	Anode / Cathode		Electrolyte	Max. Open Current Potential (V)	Peak Power Density (mW/cm^2)	Experimental Details
	Reactant Delivery	Catalyst				
Kim [30]	semi-passive vapor MeOH, air-breathing	8 mg PtRu/cm^2 8 mg Pt/cm^2	composite membrane	0.56	36	syringe-fed neat liq. MeOH at 0.3 mL/hr, passively-controlled MeOH evaporation, T = 38-40°C
Guo and Faghri [26]	passive liquid MeOH air-breathing	PtRu (unknown loading) Pt (unknown loading)	Nafion - 117	~0.59	16.5	neat liq. MeOH, passive thermal fluids system with catalytic burner to control evaporation
Chang et al. [18]	active liquid MeOH air-breathing	8 mg PtRu black/cm^2 8 mg Pt black/cm^2	composite membrane	~0.59	12.2	syringe-fed neat liq. MeOH at 0.4 mL/hr, passively-controlled MeOH evaporation, T = 30-36°C
Eccarius *et al.* [24]	passive vapor MeOH *active* humidified air	3 mg PtRu/cm^2 1 mg Pt/cm^2	Nafion - 117	0.55	27.5	Neat liq. MeOH, 40 sccm air flow, T = 50°C, evap. opening ratio 6.8%, segmented catalyst layer
Xu *et al.* [38]	passive vapor MeOH air-breathing	5 mg PtRu black/cm^2 5 mg Pt black /cm^2	Nafion - 117	~0.54	34	Neat liq. MeOH, T = 24-27°C, 45 - 55% RH

Note: Maximum open circuit potential and peak power density were not necessarily observed at the same operating conditions.

In prior chapters, a microfluidic H_2/O_2 fuel cell was discussed as an analytical platform for catalyst and electrode characterization and optimization. However, such microfluidic-based systems may also hold promise as a power source. Here, this possibility is explored with the development and characterization of a semi-passive VF-DMFC with a flowing liquid electrolyte instead of a polymeric membrane (Figure 6.2). For performance-enhancing purposes, the flowing electrolyte stream minimizes water and heat management concerns (*i.e.*, anode dry-out, cathode flooding, temperature fluctuations), facilitates by-product removal (*i.e.*, carbon dioxide,

unreacted methanol), and enables electrolyte flexibility (*i.e.*, composition). Furthermore, for electro-analytical purposes, the flowing electrolyte stream allows for the independent *in-situ* analyses of individual electrodes. Here, the performance of a microfluidic-based VF-DMFC is investigated as a function of structural parameters (*i.e.*, GDL materials, electrode-to-electrode distance) and operating conditions (*i.e.*, methanol concentration, pH).

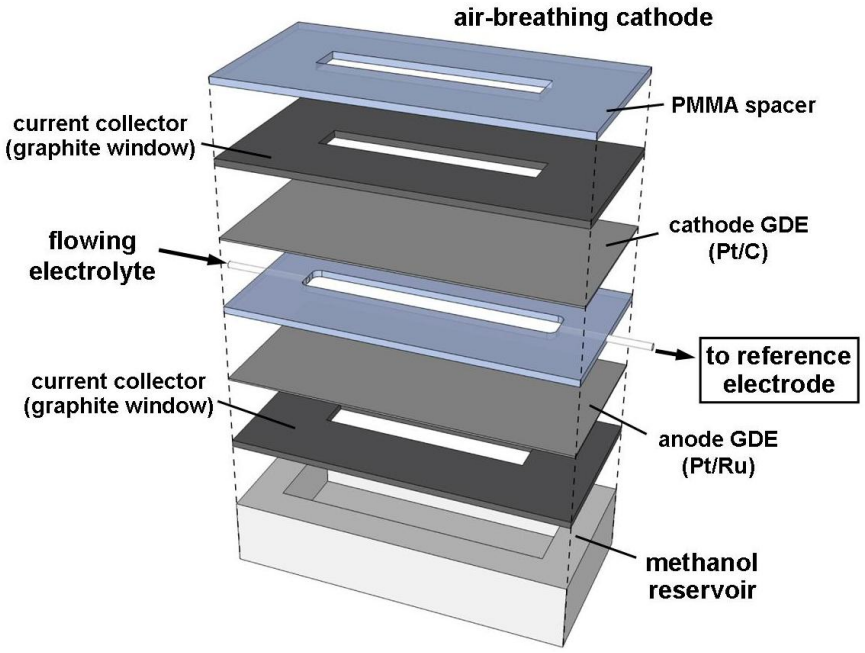

Figure 6.2. Semi-passive vapor feed direct methanol fuel cell (VF-DMFC) with a pH-flexible flowing electrolyte stream between two catalyst-coated gas diffusion electrodes (GDEs). Methanol vapor is supplied to the anode via evaporation from a liquid methanol source at the bottom of a steel reservoir. Oxygen is supplied to the cathode via diffusion from the quiescent air in the surrounding environment.

6.2 Experimental

6.2.1 Gas diffusion electrode preparation

Unless otherwise specified, the anode inks consisted of 40 mg PtRu black (Alfa Aesar, 50:50 at%) as a catalyst and 6 mg Nafion (5 wt% solution, Solution Technology) as a binder. For all studies, the cathode inks consisted of 8 mg Pt/C (E-Tek, 50 wt% Pt on Vulcan Carbon) and 0.8 mg Nafion as a binder. For all inks, 200 µL Millipore water (18.2 MΩ) and 200 µL of

isopropyl alcohol are added as carrier solvents. The catalyst inks are sonicated (Branson 3510) for at least 1 hr to ensure uniform mixing and then hand-painted onto commercial gas diffusion layers (GDLs) to create gas diffusion electrodes (GDEs). Four different GDLs are used: Sigracet 24 BC (SGL Carbon), Sigracet 35 BC (SGL Carbon), ELAT carbon cloth (E-Tek), and EFCG "S" type (E-Tek). Each GDL consists of two distinct hydrophobized layers: a macroporous carbon backing layer and a microporous carbon layer. The catalyst layer is painted on the microporous carbon coated side of all the GDLs. After application of the catalyst ink, the fabricated GDEs are hot-pressed (Carver 3851-0) at a pressure of 340 psi (~2344 kPa) and a temperature of 125 ± 10°C for 5 min. For all GDEs, the geometric surface area was 4 cm^2. Unless otherwise specified, the anode loading was 10 mg PtRu/cm^2 and 1.5 mg Nafion/cm^2. For all studies, the cathode loading was 2 mg Pt/C/cm^2 (1 mg Pt/cm^2) and 0.2 mg Nafion/cm^2.

6.2.2 Fuel cell assembly and testing

Two GDEs, anode and cathode, are mounted on opposite sides of a 0.15-cm or 0.2-cm thick poly(methyl methylacrylate) (PMMA) sheet, such that the catalyst-coated sides interface with the 3-cm long and 0.33-cm wide precision machined window in the PMMA. The window has an inlet and an outlet on either side such that the aqueous electrolyte flows between the GDEs. The 0.2-cm and 0.15-cm PMMA sheets were used for the first- and second generation VF-DMFCs, respectively. Two 0.1-cm thick graphite plates with access windows (3.8 (L) x 0.7 (W) cm^2) are placed on the outside of the GDEs and served as current collectors. On the anodic side of the assembly a stainless steel well (4.2 (L) x 1.5 (W) x 0.5 (H) cm^3) contains the liquid methanol source (1.4 mL) from which methanol evaporates and reaches the anode. For the air-breathing configuration, a second 0.15-cm thick PMMA sheet with an access window (4.4 (L) x 1 (W) cm^2) is positioned over the current collector on the cathodic side to enable oxygen to diffuse

from ambient air to the cathode. For the forced convection configuration, a polycarbonate chamber (5 (L) x 1 (W) x 0.5 (H) cm^3) was used to flow air or oxygen (laboratory grade, S. J. Smith) over the cathode at 50 sccm. In both cases, the multilayer assembly was held together with binder clips (Highmark). Prior to experimentation, the fuel cell assembly was leak tested by flowing DI water through the fluidic chamber for several minutes. In the few cases leaking was observed, typically due to misalignment of the layers, the cell was disassembled and realigned. No leaking was observed during subsequent operation.

Fuel cell experiments were conducted using either General Purpose Electrochemical Software (GPES, EcoChemie) controlled by a potentiostat (Autolab PGSTAT-30, EcoChemie) or DAQFactory Express Software (Azeotech) controlled by an in-house fabricated load box. The cell was supplied with either 0.5 M sulfuric acid (H_2SO_4, GFS Chemicals) or 1 M potassium hydroxide (KOH, Aldrich). Electrolyte flow rates were varied from 0.3 to 0.9 mL/min using a syringe pump (2200 PHD, Harvard Apparatus). The concentration of the methanol (Fisher) in the steel evaporative chamber was varied from 2.5 to 24.6 M (neat). Fuel cell polarization curves were obtained by steady-state chronoamperometric measurements at different cell potentials using a potentiostat. Potentiostat leads were attached to the anodic and cathodic graphite current collectors via copper alligator clips. The working electrode lead was attached to the anode while the reference and counter electrode leads were combined and attached to the cathode. The potentiostat was used to generate an applied potential, and a multimeter (15 XP Meterman, 87 III Fluke, or 179 Fluke), with its leads attached to the anodic and cathodic graphite current collectors, was used to determine the actual cell potential. This configuration enables the elimination of any contributions due to connect resistances between the alligator clips of the leads and the graphite current collector plates. The exposed geometric electrode surface area

(1 cm^2) was used to calculate the current and power densities. After exiting the fuel cell, the aqueous electrolyte stream was collected in a beaker with a reference electrode (Ag/AgCl in saturated NaCl, BASi). The anode and cathode polarization losses are independently characterized using two multimeters, functioning in voltmeter mode, and attached to the reference electrode and each of the graphite plate current collectors. All studies are performed at room temperature.

6.3 Results and Discussion

6.3.1 Analysis of passive vapor fuel delivery

The performance of a VF-DMFC is dependent on the continuous evaporation of methanol from the concentrated liquid source in the steel well to the anode catalyst layer. Several factors can adversely impact this evaporative flux including temperature fluctuations, caused by heat loss during vaporization, and reduced methanol concentration, caused by extended operation. Furthermore, a number of VF-DMFC configurations utilize pervaporization membranes to selectively boost the evaporative flux of methanol [24,30]. However, in this simple design, methanol and water evaporate, unassisted, from the surface of a liquid source. Thus, prior to fuel cell experiments, a brief analysis of the evaporation and mass transport of methanol to the anode is performed.

The specific vapor pressure of methanol and water is determined by the Antoine equation:

$$\log_{10} P_{vp} = A - \frac{B}{T + C} \tag{6.1}$$

In Eq. 6.1, P_{vp} represents the specific vapor pressure, T represents absolute temperature, and A, B and C represent species-specific coefficients found in the NIST Chemistry Webbook [48]. Figure 6.3 shows the specific vapor pressure of methanol and water compared to ethanol and

formic acid, two fuels of interest for direct liquid fuel cells, as a function of temperature. Both methanol and ethanol show high vapor pressure, even at room temperature, highlighting their potential as vapor feed fuels. While the vapor pressure of water is significantly lower, this is less of a concern as water for the methanol oxidation reaction is also supplied from the aqueous electrolyte stream in the present experimental configuration.

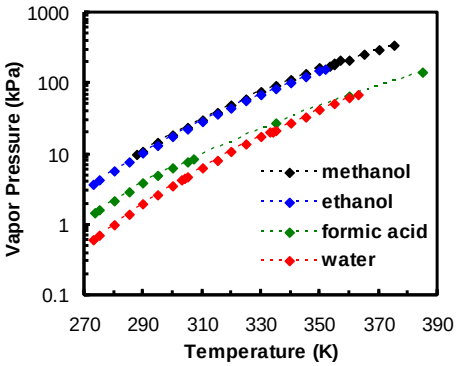

Figure 6.3. Specific vapor pressure of methanol, ethanol, formic acid, and water as a function of absolute temperature.

Further analyses are performed to determine the composition and concentration of vapor phase directly above the liquid source. For these calculations, the vapor-liquid interface is assumed to be in equilibrium and thus governed by Raoult's Law. Moreover, the interface is assumed to be a binary methanol/water system; thus, the contributions of other gaseous species (*e.g.*, air, carbon dioxide) are ignored. However, at low pressures, such as those found here, the second major assumption of the simplified Raoult's Law that the liquid behaves as an ideal solution must be abandoned. These deviations are accounted for with an activity coefficient which is a function of temperature and liquid-phase composition. Treating the interface as a low-pressure binary system, the Margules-modified Raoult's Law is as follows:

$$y_i P = x_i \gamma_i P_i^{sat} \text{ where } i = 1,2 \tag{6.2}$$

$$P = \sum x_i P_i = x_1 P_1^{sat} + x_2 P_2^{sat} = P_1^{sat} + (P_2^{sat} - P_1^{sat}) x_1 \tag{6.3}$$

$$\begin{aligned} \ln \gamma_1 &= (A_{12} + 2(A_{21} - A_{12}) x_1)(x_2)^2 \\ \ln \gamma_2 &= (A_{21} + 2(A_{12} - A_{21}) x_2)(x_1)^2 \end{aligned} \tag{6.4}$$

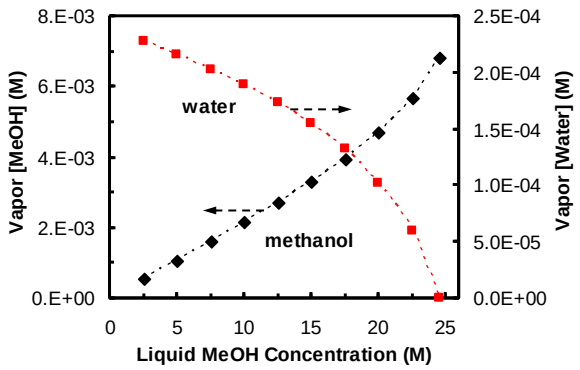

Figure 6.4. The vapor concentration of methanol (MeOH) and water at the liquid-air interface of a liquid methanol source of varying concentration.

In Eq. 6.2-6.4, x represents the liquid mole fraction, y represents the vapor mole fraction, γ represents the liquid-phase activity coefficient, P^{sat} represents the specific vapor pressure of the pure components, and P represents the total vapor pressure. The Margules coefficients A_{12} and A_{21} were 0.5533 and 0.4339, respectively [49]. The specific vapor pressures of methanol and water were determined from Eq. 6.1. Using these equations, the vapor-phase partial pressures of methanol and water were determined. The partial pressures were then converted into vapor-phase concentrations using the absolute temperature and the universal gas constant. In Figure 6.4, the resulting vapor-phase methanol and water concentrations are shown as a function of liquid-phase methanol concentrations. Promisingly, the equilibrium concentration of vaporized methanol above the liquid surface is an order-of-magnitude greater than the equilibrium concentration of vaporized water, primarily due to the higher specific vapor pressure of methanol.

As important as methanol evaporation from the liquid source is the rapid transport of that vaporized fuel to the anode surface. To determine impact of mass transport on the evaporative flux of methanol through air to the anode surface is calculated using the following equation [50]:

$$n_1 = -D\frac{dc_1}{dz} + c_1(c_1\overline{V}_1 v_1 + c_2\overline{V}_2 v_2) \tag{6.5}$$

In Eq. 6.5, n represents the total flux, D represents the diffusivity coefficient, c represents the concentration, $\overline{V}$ represents the specific volume, v represents the mass average velocity, and z represents the diffusional length. Prior to solving this general equation, several assumptions are

made. The system is assumed to behave like a concentrated solution quickly diffusing through a stagnant solvent, air. The vapor is assumed to behave as an ideal gas; therefore, the total molar concentration is constant. The vapor is assumed to react instantaneously on the anode catalytic surface; therefore, the concentration at that point approached zero. Applying these assumptions to Eq. 6.5 leads to the following equation that describes a mass-transfer limited evaporative flux:

$$n_1 = \left(\frac{DP}{lRT}\right) \ln\left(\frac{1}{1-(P^{sat}/P)}\right) \tag{6.6}$$

In Eq. 6.6, the n represents the total flux, D represents the diffusion coefficient, P represents the total pressure, l represents the diffusive length, R represents the universal gas constant, T represents the absolute temperature, and P^{sat} represents the specific vapor pressure. In this case, Eq. 6.6 is solved for the mass-transfer limited evaporative flux of methanol in air. The diffusivity coefficient of methanol in air is 0.1531 cm^2/s (at 298 K) [51]. The diffusive length is 0.2 cm. Partial vapor pressures are calculated, by solving the Margules-modified Raoult's Law (Eqs. 6.2-6.4). After solving Eq. 6.6, the evaporative fluxes are converted into limiting current densities using Faraday's coefficient and the number of electrons generated in the complete methanol oxidation reaction (6 electrons). In Figure 6.5, the limiting current densities are shown as a function of liquid methanol concentrations. Promisingly, these current densities are on the order of A/cm^2 which is an order of magnitude greater than the current densities reported in VF-DMFCs (10s to 100s mA/cm^2) [18,24,26,30,38]. Note that this calculation is based solely on the evaporative

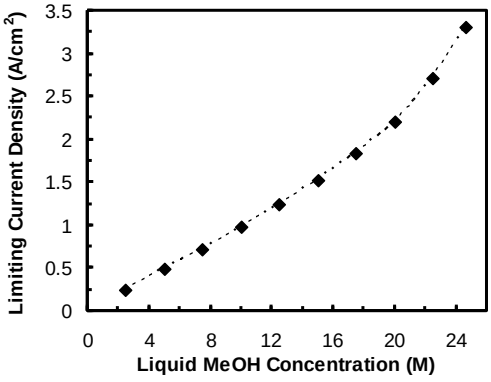

Figure 6.5. The mass-transport limited current density as a function of liquid methanol (MeOH) concentration. These values are based solely on the evaporative flux.

flux and does not account for the methanol oxidation reaction efficiency or the effects of crossover which lead to reduced fuel cell current densities. However, in general, the evaporation and diffusion of methanol appears sufficient for VF-DMFC operation to be feasible.

6.3.2 Choice of Gas Diffusion Layer Material

In all fuel cells, the choice of gas diffusion layer (GDL) is critical to performance as the material is responsible for (*i*) the transport of reactants from the flow channel to the catalyst layer, (*ii*) the drainage of liquid from the catalyst layer into either the flow channel or the membrane/electrolyte, and (*iii*) conduction of electrons with low resistance from the catalyst layer to the current collectors [52]. This choice is particularly important for passive fuel cells which rely on slower diffusive and natural convective fluxes to transport species to and from the catalyst layers. Thus, the VF-DMFC performance was first investigated and optimized using four different GDL: Sigracet 24 BC (SGL Carbon), Sigracet 35 BC (SGL Carbon), ELAT carbon cloth (E-Tek), and EFCG "S" type (E-Tek). In all experiments, the same GDL is used for both electrodes.

Prior to any electrochemical studies, each electrode set is acclimated at fuel cell operating conditions. During these acclimation sets, the fuel cell is fully assembled with 3 mL of 12.5 M liquid methanol in the reservoir and with 0.5 M H_2SO_4 flowing at 0.3 mL/min. In the first acclimation run (10 - 15 min), the cell is held at open circuit potential (OCP) until the overall fuel cell and individual electrode potentials stabilize. The OCPs of VF-DMFCs operated with Sigracet 24 BC, Sigracet 35 BC, and EFCG "S" type GDLs all stabilized after 5 min while the ELAT Carbon Cloth stabilized after 9 min (Figure 6.6a). The stable VF-DMFC OCPs were 0.41, 0.43, 0.33, and 0.33 V for Sigracet 24 BC, Sigracet 35 BC, ELAT Carbon Cloth, and EFCG "S" type GDLs, respectively. The corresponding individual electrode OCPs show that differences

both in speed of stabilization and in the stabilized OCP are due to shifts in the anode potential (Figure 6.6b). The VF-DMFCs operated with two Sigracet GDLs had lower anode potentials than cells operated with the other GDLs. This is likely because both Sigracet GDLs are thinner

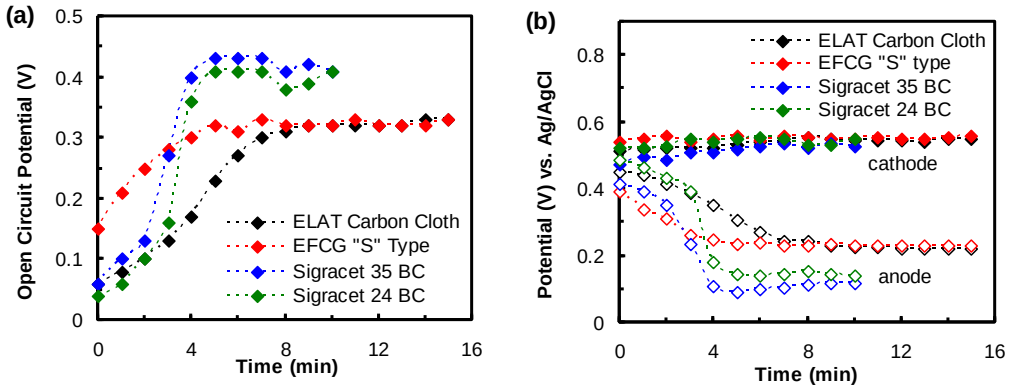

Figure 6.6. **(a)** Open circuit potential as a function of time of VF-DMFC operated with different GDLs. **(b)** The corresponding individual anode and cathode potential curves. In all studies, liquid [MeOH] = 12.5 M, the cathode is air-breathing, $[H_2SO_4]$ = 0.5 M, the electrolyte flow rate is 0.3 mL/min and experiments are performed at room temperature.

and more porous than the other GDL materials. For all GDLs, the cathode potential increased slightly before stabilizing at ~0.55 V. This indicates that (*i*) oxygen-transfer to the cathode catalyst layer is not affected by the GDL material and (*ii*) no fuel crossover is evident as the OCP remains stable for the duration of the experiments. The second acclimation test (5 - 10 min) is performed to confirm that the OCPs have indeed stabilized (not shown). In this run, all VF-DMFCs stabilized after only 1 min suggesting that the first acclimation test successfully modified the GDL materials such that the VF-DMFC response would be near-instantaneous.

Under the same fuel cell operating conditions, a number of polarization and power density curves were run to determine the VF-DMFC performance as a function of GDL material. The critical performance metrics, OCPs and peak power densities (PPDs), are shown in Table 6.2. In general, VF-DMFCs operated with the Sigracet GDLs outperformed cells operated with the other GDLs in terms of both OCPs and PPDs. The EFCG "S" type was the worst performing GDL

and does not appear suitable for VF-DMFC applications. While the ELAT Carbon Cloth GDL showed low OCPs, the cell performance improved greatly over the course of several experiments suggesting that the GDLs were further acclimating. While the Sigracet 35 BC GDL achieved the highest PPD (6.15 mW/cm^2) of all the materials, the cell performance was also highly variable which hinders reproducibility. Sigracet 24 BC GDL appears to be the best material for VF-DMFC applications as the cell demonstrates both high OCPs and PPDs with low variability. Thus, unless otherwise specified, all subsequent studies are performed on VF-DMFCs with Sigracet 24 BC-based electrodes.

Table 6.2: VF-DMFC Open circuit potential and peak power density as a function of GDL materials used. In all studies, liquid [MeOH] = 12.5 M, the cathode is air-breathing, [H_2SO_4] = 0.5 M, the electrolyte flow rate is 0.3 mL/min and experiments are performed at room temperature. Experiments are repeated 2 to 6 times for each GDL.

Gas Diffusion Layer	Open Circuit Potential (V)	Peak Power Density (mW/cm^2)
ELAT Carbon Cloth	0.33 ± 0.00	4.85 ± 0.57
E-Tek "S" Type	0.3 ± 0.04	2.87 ± 0.01
Sigracet 35 BC	0.39 ± 0.01	4.87 ± 0.95
Sigracet 24 BC	0.40 ± 0.02	5.18 ± 0.15

6.3.3 Characterization of First Generation VF-DMFC

The performance of the first-generation VF-DMFC (Gen-1 VF-DMFC) was investigated as function of methanol concentration, acidic electrolyte concentration, electrolyte flow rate, and oxidant delivery method. In Figure 6.7a, VF-DMFC performance is characterized as a function of liquid methanol concentration. A maximum OCP of 0.47 V is achieved using 2.5 M liquid methanol as the fuel. The OCP drops with increasing methanol concentrations due to increased methanol crossover which reduces the cathode potential (Figure 6.7b). The anode potential appears to decrease until a concentration of 10 M liquid methanol, above which the potential

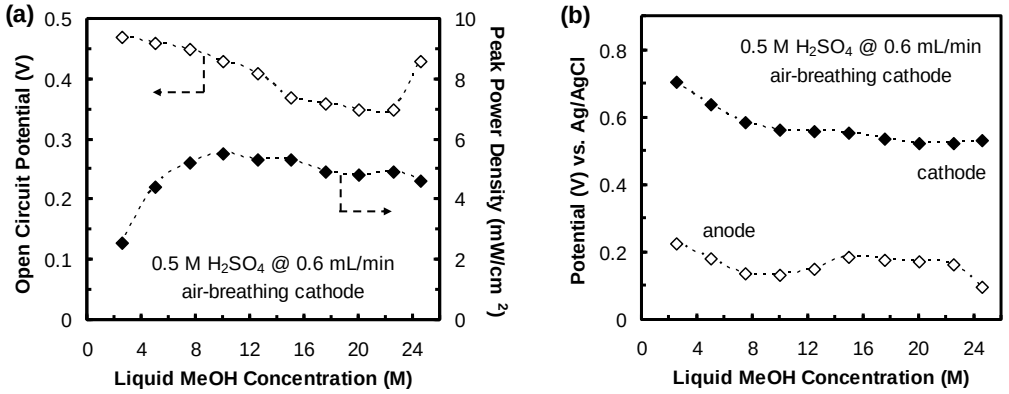

Figure 6.7. **(a)** Open circuit potential and peak power density of an acidic Gen-1 VF-DMFC as a function of liquid MeOH concentration. **(b)** The corresponding individual anode and cathode polarization curves. Studies were performed at room temperature with an air-breathing cathode, and 0.5 M H_2SO_4 flowing at 0.6 mL/min.

slightly increases and plateaus. Interestingly, the OCP spikes, due to a substantial drop in anode potential, when neat methanol (24.6 M) is used as the liquid source. A peak power density of 5.5 mW/cm^2 is achieved using 10 M liquid methanol as the fuel. Lower peak power densities are observed at methanol concentrations less than 10 M as a result of lower reaction rates on the catalytic surface of the anode in the presence of lower methanol concentrations in the vapor phase. Lower peak power densities are also seen at methanol concentrations higher than 10 M because the methanol crossover rate increases rapidly relative to the reaction rate at the anode. An apparent optimum exists between the methanol oxidation reaction rate and the methanol crossover rate at a fuel concentration of 10 M in the liquid reservoir. Again, interestingly, the increase in OCP observed using neat methanol does not translate into improved performance. For this VF-DMFC configuration, 10 M liquid methanol appears to be a global maximum that is unaffected by variations in electrolyte concentration, electrolyte flow rate, and oxidant delivery mode. Thus, unless otherwise specified, all subsequent Gen-1 VF-DMFC studies are performed using a fuel concentration of 10 M.

Figure 6.8a shows polarization and power density curves of a Gen-1 VF-DMFC as a function of H_2SO_4 concentration (0.25, 0.5, 0.75, 1, 1.5, and 2 M). Optimal fuel cell performances of 5.5, 5.6, and 5.7 mW/cm^2 were achieved at 0.5, 0.75, and 1.0 M H_2SO_4. At H_2SO_4 concentration lowers than 0.5 M, cell performance was dramatically reduced due to lowered electrolyte conductivity and thus increased ohmic losses. At H_2SO_4 concentrations greater than 1 M, cell performance was substantially reduced due to increased sulfate/bisulfate poisoning which block catalytic sites on electrodes [53]. Thus, unless otherwise specified, all subsequent VF-DMFC studies are performed with 0.5 M H_2SO_4 in the interest of minimizing any electrode degradation that may occur due to high acidic concentrations without sacrificing cell performance.

Figure 6.8b shows the polarization and power density curves of a Gen-1 VF-DMFC as a function of electrolyte flow rate (0.3, 0.6, and 0.9 mL/min). As mentioned above, methanol crossover appears flow rate independent as the optimal performance was still observed at a fuel concentration of 10 M methanol. An improvement in performance from 4.8 to 5.5 mW/cm^2 (~15%) is observed when increasing the

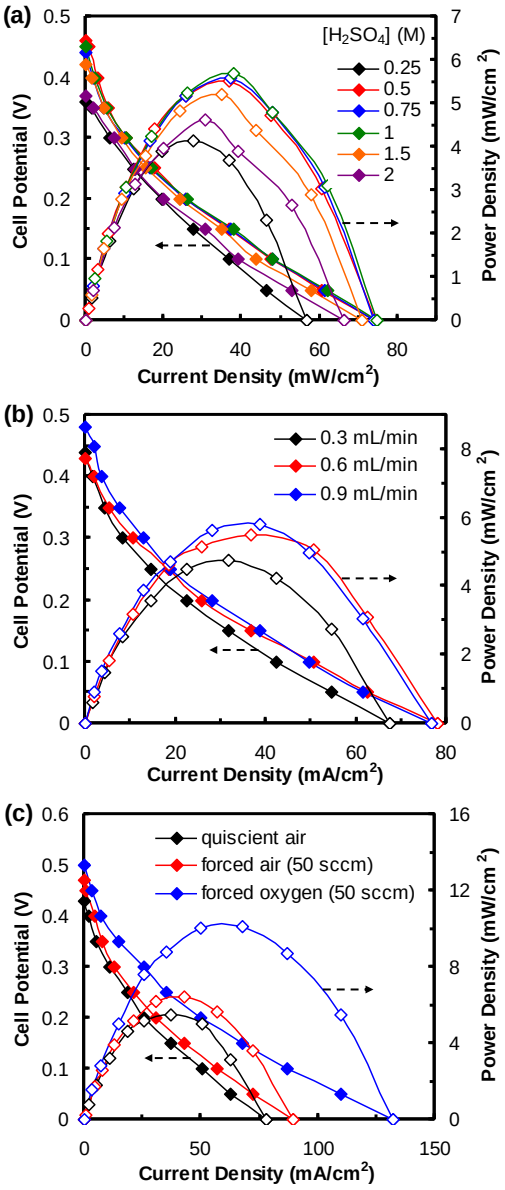

Figure 6.8. Polarization and power density curves of a Gen-1 VF-DMFC as a function of **(a)** electrolyte concentration, **(b)** electrolyte flow rate, and **(c)** oxidant delivery. Unless otherwise specified, all experiments are performed at room temperature with 10 M liquid methanol, an air-breathing cathode, and 0.5 M H_2SO_4 at 0.6 mL/min.

electrolyte flow rate from 0.3 to 0.6 mL/min. A smaller improvement in performance from 5.5 to 5.8 mW/cm^2 (~5%) is observed when the flow rate is further increased from 0.6 to 0.9 mL/min. These improvements in cell performance can be attributed to improved rates of water removal, and to a lesser extent the reduction in size of the proton-depletion boundary layer at the cathode [54]. Thus, unless otherwise specified, all subsequent VF-DMFC studies are performed using an electrolyte flow rate of 0.6 mL/min. It is worth noting that if the pumping losses are considered (assuming 40% pump efficiency) in this Gen-1 design, the net power output is slightly greater using an electrolyte flow rate 0.3 mL/min. This will be discussed in greater detail in section 6.3.5.

Figure 6.8c shows the polarization and power density curves of the VF-DMFC as a function of oxygen delivery mode (quiescent air, 50 sccm air, and 50 sccm oxygen). Under all three operating conditions, the polarization curves showed no abrupt drop in potential at higher current densities, indicating that the performance of this VF-DMFC configuration is not limited by oxygen transport to the cathode. The cell operated with forced air exhibited increased performance compared to the one operated with quiescent air, with observed PPDs of 6.4 and 5.5 mW/cm^2, respectively. This improvement is due to the enhanced oxygen transport to the cathode via convection compared to diffusion but would likely not offset the parasitic cost of adding a blower to the fuel cell system. The cell operated with forced oxygen demonstrated a considerable improvement in performance compared to the one operated with forced air, with an increase in observed PPD from 6.4 to 10.1 mW/cm^2. This enhancement is due to increased oxygen concentration flowing over the cathode which causes a higher Nernstian potential and an increased oxygen driving force to the cathode. However, because oxygen transport is not a key limiting factor in this current configuration and because on-board housing and delivery of

gaseous oxygen is unrealistic for portable fuel cell-based power sources, all subsequent VF-DMFC studies are performed using an air-breathing cathode.

6.3.4 Improvements in Cell Design and Operating Procedures

Compared to VF-DMFC designs reported in literature (see Table 6.1), the performance of the air-breathing Gen-1 VF-DMFC is mediocre. While, the OCPs are comparable, the PPDs obtained are ~55 - 85% less than those reported in literature. Thus, several changes are proposed to the cell design and the operating strategy that should make the second generation VF-DMFC (Gen-2 VF-DMFC) more competitive.

Microfluidic-based fuel cells suffer increased ohmic losses compared to membrane-based fuel cells due to the differences in electrode-to-electrode distances. Specifically, these microfluidic-based fuel cells have millimeter-scale gaps between electrodes whereas the reported membrane-based fuel cells have micrometer-scale gaps. However, due to the increased conductivity of liquid electrolytes (*e.g.*, 0.236 S/cm for 0.5 M H_2SO_4 at 25°C [55]) compared to polymeric membranes (*e.g.*, 0.093 ± 0.008 S/cm for fully-hydrated Nafion 117 at 30°C [56]), the performance of microfluidic-based fuel cells is comparable to that of membrane-based fuel cells. Reducing the electrode-to-electrode gap in microfluidic-based fuel cell may lead to performance improvements. Note that this improvement may not be a drastic as those observed in a membrane-based fuel cell due to the enhanced liquid electrolyte conductivity. Of course, these changes must be balanced by practical concerns such as increased pressure drops along the channel and increased fuel crossover due to reduced electrode-to-electrode distances. Thus, in the Gen-2 VF-DMFC the electrode-to-electrode gap was reduced from 0.2- to 0.15-cm (Table 6.3).

Several researchers have reported transient behavior after start-up for passive LF-DMFCs [20] and VF-DMFCs [30,38] due to the self-heating phenomena. During start-up, methanol crosses over the membrane and reacts at the cathode generating heat and increasing the cell temperature. This generated heat has both positive effects, increased electrochemical reaction rates, and negative effects, increased fuel crossover rates. Furthermore, significant amounts of heat are lost to the ambient surroundings limiting the temperature increase. Consequently, start-up in passive DMFC is typically characterized by: (*i*) a low initial OCP (methanol traveling to the anode), (*ii*) a high peak (methanol reaches the anode), (*iii*) a decay (methanol crosses over to the cathode) and finally (*iv*) a plateau and stabilization (balance of effects) [38]. The time required to balance these competing effects are characteristic to individual cells and operating conditions. While this self-heating phenomenon does not occur in the present configuration, due to the constantly refreshing electrolyte stream, an initial period of low OCP exists when methanol vapor travels from the liquid source to the anode catalyst layer (Figure 6.6). In the Gen-1 VF-DMFC, studies were performed after a 2 min period which may not be enough time for the OCP to stabilize. Extending the waiting time may increase and stabilize the methanol vapor concentration at the anode leading to beneficial Nernstian shifts (lower anode potentials). Consequently, in the Gen-2 VF-DMFC, the waiting time before experiments is extended to a 10 min period (Table 6.3).

Table 6.3. Changes in the design and operation of the VF-DMFC from first generation (Gen-1) to second generation (Gen-2) configurations.

Fuel Cell Parameter	Gen-1	Gen-2
Design: e-to-e gap (cm)	0.2	0.15
Operation: time (min)	2	10

6.3.5 Characterization of Second Generation VF-DMFC

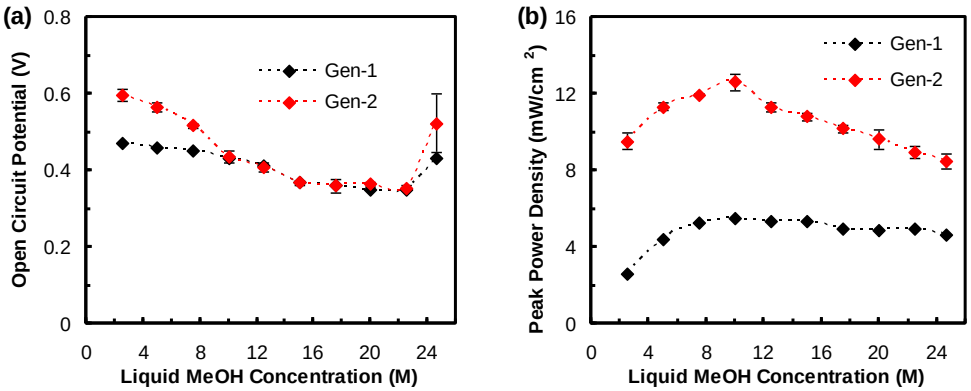

Figure 6.9. Comparative performances of acidic Gen-1 and Gen-2 VF-DMFCs as a function of liquid MeOH concentration in terms of **(a)** Open circuit potential and **(b)** peak power density. Studies were performed at room temperature with an air-breathing cathode, and 0.5 M H_2SO_4 flowing at 0.6 mL/min. Identical anode and cathode loadings were used for each cell.

The performances of Gen-1 and Gen-2 acidic VF-DMFCs were investigated as a function of methanol concentration to determine the impact of the modifications to cell design and operating procedure (Figure 6.9). Figure 6.9a shows the comparative OCPs of the Gen-1 and Gen-2 VF-DMFC under identical operating conditions. Studies in the Gen-2 VF-DMFC are performed in triplicate with cell disassembly between runs. A maximum OCP of 0.60 ±0.02 V is achieved using 2.5 M liquid methanol in the Gen-2 cell which represents a 0.13 ±0.02 V increase compared to peak OCP observed the previous design. The OCPs observed in the Gen-2 cell remain greater than those observed in the Gen-1 cell until a liquid methanol concentration of 10 M. At methanol concentrations ≥ 10 M and above, the OCPs of both designs are identical. Again, like in the Gen-1 cell, the OCP of the Gen-2 cell spikes (0.52 ± 0.08 V) when neat methanol is used as the liquid source. As shown in Figure 6.9b, while the trends of the PPD curves are similar, the Gen-2 cell significantly outperforms the Gen-1 cell at all methanol concentrations. Like the Gen-1 cell, an optimum power density (10.80 ± 0.20 mW/cm^2) in the Gen-2 cell is achieved using 10 M liquid methanol as the fuel. However, the Gen-2 cell is more

sensitive to increasing methanol concentrations (> 10 M) as highlighted by a sharper decrease in PPD compared to the Gen-1 cell. Again, like in the Gen-1 cell, the increase in OCP observed using neat methanol does not translate into improved performance.

To better understand the effects of each modification on the cell performance, comparative analyses are performed on the acidic Gen-1 and Gen-2 VF-DMFCs at three different methanol concentrations: 2.5, 10, and 24.6 M (Figure 6.10).

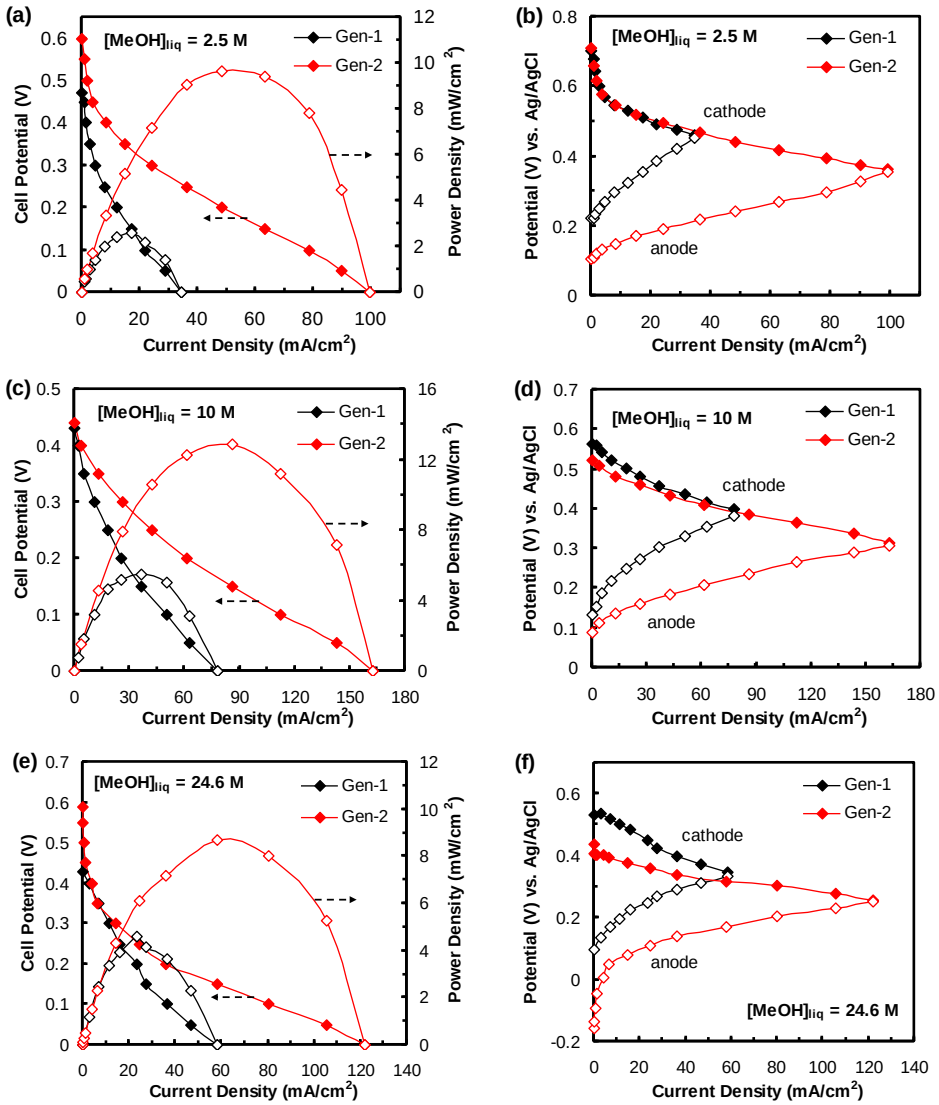

Figure 6.10. Polarization, power density curves, and individual electrode polarization curves for Gen-1 and Gen-2 acidic VF-DMFCs each configuration at liquid MeOH concentrations of **(a,b)** 2.5 M, **(c,d)** 10 M, and **(e,f)** 24.6 M. Studies were performed at room temperature with an air-breathing cathode, and 0.5 M H_2SO_4 flowing at 0.6 mL/min. Identical anode and cathode loadings were used for each cell.

Figures 6.10a and 6.10b show comparative cell performances at a low liquid methanol concentration (2.5 M). The Gen-2 cell significantly outperforms the Gen-1 cell in terms of OCP and PPD. The enhanced OCP in the Gen-2 cell can be attributed to the extended waiting time prior to experimentation which enables methanol vapor to concentrate at the anode stabilizes at a lower potential (Figure 6.10b). Furthermore, at this concentration fuel crossover is not an issue as the cathode potential remains the same despite the reduced electrode-to-electrode distance and the extended waiting period. The enhanced power density can be attributed to both the increased methanol concentration at the anode and the reduced electrode-to-electrode gap that lowers ohmic resistance. The reduced resistance leads to decreased ohmic losses in the Gen-2 cell which are highlighted by the shallower slopes observed for the overall polarization curve (Figure 6.10a) and the individual anode polarization curve (Figure 6.10b). Figures 6.10c and 6.10d show comparative cell performances at an optimal liquid methanol concentration (10 M). While, the cells have similar OCPs, the Gen-2 cell outperforms the Gen-1 cell due to the reduced ohmic losses (Figure 6.10c). The extended waiting time has no net gain as both the anode and cathode potential slightly lower. The anode shift is likely due to higher local methanol concentrations, while the cathode potential, possibly due to higher fuel crossover. Figures 6.10e and 6.10f show comparative cell performances at a very high methanol concentration (24.6 M). The Gen-2 cell outperforms the Gen-1 cell in terms of OCP and PPD due to reduced ohmic losses (Figure 6.10e). The difference in OCP can be attributed to significant reduction in anode potential after an extended waiting time (Figure 6.10f). However, this difference does not translate into power output as the Gen-2 cell shows significant anode kinetic losses.

In sum, the reduced electrode-to-electrode gap in the Gen-2 cell leads to a substantial increase in overall cell performance but also leads to an increase in fuel crossover at higher

liquid methanol concentration (≥ 10 M) which likely contributes, in part, to the sharper relative decrease in observed PPD (see Figure 6.9b). The extended waiting time in the Gen-2 cell leads to marked increase in OCP at lower liquid methanol concentrations (< 10 M) due to reduced anode potentials. The extended waiting times are not effective at higher liquid methanol concentrations (≥ 10 M) as the lowered anode potential is offset by lowered cathode potentials due to increased fuel crossover. No net gain is observed in fuel cell OCP at 10 M where peak power output is achieved (see Figure 6.9a)

Reducing the electrode-to-electrode gap also impacts the electrolyte flow rates in the microfluidic channel. For example, at a constant volumetric flowrate of 0.6 mL/min, the linear velocities are 0.15 and 0.2 cm/s for 0.2- and 0.15-cm gaps, respectively. In terms of performance, the differing superficial velocities have minimal effects on fuel cell performance as evidenced in Figure 6.8b. Reducing the electrode-to-electrode gap also increases the parasitic losses associated with pumping the electrolyte which, in turn, impacts the overall power output. In the fuel cell experimental set-up electrolyte is pumped from a syringe through polyethylene tubing to the microfluidic fuel cell. Once passing through the fuel cell the electrolyte travels through polyethylene tubing into a collection beaker. The effects of these pumping losses on overall power output can be described by the following equation:

$$P_{output} = P_{cell} - P_{pump} = P_{cell} - \left(\frac{Q \Delta P_{elec}}{\eta_{pump}} \right) \tag{6.7}$$

In Eq. 6.7, P_{output} represents the output power of the fuel cell system, P_{cell} represents the power generated by the fuel cell, P_{pump} represents the power required to pump the electrolyte through the fuel cell, Q represents the volumetric electrolyte flow rate, ΔP_{elec} represents the pressure drop the electrolyte experiences, and η_{pump} represents the pump efficiency. When calculating the

overall power output, the pump efficiency is assumed be to 0.4. The electrolyte pressure drops along channel and at contractions can be described by the following two equations:

$$\Delta P_{elec} = \left(\frac{8\eta QL}{\pi r^4} \right) \tag{6.8}$$

$$\left(\frac{\Delta P_{elec}}{\rho g} \right) + \left(\frac{(v_1)^2 - (v_2)^2}{2g} \right) + \Delta z = 0 \tag{6.9}$$

In Eq. 6.8, η represents the electrolyte dynamic viscosity, L represents the channel length, and r represents the hydraulic radius. In Eq 6.9, ρ represents the electrolyte density, g represents the gravitational constant, v represents the fluid velocity, and z represents the change in height. Several assumptions were made when calculating the electrolyte pressure drops in the fuel cell set-up. The electrolyte was assumed to behave like an incompressible fluid. The pressure at the electrolyte outlet was assumed to be atmospheric. The changes in height were assumed to negligible. The net power outputs calculated for the Gen-1 and Gen 2 VF-DMFC were ~1.86 and ~7.13 mW/cm^2 at an electrolyte flow rate of 0.6 mL/min. Note that the fuel cell experimental set-up is not optimized to minimizing pumping losses (*e.g.*, minimal tubing length). However, the fuel cell benefits of reducing the electrode-to-electrode gap outweigh the pumping costs. Further optimization of these structural parameters may lead to significant leaps in fuel cell system performance.

6.3.6 Characterization of an Alkaline VF-DMFC

As highlighted previously in Chapter 1, operating fuel cells in alkaline media, as opposed to acidic media, is advantageous as enhanced methanol oxidation reaction and oxygen reduction reaction kinetics improve fuel cell efficiency [57]. Moreover, a wide range of inexpensive non-precious catalysts (*i.e.,* Ag cathodes, Ni anodes) materials are stable and active under alkaline conditions which can dramatically reduce fuel cell costs. Though among the first fuel cell

technologies to be successfully demonstrated, traditional alkaline fuel cells which utilize concentrated liquid electrolytes (*i.e.*, 30 - 45 wt% KOH) were typically not considered for direct liquid applications due to perceived carbonate formation issues. Carbonate formation (CO_3^{2-} / HCO_3^-) occurs when the hydroxyl ions present in the electrolyte react with carbon dioxide from either organic fuel oxidation, or the quiescent environment. In the presence of mobile cations, the carbonates can precipitate within the electrodes, where they damage the microporous architecture, block electrocatalytic sites, and eventually reduce performance. Furthermore, carbonate formation reduces the hydroxyl concentration in the liquid electrolyte, thus lowering electrolyte conductivity and electrode kinetics.

Of late, significant efforts have been focused on developing high performance alkaline anion exchange membranes (AAEMs) which reduce the adverse effects of carbonate formation [58]. AAEMs are less susceptible to carbonate precipitation because no mobile cations exist *within the membrane* enabling less stringent operating conditions, *e.g.* air-breathing cathodes. Still, the presence of carbonate ions in the AAEM can adversely impact cell performance (*e.g.*, unfavorable pH gradients, reduced conductivity) particularly in the case of direct liquid AAEM-based fuel cells [59]. For example, Wang *et al.* demonstrated that, in an AAEM-based DMFC at room temperature, a substantial pH gradient (6.1 pH units) exists between the cathode (due to OH^- production) and the anode (due to CO_3^{2-} / HCO_3^- generation), leading to a large voltage loss (ca. 360 mV) [59]. By operating the AAEM-DMFC at elevated temperatures ($T \approx 80\ ^oC$), the thermodynamic drawbacks can be minimized because: (*i*) the pH gradient and consequent voltage loss between electrodes is reduced, and (*ii*) the reaction kinetics at both electrodes is improved which counters the voltage losses. Unfortunately operating the fuel cell under these conditions lead to increased parasitic losses and reduced membrane stability [58]. Alternatively,

to minimize the adverse effects of carbonate formation on alkaline DMFC performance, several authors have introduced supporting alkaline electrolytes into the anodic fuel streams to control the pH and to assist in the electro-oxidation reaction [60,61]. Note that, in these configurations, AAEM stability is adversely affect by extended exposure to an aqueous electrolyte [62] and carbonate precipitation is also possible.

To date, no passive or semi-passive alkaline LF- or VF-DMFCs have been reported primarily due to aforementioned carbonate-related challenges. However, the present semi-passive VF-DMFC design is well-suited for alkaline operation as the flowing electrolyte stream (*i*) enables the immediate removal of carbonates generated at the anode surface and (*ii*) prevents the formation of adverse pH gradients. Furthermore, an alkaline VF-DMFC may be more competitive than an acidic VF-DMFC due to the possibility of increased performance and reduced costs. Figure 6.11 shows polarization and power density curves for a Gen-2 VFMFC operated with acidic (0.5 M H_2SO_4) and alkaline (1 M KOH) media under otherwise identical conditions. The OCPs and PPDs obtained in VF-DMFCs operated in acidic and alkaline media were 0.435 ± 0.02 V and 12.61 ± 0.44 mW/cm^2, and 0.603 ± 0.01 V and 21.78 ± 0.43 mW/cm^2, respectively. The superior performance of the alkaline VF-DMFC can be attributed to enhanced electrode reaction kinetics under alkaline conditions. For the alkaline VF-DMFC peak power output, 24.67 ± 0.76 mW/cm^2, was actually observed using

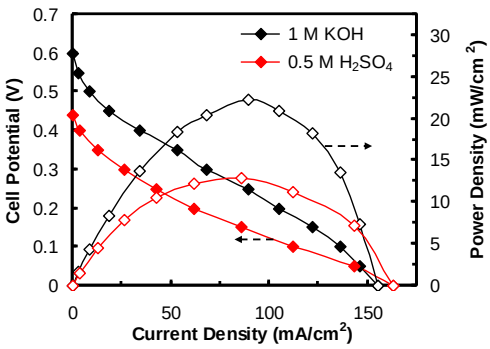

Figure 6.11. Polarization and power density curves for a Gen-2 VF-DMFC operated with either acidic or alkaline electrolyte. Studies were performed at room temperature with an air-breathing cathode, 10 M liquid methanol fuel, and electrolyte flowing at 0.6 mL/min. Alkaline VF-DMFC studies are performed with Sigracet 35 BC-based electrodes rather than Sigracet 24 BC-based electrodes.

12.5 M liquid methanol fuel. This shift is likely due to the hydroxyl ion gradient - from cathode to anode - which hinders fuel crossover. Furthermore, the cell demonstrates good short-term performance stability (not shown, N = 4) which suggests the flowing electrolyte stream effectively removes most formed carbonates.

As mentioned earlier, the superior performance of alkaline fuel cells enable the reduction of precious metal catalyst loading and/or the use of cheaper non-precious metal catalysts which can both substantially reduce the fuel cell system costs. In the present VF-DMFC configuration, the anode requires large amounts of PtRu catalyst (nominally 10 mg/cm^2) to achieve adequate

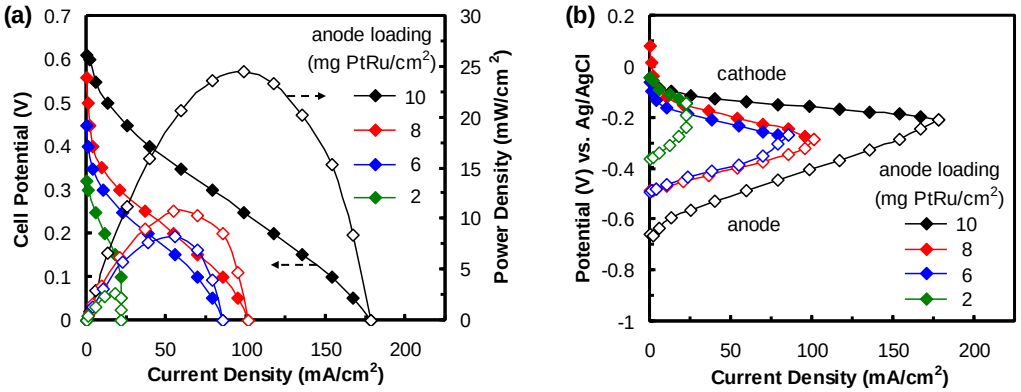

Figure 6.12. **(a)** Polarization and power density curves for an alkaline Gen-2 VF-DMFC as a function of anode catalyst (PtRu black) loading. **(b)** Corresponding individual electrode polarization curves. Studies were performed at room temperature with an air-breathing cathode, 12.5 M liquid methanol fuel, and 0.5 M H_2SO_4 flowing at 0.6 mL/min. Experiments performed with Sigracet 35 BC-based electrodes.

performance. Reducing this anode loading, without sacrificing performance and durability, is an important step towards improving the viability of this VF-DMFC design. Figure 6.12a shows the polarization and power density curves of an alkaline Gen-2 VF-DMFC as a function of anode loading. Peak outputs of 24.50, 10.80, 8.25, and 2.7 mW/cm^2 were observed for anode loadings of 10, 8, 6, and 2 mg PtRu /cm^2, respectively. The reduced performance at lower anode loading can be attributed to increased kinetic losses which are primarily observed on the anode (Figure 6.12b). Interestingly, the mass activity (mA/mg) of the highest loading (10 mg/cm^2) is

significantly greater than that of the lower loadings which all overlay (not shown). Thus, a critical next step would be improved anode design (*e.g.,* microstructure) to simultaneously increase the electrochemically active surface area and reduce the bulk catalyst loading.

While no semi-passive or passive alkaline DMFCs have been reported, the performance of this present configuration compares favorable with similar small-scale alkaline DMFCs which utilize active reactant delivery (Table 6.4) [63-66]. Furthermore, this alkaline VF-DMFC configuration is competitive with the acidic VF-DMFCs reported in literature (see Table 6.3).

Table 6.4. Representative literature survey of different small-scale alkaline DMFC configurations. Results are compared to present work.

Reference	Anode / Cathode		Electrolyte	Max. Open Current Potential (V)	Peak Power Density (mW/cm^2)	Experimental Details
	Reactant Delivery	Catalyst				
Verma and Basu [63]	active liquid MeOH air-breathing	1 mg Pt black/cm^2 MnO_2 (unknown loading)	3 M KOH	~1.0	~15	2 M liq. MeOH, 1 mL/min flow, T = 25°C, MRFC (1)
Yang *et al.* [64]	active liquid MeOH air-breathing	4 mg PtRu black/cm^2 γ-MnO_2 (unknown loading)	PVA/10% HAP composite membrane (2)	0.8	11.48	2 M liq. MeOH + 8 M KOH, T = 25°C, Ti-based anode
Adams *et al.* [65]	active liquid MeOH forced air	4 mg PtRu black/cm^2 4 mg Pt black/cm^2	Morgane ADP100-2	~0.62	0.54	2 M liq. MeOH, 10 mL/min flow, 2 L/min airflow, T = 50°C, 100% RH
Brushett *et al.* [66]	active liquid MeOH air-breathing	10 mg PtRu black/cm^2 2 mg Pt black/cm^2	1 M KOH	1.05	17.2	1 M liq. MeOH, RT, LFFC (3)
This work	passive vapor MeOH air-breathing	10 mg PtRu black/cm^2 2 mg Pt/C/cm^2 (50 wt% Pt)	1 M KOH	0.75	24.5	10 M liq. MeOH, RT, 0.6 mL/min electrolyte flow

Note: Maximum open circuit potential and peak power density were not necessarily observed at the same operating conditions.
(1) Mixed Reactant Fuel Cell, (2) Poly(vinyl alcohol) / hydroxyapatite, (3) Laminar Flow Fuel Cell

6.4 Conclusions

Simple semi-passive and passive vapor feed DMFCs, operated at near ambient conditions and fed with concentrated methanol solutions may be viable alternative power sources to Li-ion batteries for portable electronics. However, membrane-based VF-DMFC technologies are limited by anode dry-out and methanol crossover. To overcome these challenges, a proof-of-concept VF-DMFC has been developed which utilizes a flowing electrolyte in place of a polymeric membrane. The performance of this microfluidic-based VF-DMFC has been characterized as a function of operating conditions and structural parameters. These studies

highlighted liquid methanol concentration, waiting time, and electrode-to-electrode gap as key parameters that influence VF-DMFC performance. Promisingly, though unoptimized, the fuel cell peak power (~12.6 and ~24.7 mW/cm^2 for acidic and alkaline, respectively) was substantially greater than the power required to pump the electrolyte (~3.7 mW/cm^2), confirming system viability. While more rigorous and systematic analyses of the present cell design and operating strategies will surely lead to further performance enhancements, serious consideration must be given to following two broader system-level challenges.

First, across all experimental conditions in the present cell design, peak power density was observed at concentrations around 10 - 12.5 M liquid methanol. At this point, cell performance is at an optimal balance between enhanced methanol oxidation at the anode and limited methanol crossover to the cathode. While increasing the methanol concentrations leads to lowered anode potentials, this improvement is offset by increased fuel crossover which reduced cathode potentials. Ideally, a VF-DMFC must operate at mass-transport limiting conditions utilizing neat methanol concentrations to maximize system energy density. Thus, efforts should be focused on developing passive means of controlling methanol evaporation (*e.g.*, wicked well) and transport (*e.g.*, polymeric barrier layers) to the anode. Furthermore, efforts should be focused on improving anode design (*e.g.*, microstructured electrodes) to increase the catalyst layer surface area, while maintaining or reducing the catalyst loading, to enhance methanol utilization and, consequently, fuel cell efficiency.

Second, an on-board circulating electrolyte system adds both complexity and volume (reduced energy density) to a fuel cell-based power source. Thus, the flowing electrolyte stream must provide certain "added-value" to the device. While flowing acidic electrolytes enhance water management and reduce fuel crossover, these improvements alone may not be enough to

offset the simplicity and robustness of a membrane-based system. However, in addition to these aforementioned improvements, flowing alkaline electrolytes also enable enhanced electrode kinetics and allow for the use of inexpensive materials for both electrocatalysis and system construction. Thus, efforts must be focused on alkaline VF-DMFC development which appears more promising than its acidic counterpart. Note that a detailed analysis of the impact of sustained carbonate formation on performance and durability of an alkaline VF-DMFC-based system would be required to determine the viability of this configuration.

6.5 References

1. Kundu, A., J.H. Jang, J.H. Gil, C.R. Jung, H.R. Lee, S.H. Kim, B. Ku, and Y.S. Oh, *Micro-fuel cells - Current development and applications.* Journal of Power Sources, 2007. **170**(1): p. 67-78.
2. Dyer, C.K., *Fuel cells for portable applications.* Journal of Power Sources, 2002. **106**(1-2): p. 31-34.
3. Perry, M.L. and T.F. Fuller, *A historical perspective of fuel cell technology in the 20th century.* Journal of the Electrochemical Society, 2002. **149**(7): p. S59-S67.
4. Carrette, L., K.A. Friedrich, and U. Stimming, *Fuel cells: Principles, types, fuels, and applications.* Chemphyschem, 2000. **1**(4): p. 162-193.
5. Demirci, U.B., *Direct liquid-feed fuel cells: Thermodynamic and environmental concerns.* Journal of Power Sources, 2007. **169**(2): p. 239-246.
6. Gurau, B. and E.S. Smotkin, *Methanol crossover in direct methanol fuel cells: a link between power and energy density.* Journal of Power Sources, 2002. **112**(2): p. 339-352.
7. Zhao, T.S., W.W. Yang, R. Chen, and Q.X. Wu, *Towards operating direct methanol fuel cells with highly concentrated fuel.* Journal of Power Sources, 2010. **195**(11): p. 3451-3462.
8. Kuver, A. and W. Vielstich, *Investigation of methanol crossover and single electrode performance during PEMDMFC operation - A study using a solid polymer electrolyte membrane fuel cell system.* Journal of Power Sources, 1998. **74**(2): p. 211-218.
9. Cruickshank, J. and K. Scott, *The degree and effect of methanol crossover in the direct methanol fuel cell.* Journal of Power Sources, 1998. **70**(1): p. 40-47.
10. Buie, C.R., J.D. Posner, T. Fabian, C.A. Suk-Won, D. Kim, F.B. Prinz, J.K. Eaton, and J.G. Santiago, *Water management in proton exchange membrane fuel cells using integrated electroosmotic pumping.* Journal of Power Sources, 2006. **161**(1): p. 191-202.
11. Yi, J.S., J.D.L. Yang, and C. King, *Water management along the flow channels of PEM fuel cells.* AIChE Journal, 2004. **50**(10): p. 2594-2603.
12. Ge, S.H., X.G. Li, and I.M. Hsing, *Internally humidified polymer electrolyte fuel cells using water absorbing sponge.* Electrochimica Acta, 2005. **50**(9): p. 1909-1916.
13. Borup, R., J. Meyers, B. Pivovar, Y.S. Kim, R. Mukundan, N. Garland, D. Myers, M. Wilson, F. Garzon, D. Wood, P. Zelenay, K. More, K. Stroh, T. Zawodzinski, J. Boncella, J.E. McGrath, M. Inaba, K. Miyatake, M. Hori, K. Ota, Z. Ogumi, S. Miyata, A. Nishikata, Z. Siroma, Y. Uchimoto, K. Yasuda, K.I. Kimijima, and N. Iwashita, *Scientific aspects of polymer electrolyte fuel cell durability and degradation.* Chemical Reviews, 2007. **107**(10): p. 3904-3951.
14. Zhao, T.S., R. Chen, W.W. Yang, and C. Xu, *Small direct methanol fuel cells with passive supply of reactants.* Journal of Power Sources, 2009. **191**(2): p. 185-202.

15. Yang, Y.M. and Y.C. Liang, *A direct methanol fuel cell system with passive fuel delivery based on liquid surface tension.* Journal of Power Sources, 2007. **165**(1): p. 185-195.
16. Chan, Y.H., T.S. Zhao, R. Chen, and C. Xu, *A self-regulated passive fuel-feed system for passive direct methanol fuel cells.* Journal of Power Sources, 2008. **176**(1): p. 183-190.
17. Chan, Y.H., T.S. Zhao, R. Chen, and C. Xu, *A small mono-polar direct methanol fuel cell stack with passive operation.* Journal of Power Sources, 2008. **178**(1): p. 118-124.
18. Chang, I., S. Ha, J. Kim, J. Lee, and S.W. Cha, *Performance evaluation of passive direct methanol fuel cell with methanol vapour supplied through a flow channel.* Journal of Power Sources, 2008. **184**(1): p. 9-15.
19. Chang, I., S. Ha, S. Kim, S. Kang, J. Kim, K. Choi, and S.W. Cha, *Operational condition analysis for vapor-fed direct methanol fuel cells.* Journal of Power Sources, 2009. **188**(1): p. 205-212.
20. Chen, R. and T.S. Zhao, *Performance characterization of passive direct methanol fuel cells.* Journal of Power Sources, 2007. **167**(2): p. 455-460.
21. Chen, R. and T.S. Zhao, *A novel electrode architecture for passive direct methanol fuel cells.* Electrochemistry Communications, 2007. **9**(4): p. 718-724.
22. Chen, R. and T.S. Zhao, *Porous current collectors for passive direct methanol fuel cells.* Electrochimica Acta, 2007. **52**(13): p. 4317-4324.
23. Chen, R., T.S. Zhao, and J.G. Liu, *Effect of cell orientation on the performance of passive direct methanol fuel cells.* Journal of Power Sources, 2006. **157**(1): p. 351-357.
24. Eccarius, S., F. Krause, K. Beard, and C. Agert, *Passively operated vapor-fed direct methanol fuel cells for portable applications.* Journal of Power Sources, 2008. **182**(2): p. 565-579.
25. Eccarius, S., X.H. Tian, F. Krause, and C. Agert, *Completely passive operation of vapor-fed direct methanol fuel cells for portable applications.* Journal of Micromechanics and Microengineering, 2008. **18**(10).
26. Guo, Z. and A. Faghri, *Vapor feed direct methanol fuel cells with passive thermal-fluids management system.* Journal of Power Sources, 2007. **167**(2): p. 378-390.
27. Jewett, G., Z. Guo, and A. Faghri, *Water and air management systems for a passive direct methanol fuel cell.* Journal of Power Sources, 2007. **168**(2): p. 434-446.
28. Jewett, G., Z. Guo, and A. Faghri, *Performance characteristics of a vapor feed passive miniature direct methanol fuel cell.* International Journal of Heat and Mass Transfer, 2009. **52**(19-20): p. 4573-4583.
29. Kho, B.K., B. Bae, M.A. Scibioh, J. Lee, and H.Y. Ha, *On the consequences of methanol crossover in passive air-breathing direct methanol fuel cells.* Journal of Power Sources, 2005. **142**(1-2): p. 50-55.
30. Kim, H., *Passive direct methanol fuel cells fed with methanol vapor.* Journal of Power Sources, 2006. **162**(2): p. 1232-1235.
31. Li, X., A. Faghri, and C. Xu, *Water management of the DMFC passively fed with a high-concentration methanol solution.* International Journal of Hydrogen Energy, 2010. **35**(16): p. 8690-8698.
32. Liu, J.G., T.S. Zhao, R. Chen, and C.W. Wong, *The effect of methanol concentration on the performance of a passive DMFC.* Electrochemistry Communications, 2005. **7**(3): p. 288-294.
33. Liu, J.G., T.S. Zhao, Z.X. Liang, and R. Chen, *Effect of membrane thickness on the performance and efficiency of passive direct methanol fuel cells.* Journal of Power Sources, 2006. **153**(1): p. 61-67.
34. Rice, J. and A. Faghri, *Analysis of a passive vapor feed direct methanol fuel cell.* International Journal of Heat and Mass Transfer, 2008. **51**(3-4): p. 948-959.
35. Shimizu, T., T. Momma, M. Mohamedi, T. Osaka, and S. Sarangapani, *Design and fabrication of pumpless small direct methanol fuel cells for portable applications.* Journal of Power Sources, 2004. **137**(2): p. 277-283.
36. Tominaka, S., S. Ohta, H. Obata, T. Momma, and T. Osaka, *On-chip fuel cell: Micro direct methanol fuel cell of an air-breathing, membraneless, and monolithic design.* Journal of the American Chemical Society, 2008. **130**(32): p. 10456-10457.
37. Wu, Q.X., T.S. Zhao, R. Chen, and W.W. Yang, *A microfluidic-structured flow field for passive direct methanol fuel cells operating with highly concentrated fuels.* Journal of Micromechanics and Microengineering, 2010. **20**(4).
38. Xu, C., A. Faghri, and X.L. Li, *Development of a High Performance Passive Vapor-Feed DMFC Fed with Neat Methanol.* Journal of the Electrochemical Society, 2010. **157**(8): p. B1109-B1117.

39. Xu, C., A. Faghri, X.L. Li, and T. Ward, *Methanol and water crossover in a passive liquid-feed direct methanol fuel cell.* International Journal of Hydrogen Energy, 2010. **35**(4): p. 1769-1777.
40. Ahmad, M.M., S.K. Kamarudin, W.R.W. Daud, and Z. Yaakub, *High power passive μ–DMFC with low catalyst loading for small power generation.* Energy Conversion and Management, 2010. **51**(4): p. 821-825.
41. Prakash, S. and P.A. Kohl, *Performance of carbon dioxide vent for direct methanol fuel cells.* Journal of Power Sources, 2009. **192**(2): p. 429-434.
42. Prakash, S., W. Mustain, and P.A. Kohl, *Carbon dioxide vent for direct methanol fuel cells.* Journal of Power Sources, 2008. **185**(1): p. 392-400.
43. Zhang, H.F. and I.M. Hsing, *Flexible graphite-based integrated anode plate for direct methanol fuel cells at high methanol feed concentration.* Journal of Power Sources, 2007. **167**(2): p. 450-454.
44. Neburchilov, V., J. Martin, H.J. Wang, and J.J. Zhang, *A review of polymer electrolyte membranes for direct methanol fuel cells.* Journal of Power Sources, 2007. **169**(2): p. 221-238.
45. Kim, W.J., H.G. Choi, Y.K. Lee, J.D. Nam, S.M. Cho, and C.H. Chung, *Suppression of the methanol crossover by hydrogels in passively operated flat-pack type DMFCs and its application for the power source of cellular phone.* Journal of Power Sources, 2006. **163**(1): p. 98-102.
46. Abdelkareem, M.A. and N. Nakagawa, *DMFC employing a porous plate for an efficient operation at high methanol concentrations.* Journal of Power Sources, 2006. **162**(1): p. 114-123.
47. Guo, Z. and A. Faghri, *Miniature DMFCs with passive thermal-fluids management system.* Journal of Power Sources, 2006. **160**(2): p. 1142-1155.
48. NIST. *National Insitute of Standards and Technology (NIST) Chemistry Webbook: Standard Reference Database Number 69*. February 1, 2010 [cited 2007 March]; Available from: http://webbook.nist.gov/chemistry/.
49. Gmehling, J., U. Onken, and W. Arlt, *Vapor-liquid equilibrium data collection*. 1977, Frankfurt: Dechema.
50. Cussler, E.L., *Diffusion: Mass Transfer in Fluid Systems*. 2nd ed. 1997, New York: Cambridge University Press.
51. Reid, R.C., J.M. Prausnitz, and B.E. Poling, *The Properties of Gases and Liquids*. 4th ed. 1987, New York: McGraw-Hill Book Company.
52. Cindrella, L., A.M. Kannan, J.F. Lin, K. Saminathan, Y. Ho, C.W. Lin, and J. Wertz, *Gas diffusion layer for proton exchange membrane fuel cells-A review.* Journal of Power Sources, 2009. **194**(1): p. 146-160.
53. Horanyi, G., *Radiotracer Studies of Adsorption/Sorption Phenomena at Electrode Surfaces*, in *Interfacial Electrochemistry: Theory, Experiment, and Application*, A. Wieckowski, Editor. 1999, Marcel Dekker Inc.: New York. p. 477-491.
54. Jayashree, R.S., M. Mitchell, D. Natarajan, L.J. Markoski, and P.J.A. Kenis, *Microfluidic hydrogen fuel cell with a liquid electrolyte.* Langmuir, 2007. **23**(13): p. 6871-6874.
55. Prentice, G., *Electrochemical Engineering Principles*. 1991, Englewood Cliffs: Prentice Hall.
56. Varcoe, J.R., *Investigations of the ex situ ionic conductivities at 30 degrees celsius of metal-cation-free quaternary ammonium alkaline anion-exchange membranes in static atmospheres of different relative humidities.* Physical Chemistry Chemical Physics, 2007. **9**(12): p. 1479-1486.
57. Spendelow, J.S. and A. Wieckowski, *Electrocatalysis of oxygen reduction and small alcohol oxidation in alkaline media.* Physical Chemistry Chemical Physics, 2007. **9**(21): p. 2654-2675.
58. Varcoe, J.R. and R.C.T. Slade, *Prospects for alkaline anion-exchange membranes in low temperature fuel cells.* Fuel Cells, 2005. **5**(2): p. 187-200.
59. Wang, Y., L. Li, L. Hu, L. Zhuang, J.T. Lu, and B.Q. Xu, *A feasibility analysis for alkaline membrane direct methanol fuel cell: thermodynamic disadvantages versus kinetic advantages.* Electrochemistry Communications, 2003. **5**(8): p. 662-666.
60. Matsuoka, K., Y. Iriyama, T. Abe, M. Matsuoka, and Z. Ogumi, *Alkaline direct alcohol fuel cells using an anion exchange membrane.* Journal of Power Sources, 2005. **150**: p. 27-31.
61. Scott, K., E. Yu, G. Vlachogiannopoulos, M. Shivare, and N. Duteanu, *Performance of a direct methanol alkaline membrane fuel cell.* Journal of Power Sources, 2008. **175**(1): p. 452-457.
62. Vega, J.A., C. Chartier, and W.E. Mustain, *Effect of hydroxide and carbonate alkaline media on anion exchange membranes.* Journal of Power Sources, 2010. **195**(21): p. 7176-7180.

63. Verma, A. and S. Basu, *Direct alkaline fuel cell for multiple liquid fuels: Anode electrode studies.* Journal of Power Sources, 2007. **174**(1): p. 180-185.
64. Yang, C.C., S.J. Chiu, and C.T. Lin, *Electrochemical performance of an air-breathing direct methanol fuel cell using poly(vinyl alcohol)/hydroxyapatite composite polymer membrane.* Journal of Power Sources, 2008. **177**(1): p. 40-49.
65. Adams, L.A., S.D. Poynton, C. Tamain, R.C.T. Slade, and J.R. Varcoe, *A carbon dioxide tolerant aqueous-electrolyte-free anion-exchange membrane alkaline fuel cell.* Chemsuschem, 2008. **1**(1-2): p. 79-81.
66. Brushett, F.R., R.S. Jayashree, W.P. Zhou, and P.J.A. Kenis, *Investigation of fuel and media flexible laminar flow-based fuel cells.* Electrochimica Acta, 2009. **54**(27): p. 7099-7105.

Chapter 7

Summary of Accomplishments and Future Directions

7.1 Summary of Accomplishments

A clear need exists for novel approaches to producing and utilizing energy in more efficient ways, in light of society's ever increasing demand as well as growing concerns with respect to climate change related to CO_2 emissions [1]. The development of low temperature fuel cell technologies will continue to play a critical role in many alternative energy conversion strategies, especially for portable electronics and automotive applications [2-7]. However, widespread commercialization of acidic and alkaline fuel cell technologies has yet to be achieved mainly due to a combination of high costs, insufficient durability and system performance limitations [5]. Improved understanding of the complex electrochemical, transport, and degradation processes that govern the performance and durability of novel fuel cell components, particularly catalysts and electrodes, *within operating alkaline or acidic fuel cells* is critical to designing robust, inexpensive configurations that are required for commercial introduction [8-11]. The development of novel analytical platforms and techniques to probe these critical underlying processes is the primary focus of this thesis.

Previously, membraneless microfluidic fuel cells have been developed to address some of the aforementioned fuel cell challenges. At the microscale, the laminar nature of fluid flow eliminates the need for a physical barrier, such as a stationary membrane, while still allowing ionic transport between electrodes. This enables the development of many unique and innovative fuel cell designs. In addition to addressing water management and fuel crossover issues, these laminar flow-based systems allow for the independent specification of individual stream compositions (*e.g.*, pH). Furthermore, the use of a liquid electrolyte enables the simple

in-situ analysis of individual electrode performance using an off-the-shelf reference electrode. These advantages may be leveraged to develop microfluidic fuel cells as versatile electro-analytical platforms for the characterization and optimization of catalysts and electrodes for fuel cell applications. To this end, a pH-flexible microfluidic H_2/O_2 fuel cell has been developed that enables the study of electrochemical, transport, and degradation processes at the two electrodes *independently*, without factors such as water management complicating the experiment and data analysis (Figure 7.1) [12-20]. This platform helps to bridge the huge gap between traditional characterization of catalyst structure and activity within a 3-electrode electrochemical cell and analyses of catalyst/electrode performance and durability within actual fuel cell systems. For analytical investigations, the flowing stream (*i*) enables autonomous control over electrolyte parameters (*i.e.*, pH, composition) and consequently the local electrode environments, as well as (*ii*) allows for the independent *in-situ* analyses of catalyst and/or electrode performance and degradation characteristics via an external reference electrode. *In sum, this microfluidic analytical platform enables a high number of experimental degrees of freedom, previously limited to a 3-electrode electrochemical cell, to be employed in a working fuel cell.*

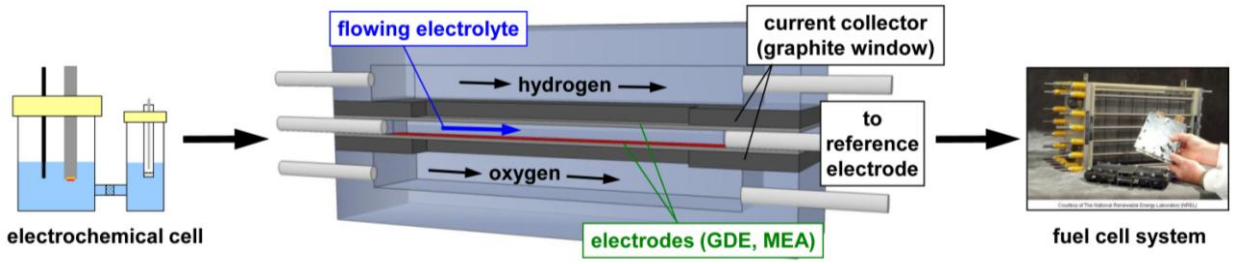

Figure 7.1. Bridging the gap between traditional three-electrode electrochemical cells and actual working fuel cell systems by employing a microfluidic H_2/O_2 fuel cell, as a versatile electro-analytical platform, for *in-situ* catalyst and electrode investigations.

Using this microfluidic H_2/O_2 fuel cell as a versatile analytical platform, the focus of this doctoral work has been three-fold:

- **Comprehensive analysis and optimization of individual electrode and overall alkaline fuel cell (AFC) performance as a function of electrode preparation methods and operating parameters [16-18,20].** Key factors that govern the performance and durability of cathodes and anodes have been identified over a range of operating conditions. Furthermore, the impact of carbonates (an unwanted by-product due to the reaction of carbon dioxide and hydroxyl ions) on individual electrode and overall cell performance has been fully characterized such that critical concentrations and exposure times can be elucidated which, in turn, will facilitate the development of improved materials and optimized operating protocols. This work has led to a future collaboration with a commercial partner (Ovonic Fuel Cell Company) to optimize their AFC systems.
- **Detailed *in-situ* characterizations of promising novel cathode catalysts for the oxygen reduction reaction (ORR) for application in acidic and alkaline fuel cells [12,17,18].** Specifically, using this platform, a carbon-supported Copper Complex of 3,5-Diamino-1,2,4-triazole (Cu-tri/C), has been integrated in a gas diffusion electrode and characterized under realistic fuel cell operating conditions. Under alkaline conditions, the absolute Cu-tri/C cathode performance is comparable to that of a Pt/C cathode. Furthermore, at a commercially relevant potential, the measured mass activity of an unoptimized Cu-tri/ C-based cathode was significantly greater than that of similar Pt/C- and Ag/C-based cathodes. These promising results represent the first report of a synthetic multi-Cu complex as a cathode catalyst material for AFC applications.

- **Investigation of the structure-activity relationships of fuel cell electrodes by aligning *in-situ* electrochemical analyses with X-ray computed microtomographic (MicoCT) structural analyses [15,16].** Qualitative analyses of electrode structure and organization have been performed to identify performance-limiting factors such as poor catalyst distribution. Furthermore, robust quantitative protocols have been developed for probing local properties within in the 3D electrode architecture. By combining electrochemical and visualization methods, shifts in electrode performance have been correlated to physical changes in structure [16].

Furthermore, the utility of this microfluidic configuration has been explored for energy conversion applications as a microscale power source:

- **A proof-of-concept semi-passive vapor-feed direct methanol fuel cell (VF-DMFC) has been developed which utilizes a flowing electrolyte in place of a polymeric membrane.** The performance of this microfluidic-based VF-DMFC has been characterized as a function of operating conditions and structural parameters. The media flexibility enabled by the flowing electrolyte stream facilitates the development of promising alkaline VF-DMFC configuration which may be considerably cheaper than its acidic membrane-based counterparts.

7.2 Future Directions

While future areas of research are suggested in the conclusion section of each chapter, the work presented in this thesis will hopefully open a broader research field rich with analytical opportunities. For example, a similar microfluidic configuration is being employed as an electrochemical reactor for investigating efficient CO_2 reduction processes to value-added

compounds (*i.e.*, formic acid, syngas) [21]. Thus, the goal of this section is to provide on "big picture" ideas for future research areas:

- Novel nanostructured electrocatalytic materials (*e.g.*, multimetallic core-shell particles) and porous high surface area catalyst support architectures (*e.g.*, ordered 3D carbon nanotube frameworks) are presently being developed to improve fuel cell performance and reduce costs. This microfluidic platform enables the rapid characterization and optimization of these materials under a range of experimental conditions. In particular, in concert with MicroCT analysis, novel architectures and interfaces may be characterized to determine the relationship between important physical and chemical properties (*e.g.*, catalyst distribution and uniformity, internal structure and porosity, electrode / membrane interface visualization) and electrochemical performance.
- Presently, research efforts focused on the development of novel catalyst layers and ionomeric materials remain disconnected often resulting in morphological and electrochemical mismatches in fabricated MEAs (*e.g.*, hydrophobicity, ion exchange capacities) which severely hamper fuel cell performance. Electrode-electrolyte and electrode-membrane interfacial structures are fundamentally different and significant work must be done to understand these parameters. Such studies maybe performed in this microfluidic platform by introducing the thin membrane layer over an electrode which still allows for electrolyte flow enabling individual electrode investigations and interfacial analyses. As mentioned above, physical and electrochemical properties may be analyzed via combined microfluidic fuel cell and microtomographic studies. Probing and optimizing these interfaces will facilitate the development of novel high performance "non-Nafion" based MEAs for fuel cell applications.

- The impact and nature of contaminants in a fuel cell system must be analyzed to improve durability and meet DOE performance benchmarks. Impurities from real-world environments, *i.e.* SO_X compounds from military applications and NaCl from marine applications, hinder performance by poisoning cathode catalysts. Dopants used to prevent membrane degradation, *i.e.* Ce, Mn ions for perfluorinated sulfonic acid membranes, affect oxygen reduction reaction rates by hindering proton transport in PEM-based fuel cells. Internally generated species, *i.e.* crossed over fuels and undesired by-products, have significant effects of cathode and overall fuel cell performance due to surface poisoning and radical formation. The effects of all these contaminants may be explored in this microfluidic platform by introducing species via the flowing electrolyte stream. These studies would enable the rapid determination of critical contaminant concentrations and exposure times as well as identify optimal catalyst materials and operating protocols.
- Degradation mechanisms of catalyst layers are dependent on thermodynamic parameters (pH, concentration, temperature) and operating strategies ("drive"cycles). Varying these parameters can dramatically alter degradation rates and surface instabilities. Consequently, data available in literature vary substantially depending on the experimental conditions. A systematic investigation of the effects of these parameters is possible in this microfluidic platform as multiple experimental conditions may be employed. Furthermore, soluble degradation by-products may be measured from the flowing electrolyte stream via techniques used in electrochemical cell studies. A detailed analysis of dissolution rates under various conditions would guide the design of robust fuel cell systems.
- Expanding analyses to direct liquid fuel cells (DLFCs) is interesting as organic fuel oxidation reactions are more challenging than hydrogen oxidation. Also, optimization of anode

performance would enable more efficient DLFCs which may be used for portable electronic applications. To this end, the development of a liquid-based microfluidic pseudo half-cell configuration would be very beneficial. Such a platform would consist of anodic and electrolyte streams of flexible composition and a hydrogen cathode as a reference and counter electrode. This liquid-phase platform would enable detailed analyses of organic fuel oxidation mechanisms on the anode (including by-product formation) and electrode / electrolyte (membrane) interface structure and properties.

7.3 References

1. Whitesides, G.M. and G.W. Crabtree, *Perspective: Don't Forget Long-Term Fundamental Research in Energy.* Science 2007. **315**: p. 796-798.
2. Dyer, C.K., *Fuel cells for portable applications.* Journal of Power Sources, 2002. **106**(1-2): p. 31-34.
3. Jacoby, M., *Analytics for Fuel Cells.* Chemical & Engineering News, 2009. **87**(13): p. 39-41.
4. Carrette, L., K.A. Friedrich, and U. Stimming, *Fuel cells: Principles, types, fuels, and applications.* Chemphyschem, 2000. **1**(4): p. 162-193.
5. Borup, R., J. Meyers, B. Pivovar, Y.S. Kim, R. Mukundan, N. Garland, D. Myers, M. Wilson, F. Garzon, D. Wood, P. Zelenay, K. More, K. Stroh, T. Zawodzinski, J. Boncella, J.E. McGrath, M. Inaba, K. Miyatake, M. Hori, K. Ota, Z. Ogumi, S. Miyata, A. Nishikata, Z. Siroma, Y. Uchimoto, K. Yasuda, K.I. Kimijima, and N. Iwashita, *Scientific aspects of polymer electrolyte fuel cell durability and degradation.* Chemical Reviews, 2007. **107**(10): p. 3904-3951.
6. Gottesfeld, S., *Polymer Electrolyte and Direct Methanol Fuel Cells*, in *Electrochemical Engineering*, D.D. Macdonald and P. Schmuki, Editors. 2007, Viley-VCH Verlag GmbH & Co. KGaA: Weinheim. p. 544 - 661.
7. Perry, M.L. and T.F. Fuller, *A historical perspective of fuel cell technology in the 20th century.* Journal of the Electrochemical Society, 2002. **149**(7): p. S59-S67.
8. Kucernak, A.R. and E. Toyoda, *Studying the oxygen reduction and hydrogen oxidation reactions under realistic fuel cell conditions.* Electrochemistry Communications, 2008. **10**(11): p. 1728-1731.
9. Hizir, F.E., S.O. Ural, E.C. Kumbur, and M.M. Mench, *Characterization of interfacial morphology in polymer electrolyte fuel cells: Micro-porous layer and catalyst layer surfaces.* Journal of Power Sources, 2010. **195**(11): p. 3463-3471.
10. Kim, S., M. Khandelwal, C. Chacko, and M.M. Mench, *Investigation of the Impact of Interfacial Delamination on Polymer Electrolyte Fuel Cell Performance.* Journal of the Electrochemical Society, 2009. **156**(1): p. B99-B108.
11. Ramasamy, R.P., E.C. Kumbur, M.M. Mench, W. Liu, D. Moore, and M. Murthy, *Investigation of macro- and micro-porous layer interaction in polymer electrolyte fuel cells.* International Journal of Hydrogen Energy, 2008. **33**(13): p. 3351-3367.
12. Brushett, F.R., H.T. Duong, J.W.D. Ng, A. Wieckowski, and P.J.A. Kenis, *Investigation of Pt, Pt_3Co and Pt_3Co/Mo cathodes for the Oxygen Reduction Reaction in an Acidic Microfluidic H_2/O_2 Fuel Cell.* Journal of the Electrochemical Society, 2010. **157**(6): p. B837-B845.

13. Brushett, F.R., A.S. Hollinger, L.J. Markoski, and P.J.A. Kenis. *Microfluidic Fuel Cells as Microscale Power Sources and Analytical Platforms*. in *Proceedings of ASME 2009 2nd Micro/Nanoscale Heat & Mass Transfer International Conference*. 2009. Shanghai: in press *(invited paper)*.

14. Brushett, F.R., R.S. Jayashree, W.P. Zhou, and P.J.A. Kenis, *Investigation of Fuel and Media Flexible Laminar Flow-Based Fuel Cells.* Electrochemica Acta, 2009. **54**.

15. Brushett, F.R., P.J.A. Kenis, and A. Wieckowski, *New Concepts in the Chemistry & Engineering of Low Temperature Fuel Cells*, in *Fuel Cell Science: Theory, Fundamentals, and Bio-Catalysis*, A. Wieckowski and J.K. Norskov, Editors. 2010, John Wiley & Sons, Inc.: Hoboken. p. 565-610.

16. Brushett, F.R., M.S. Naughton, J.W.D. Ng, L.L. Yin, and P.J.A. Kenis, *Analysis of Electrode Performance in an Alkaline Microfluidic H_2/O_2 Fuel Cell.* in preparation.

17. Brushett, F.R., M.S. Thorum, N.S. Lioutas, M.S. Naughton, C. Tornow, H.R. Jhong, A.A. Gewirth, and P.J.A. Kenis, *A Carbon-Supported Copper Complex of 3,5-Diamino-1,2,4-triazole as a Cathode Catalyst for Alkaline Fuel Cell Applications.* Journal of the American Chemical Society, 2010. **132**(35): p. 12185-12187.

18. Brushett, F.R., W.P. Zhou, R.S. Jayashree, and P.J.A. Kenis, *Alkaline Microfluidic Hydrogen-Oxygen Fuel Cell as a Cathode Characterization Platform.* Journal of the Electrochemical Society, 2009. **156**(5): p. B565-B571.

19. Jayashree, R.S., D. Egas, J.S. Spendelow, D. Natarajan, L.J. Markoski, and P.J.A. Kenis, *Air-breathing laminar flow-based direct methanol fuel cell with alkaline electrolyte.* Electrochemical and Solid State Letters, 2006. **9**(5): p. A252-A256.

20. Naughton, M.S., F.R. Brushett, and P.J.A. Kenis, *Carbonate resilience of flowing electrolyte-based alkaline fuel cells.* Journal of Power Sources, 2010: p. accepted.

21. Whipple, D.T., E.C. Finke, and P.J.A. Kenis, *Microfluidic Reactor for the Electrochemical Reduction of Carbon Dioxide: The Effect of pH.* Electrochemical and Solid State Letters, 2010. **13**(9): p. D109-D111.